Fermi National Accelerator Laboratory

Fermilab Accelerator Upgrade
Phase I

April 1989

Operated by Universities Research Association, Inc., under contract with the United States Department of Energy

FERMILAB ACCELERATOR UPGRADE
PHASE 1

1. OVERVIEW

The long range Fermilab program requires maintaining a viable physics program into the late 1990's when the SSC will begin operation. The program calls for doubling the integrated luminosity with each succeeding run until peak luminosities of $>5 \times 10^{31}$ cm^{-2} s^{-1}, or an integrated luminosity per run in excess of 100 pb^{-1} is achieved, effectively doubling the mass range accessable for discovery. In order to achieve this goal we present a highly challenging upgrade of the present Tevatron proton accelerator and proton-antiproton collider.

In the near term, improvements already in progress will achieve the design goal of the present Tevatron project for fixed target physics: 2×10^{13} ppp (protons per pulse) and exceed those of collider operation: $10^{30} cm^{-2} s^{-1}$ peak luminosity. In addition, a second interaction region will exist at D0. However, more and more extensive modifications need to be planned in order to sustain the increasing luminosity per run. Such a plan, by necessity, has modifications in almost all areas of the accelerator as the present system is already reasonably optimized.

The Upgrade places emphasis on collider operation. This is because collider physics demands a continual increase in integrated luminosity with each run to productively search new physics domains. Fixed target physics intensity improvements are also planned and are part of the overall consideration. The proton intensity increases will aid in antiproton production as well as substantially benefit the fixed target program.

The full upgrade proposal has 3 phases involving replacing the Main Ring with a dedicated injector, and a new superconducting ring of higher energy than the Tevatron. This report presents a detailed technical evaluation of the initial steps in this proposed upgrade, the so-called Phase 1, which results in a luminosity of $\sim 10^{31}$ cm^{-2} s^{-1}.

A major component of this project is the increase in the Linac energy from 200 Mev to 400 Mev. This project is already extensively described in the its own design report and is only presented in outline in this document.

1.1 INTRODUCTION

In order to increase the luminosity beyond the existing design goals then the antiproton production rate must be increased significantly, this requires (among other things) an increased number of protons per batch delivered onto the antiproton production target, and hence would also result in higher fixed target beam intensities. The antiprotons manufactured must be collected and stored. More antiprotons (and protons) must be colliding in

the Tevatron with smaller beam emittances and dispersed into a greater number of bunches than the present six bunch operation.

The first section defines the beam parameters necessary to reach such luminosities and identifies the design modifications needed to realise these goals. The following chapters provide a more detailed technical review of each of the major elements called for in Phase 1 of the upgrade scheme.

1.2 CHOICE OF PARAMETERS

The luminosity for head-on collisions is given by:

$$L = N_p N_{\bar{p}} B f_o / 4\pi\sigma^2 = \frac{3}{2} \frac{BN_{\bar{p}} N_p f_o \gamma}{\beta^* \epsilon_N}$$

where N_p and $N_{\bar{p}}$ are the proton and antiproton per bunch intensities, B is the number of bunches in each beam, f_0 is the revolution frequency (47 kHz), σ is the rms beam size at the interaction point, ϵ_N is the normalised beam emittance and β^* is the lattice function at the interaction point. Thus the relationship between the luminosity and the primary beam parameters is given by :

$$L \alpha \frac{BN_{\bar{p}} N_p}{\beta^* \epsilon_N}$$

In chosing a suitable parameter set to achieve high luminosities there are certain constraints imposed by the antiproton source and operational factors. The available stacking rate requires that :

$$BN_{\bar{p}} < \tau_{eff} R_{\bar{p}} SL$$

where τ_{eff} is the transfer efficiency from the stack to the collision point, $R_{\bar{p}}$ is the antiproton stacking rate, and SL is the average length of the store. A transfer efficiency of 70%, and an average store length of 20 hrs has been assumed throughout this report. This relationship emphasizes the importance of reliability considerations during the stores.

The relationship between antiproton supply and demand is given by the rate at which antiprotons are removed from the machine by the process of interactions at the crossing points. Hence :

$$\sigma_{tot} L_0 \#_{IR} < \tau_{eff} R_{\bar{p}}$$

for a total cross-section of 80 mb, an initial luminosity of 10^{31} cm^{-2} sec^{-1} and two interaction regions then the stacking rate must be at least 6×10^9 antiprotons per hour, a relatively modest requirement.

The maximum achievable stack size also provides an upper bound on the peak luminosity by:

$$B\dot{N}_{\bar{p}} < \tau_{eff} S_{max} U$$

where S_{max} is the maximum stack size and U is the fraction of the beam that can be unstacked from the core. For 6 bunch operation U is taken to be 66%, and increases to 75% as the number of bunches is increased..

There are two ways to raise the luminosity: increasing the bunch density (more particles per bunch, or smaller beam sizes at the collision points), or more bunches. While we do expect to increase the bunch density from the Tevatron 1 design value, the major increase in luminosity is achieved by colliding many more bunches. This is dictated by both experimental and accelerator physics considerations.

Multiple interactions per bunch collision can provide problems of event reconstruction in the detectors. The average number of interactions $\langle n \rangle$ is given by :

$$\langle n \rangle = \frac{\sigma_{inel} L_0}{B f_0}$$

Since σ_{inel} and f_0 are fixed then for a given luminosity the average number of interactions per crossing is inversely proportional to the number of bunches. At L and assuming 50 mb for the detectable inelastic cross section, there will be 0.35 interactions per bunch crossing for 3×3 bunches, and half that number for 6×6. Multiple interactions will occur respectively in 19% and 10% of the events. If the detectors are capable of analysing only those events in which there was one interaction per crossing, then the effective luminosity is reduced in the two cases to 81% and 90% of L. The situation becomes worse at higher luminosities. At 10^{31} and 6×6, the average number of interactions per crossing is 1.8, and if the multiple events are rejected then the effective luminosity is saturated at about one third of the figure of 10^{31}. However with n=44 bunches (of protons and antiprotons), and L=50 L. there will only be 1.19 average interactions per crossing and single interactions will occur 54% of the time there is an interaction.

Accelerator considerations also argue in favor of more bunches. Very dense bunches of the kind needed to produce 10^{31} luminosities with only 6

bunches are not only technically difficult to achieve, but also dilute very rapidly due to the phenomona of intrabeam scattering. This effect, multiple coulomb scattering amongst the individual particles of the bunch, severely limits the luminosity lifetime (and hence the integrated luminosity) resulting from intense bunch collisions. This is illustrated in fig 1.2.1a which shows the integrated luminosity obtained from a 20 hour 6 bunch store versus the initial luminosity multiplied by the length of the store. In the absense of any mechanism which dilutes the bunches then there is a one-to-one correspondance between the two axis as represented by the solid line. The deviation of any data point from this line represents loss of luminosity due to the increase in beam emittance from intrabeam scattering. The dashed and dotted lines connect equal intensity bunches with different initial transverse emittances (24π, 12π, 6π). The two curves correspond to initial bunch intensities of 6×10^{10}, and 10×10^{10}. The most intense bunch (6π, 10×10^{10}) achieves only 28% of the infinte lifetime integrated luminosity which corresponds to an average luminosity lifetime of ~7 hours over the 20 hour store duration. The actual luminosity lifetime of course starts at a much smaller figure than this and evolves during the 20 hours to a larger figure. At bunch intensities in this regime reducing the beam emittance below 12π results in only small increases in integrated luminosity. This can be seen in fig 1.2.1b which shows the bunch parameters for this high intensity bunch during the 20 hours. After 4-5 hours the initial transverse emittance has doubled and the luminosity has fallen by a factor of 3, at this point the rate of beam growth has declined significantly and the luminosity lifetime is ~ 15 hours. For a fixed number of antiprotons available from the source and a constant beam emittance more less dense bunches will produce a greater integrated luminosity the a few intense ones. The bunch parameters used for this design (12π, 6×10^{10}) correspond to an initial luminosity lifetime of ~20 hours.

At present there seems to be no feasible technical way to avoid the intrabeam scattering problem. Bunched-beam cooling for the bunch lengths needed in this proposal appears to be beyond reasonable technical expectations.

One of the fundamental luminosity limits is the beam-beam tune shift, $\Delta\nu$, (roughly equal to the beam-beam tune spread). This effect is caused by the bunches passing through each other at the collisions points and is proportional to the bunch density and the number of collisions per revolution. The relationship between the tune shift per collision point and the fundamental parameters is given by :

$$\Delta\nu = 0.007 \times \frac{N_p \ (10^{10})}{\epsilon_N \ (\text{mm-mrad})}$$

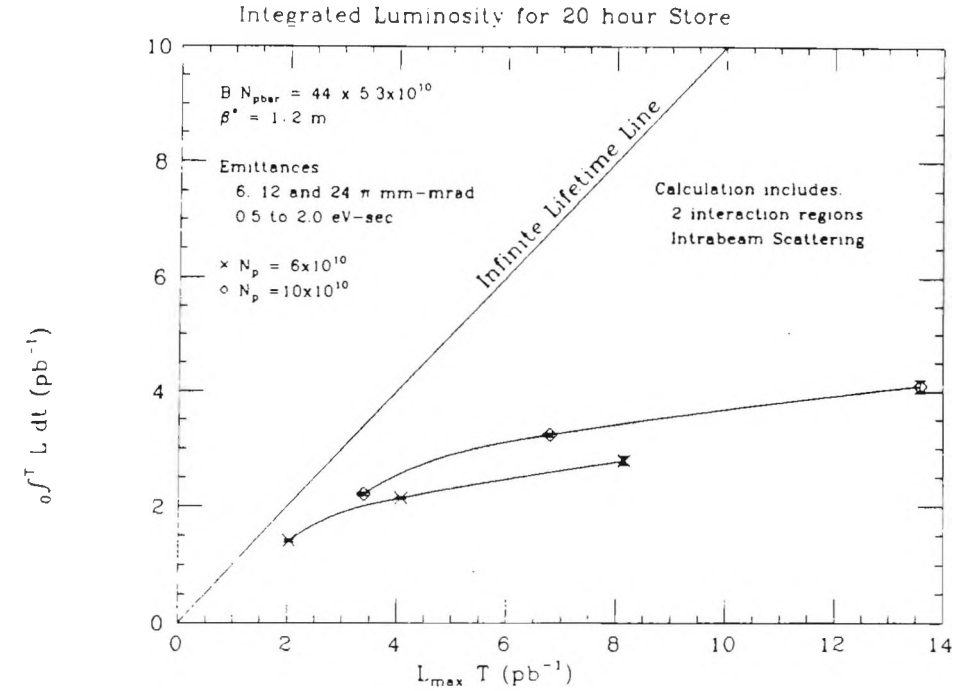

Figure 1.2.1a

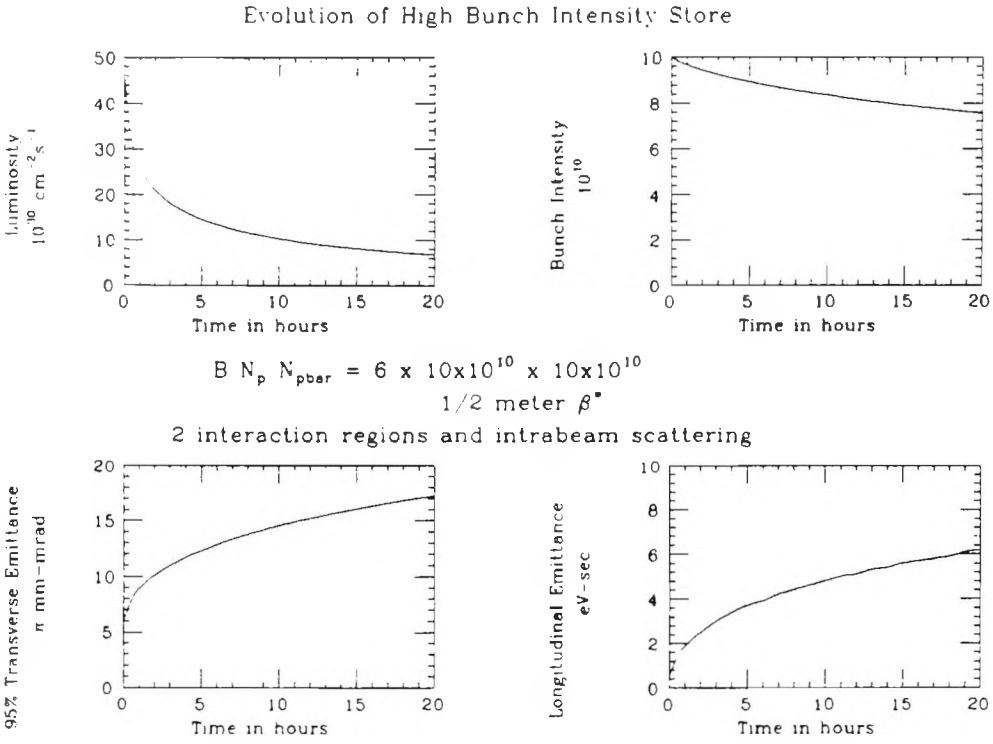

Figure 1.2.1b

The largest value of this tune shift parameter obtained to date both at Fermilab and CERN without degrading the beam lifetime is a total $\Delta\nu$ of 0.02. For head on collisions at Fermilab, this will occur at a luminosity of 2 L with 6x6 bunches. It is necessary to have the beams collide in the experimental areas, however, if the total available charge is divided among many bunches (to keep the $\Delta\nu$ per crossing small), and at the same time the number of crossing points is limited to the experimental regions by keeping the two beams apart transversely with electrostatic separators, then the luminosity can be raised without exceeding the allowable $\Delta\nu$ limit. A scheme to do this is given in Section IV.

A set of beam parameters which would produce the desired luminosity while maintaining adequately low bunch intensities to avoid the forementioned problems are given in Table 1.2.1. Beams containing 22 (44) bunches of 10-15 x 10^{10} protons and 2.8 (1.4) x 10^{10} antiprotons with transverse emittances of 15-20π mm-mrad are required. The total number of antiprotons needed in the collider is 6.2 x 10^{11}. The total number of bunches (and hence time between crossings) is defined by the need to avoid very high bunch intensities which dilute rapidly due to intrabeam scattering and providing adqueate bunch separation at the crossing points adjacent to the interaction regions. Taking both these effects into account, two scenarios are possible 22 and 44 bunches. We chose to present the 22 bunch case in this report but there are no major problems associated with implementing the 44 bunch one. Peak and intergrated luminosities are estimated to be similar in both cases.

Table 1.2.1 Parameter list - Phase 1

Protons per bunch	10-15 x 10^{10}
Antiprotons per bunch	2.8(1.4) x 10^{10}
Number of bunches	22 (44)
Lum. limit (10^{30} $cm^{-2}s^{-1}$)	11-17 peak
Bunch Spacing	792 (396)ns
Total protons (10^{12})	3.3 (6.6)
Total antiprotons (10^{12})	0.62
Pbar accumulation rate	7.6 x 10^{10}/hour
Accumulator Intensity	137 x 10^{11}
Tevatron Fill Interval	20 hours
Beam-beam tune shift	0.005 per interaction point
Transverse ϵ (95%)	15-20π x 10^{-6} m-rad w/growth to 25π
Longtitudinal ϵ(95%)	3eV-s
σ_*long (rms)	20 cm w/growth to 30 cm
β	1/2 m w/possibly 1/4 m
Harmonic Number	1113/21 21st subharmonic of 53 MHz

1.3 UPGRADE COMPONENTS

Antiproton economics represent one of the outstanding problems to be solved in this proposed upgrade. There are 3 parameters to be addressed: stack size limit, pbar yield per proton on target, protons per second on target. Increasing the stack size limit involves the utilization of higher frequency cooling systems together with curing a problem of crosstalk between the stacktail and the core cooling system with large stacks. Factors which influence the antiproton yield are the proton spot size and the collection aperture. Stronger focussing at the production target will result in a smaller spot size but will also require a sweeping system to avoid destroying the target itself. The collection aperture can be increased with improvements to certain elements in the beamline and increasing the aperture of the cooling system in the Debuncher. Delivering more protons onto the production target involves improving the Main Ring intensity and/or the repetition rate. Increasing the Linac energy will result in more protons. The effective repetition rate can be improved by a scheme to accelerate 3 booster batches. Once at flattop the batches are sequentially extracted to the target at a rate determined by the antiproton source cooling systems. Bunch shortening RF manipulations just prior to extraction may render this approach unfeasible due to longtitudinal emittance dilution in the bunches remaining in the Main Ring. Details of the required antiproton source modifications are given in section III.

Increasing the intensity of the proton bunches in the Main Ring relies primarily in phase 1 on increasing the proton density delivered to it from the Booster. We believe that the present performance of the Booster is limited by the incoherent space charge tune spread at the injection energy of 200 MeV. Evidence for this fact is shown in fig. 1.3.1 where it can be seen that the transverse emittance of the beam emerging from the Booster grows linearly with intensity. Analysis of this data shows that it is consistent with the Booster being able to sustain a tune spread, $\Delta\nu$, of 0.37 at injection. This tune spread scales as $1/\beta\gamma^2$, so injecting at 400 MeV would be expected to increase the achievable bunch density N/ϵ by 75% as indicated in fig. 1.3.1, or conversly the batch intensity for a fixed emittance beam would increase by 75%. The Booster intensity at which its aperture would begin to be a limiting factor (the fixed target limit) is also increased. Thus as long as collective instabilities can be controlled, the most cost effective way to enhance the Booster performance to the level needed in this proposal, is to increase the injection energy from the Linac from 200 MeV to 400 MeV. The method chosen to do this calls for replacing the downstream half of the present 200 MHz drift tube Linac with an 800 MHz side coupled cavity or disk and washer structure operating at 7 MeV/m. The resulting new Linac structure would be the same length as the existing device, some elements of the transport line to the Booster will require replacement. A

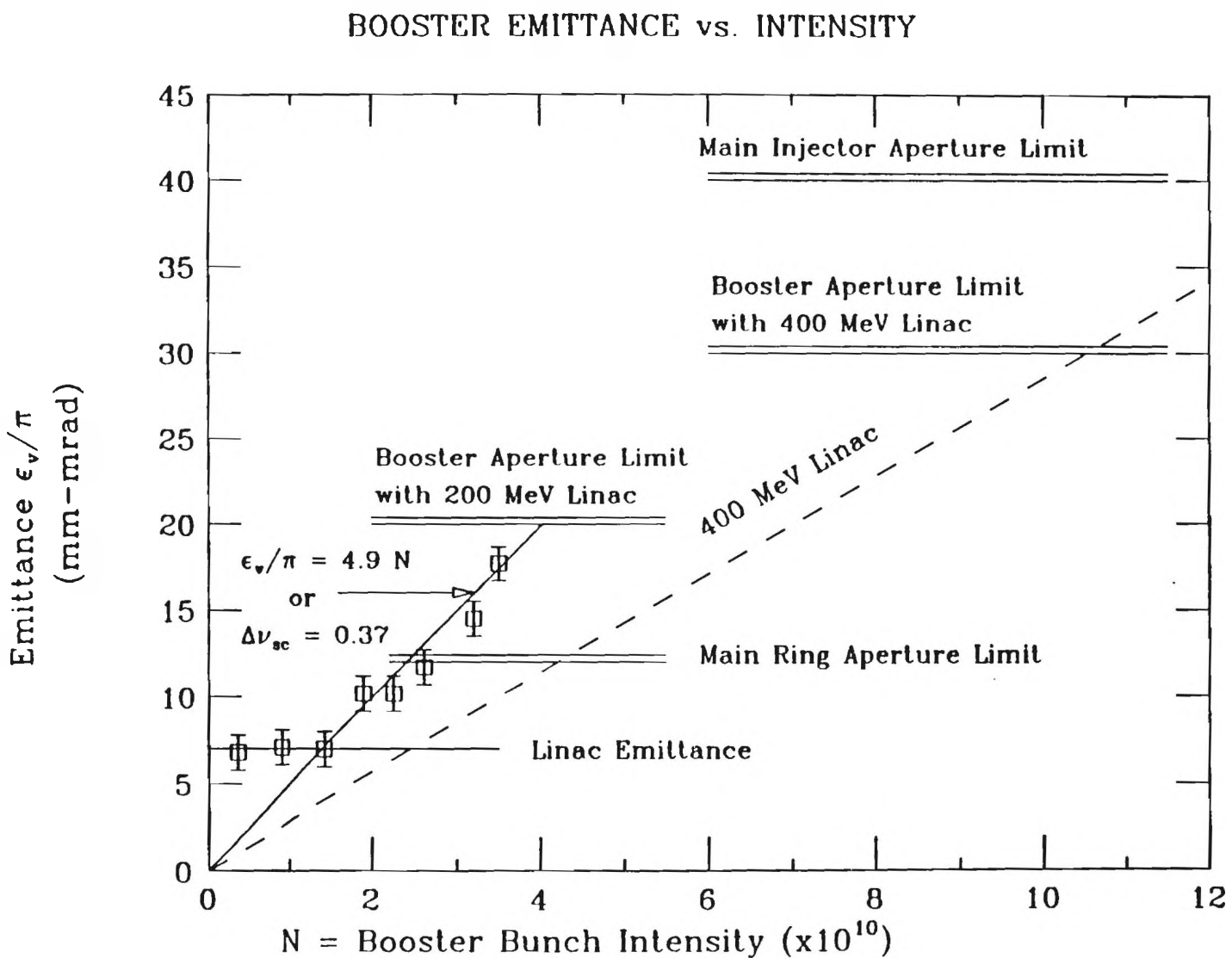
BOOSTER EMITTANCE vs. INTENSITY
Emittance ϵ_v/π (mm-mrad)
N = Booster Bunch Intensity ($x10^{10}$)
Main Injector Aperture Limit
Booster Aperture Limit with 400 MeV Linac
400 MeV Linac
Booster Aperture Limit with 200 MeV Linac
ϵ_v/π = 4.9 N
or
$\Delta\nu_{sc}$ = 0.37
Main Ring Aperture Limit
Linac Emittance
0
5
10
15
20
25
30
35
40
45
0
2
4
6
8
10
12

Figure 1.3.1

full description of the Linac energy increase is available as a design report, section II gives an outline of the project.

It is crucial to this luminosity upgrade that the Tevatron can be made to operate with significantly more bunches than the six used at present. This will require modifications to the injection and abort systems as described in section V, but more fundamentally it means that the Tevatron be made to operate with separated beams. Electrostatic separators must be installed on each side of the collision regions to produce helical spiral orbits of protons and antiprotons about one another in the transverse plane. The beams will only collide with each other at the interaction regions and not in the arcs. There are two parts to the problem. First, there is the single beam question of whether the beams with large orbit distortions can be stored with a reasonable lifetime. This is a question of magnetic field quality and available aperture in the magnets and it is especially important at injection energy where the inherent beam size is large compared to the available aperture. The other source for concern is the effect of the long range beam-beam interaction. Experience at CERN with separated beams indicates that a beam separation of 5σ is sufficient to ensure a good beam lifetime. Details on the separation scheme are given in section IV.

The other major modification to the Tevatron is the second low-beta interaction region in the D0 straight section. The existing interaction region at B0 is only partially matched to the machine lattice and introduces dispertion errors into the lattice which grow progressively worse as the beta value at the interaction point is lowered. Two such low beta regions would result in unacceptably large values of the dispersion function around the ring. Consequently we will install new matched low beta insertions at both the D0 and B0 collision points, which incorporate space for the electrostatic deflector plates. The design details of these insertions are given in section VII.

1.4 IMPLEMENTATION SCHEME

The proposed upgrade will be implemented in an incremental fashion with the improvements becoming increasingly more costly and technically difficult. Table 1.4.1 lists the upgrade components of phase 1 grouped together in two steps. The steps have been phased so that completing one step between each Tevatron collider run would result in a peak luminosity profile as a function of time as shown in table 1.4.1.

In estimating the peak luminosity (Lmax) the following assumptions were made: The number of antiprotons available for a transfer from the Source was given by a 20 hour stacking scenario, this is equivalent to assuming a ~20 hour luminosity lifetime in the Tevatron and one transfer per day. The maximum number of antiprotons which can be unstacked from the core is 66% of the stack size when taking 6 bunches of 1.0 eV-s. For 20 or more bunches then this

number rises to 75% or more depending on how the individual bunch intensity is varied. The efficiency of transferring the antiprotons from the Source to the collision point at low beta in the Tevatron is assumed to be 70%. The maximum stack size needed in the Source is 13.7×10^{11}, the largest stack of antiprotons achieved to date is 8.1×10^{11}. The number of colliding bunches must be increased from 6 to 22 to make full use of the number of antiprotons available.

TABLE 1.4.1 Step by Step Improvement Factors

Upgrade Component	Stacking Rate $x10^{10}$	Stack Size $x10^{10}$	Lum Limit $x10^{30}$	Beam Parameters	Limitations
None	2.0	55	1.6	Nprot $6.0x10^{10}$ Npbar $2.9x10^{10}$ Bunches 6 Emittance 18-25π Bstar 0.55m	Stacking rate $\Delta\nu$ beam-beam
Source Acceptance 20π -> 30π $\Delta p/p$ 3% -> 4% 0.5 Hz production cycle 8 GHz cooling systems New Low Beta Design Tevatron separated orbits	3.2	82	6.6-9.4	Npbar $7.2x10^{10}$ Emittance 14-16π Nprot $7.0\text{-}10.0x10^{10}$ Bunches 6 Bstar 0.5	Stacking rate
Smaller Spot on target Linac Energy Upgrade 22 bunch operation	7.3	137	11.0-17.0	Npbar $2.8x10^{10}$ Bunches 22 Nprot $10\text{-}15x10^{10}$ Emittance 15-19π	Proton Int/rate

It is more difficult to estimate accurately the integrated luminosity obtained from a given peak luminosity. Present collider operations have achieved a peak luminosity of 2×10^{30} cm^{-2} s^{-1} and an average store attains 80% of this value. The number of collision hours per week is ~120. Transfers are taken approximately every 20 hrs, and with an initial luminosity lifetime of ~15hrs this results in 300-500 nb^{-1} of integrated luminosity per week. It is expected that the integrated luminosity per week should scale directly from the peak luminosity.

1.5 LIMITATIONS OF THE PRESENT PLAN

The fundamental limitation on luminosity in an antiproton collider is the ability to make and store antiprotons. This is shown in table 1.4.1. There are however features in this proposal which have certain risk factors associated with them, and which do not show up explicitly in this table. Conversely some features of the scheme are relatively straight forward and hence can be approached with a certain degree of confidence. Increasing the available aperture in the Source falls under this second catagory as does the Linac energy upgrade.

The requirement of operating the Tevatron with separated beams could well prove to be difficult especially at the injection energy where the required separation leads to very large amplitude orbits. The magnetic field quality deteriorates at large amplitudes leading to non-linear behaviour of the beam properties (tune, chromaticity) which must be controlled very precisely during filling and acceleration in order to preserve the beam intensity and emittance. The situation is further complicated by the time and energy dependant persistent current phenomona observed for the first time in the Tevatron during the initial collider run. Operational techniques to adequately correct the effects of rapidly changing chromaticity are still in the developmental stage.

The increase in antiproton production rate (and fixed target intensity) resulting from the Linac energy increase is contingent on the Booster, Main Ring and Tevatron being able to handle these more intense beams (batch intensities > 3×10^{12}) without any problems arising from beam instabilities. Precise calculations of instability thresholds are difficult to make, so there is an element of uncertainty as to the achievable bunch densities in the various accelerators. Active feedback systems and Landau damping techniques may prove necessary

II. LINAC DESIGN

An important parameter throughout the accelerator chain is ϵ, the transverse invariant beam emittance, a measure of beam brightness. The initial value of ϵ is established in the Linac and its pre-injector. At each step in the acceleration process, ϵ can only become larger through dilution processes. The first place where this occurs is in transferring the protons into the Booster. The most straightforward way in which to preserve the small emittance of the Linac is to raise the energy at which the Linac beam is injected into the Booster.

The Linac currently provides 0.7 x 10^{10} H^-/bunch/turn into the Booster with ϵ = 7 to 8 π mm-mrad. Theoretical calculations and experimental measurements have established that the tune-spread caused by space-charge, $\Delta\nu$, degrades transverse emittance of the proton beam at injection into the Booster at intensities corresponding to two turns or greater injected from the Linac. It is believed that the degradation of the transverse beam emittance is determined by a space-charge tune-shift limit of $\Delta\nu$=0.37 in the Booster at the start of acceleration after the beam has been bunched. As the space-charge tune-shift is inversely proportional to a relativistic factor $\beta\gamma^2$, and proportional to N/ϵ, it should be possible to reduce the emittance in the space charge dominated intensity regime by increasing the injection energy from 200 MeV to 400 MeV, a change in $\beta\gamma^2$ of 1.75. Normalized emittances of 10π for bunch intensities of 3.5×10^{10} particles out of the Booster could be expected instead of the presently measured 18π numbers. Conversely, transmitted intensities in the Booster and Main Ring, which are limited by the transverse emittance growth, could be expected to increase by approximately the same 1.75 factor for emittances which are presently encountered.

A Linac upgrade project to increase the energy from 200 MeV to 400 MeV has been submitted. The downstream end of the Linac will be replaced with more efficient, higher accelerating gradient cavities and a matching section between the existing Linac cavities and the higher accelerating gradient cavities. The downstream drift-tube tanks will be replaced with side-coupled cavities operating at a frequency of 800 MHz, four times the operating frequency of the present Linac. The higher frequency coupled cavities will be operated at an accelerating gradient of 7.5 MV/m (effective gradient for particle acceleration ~6 MV/m) or more compared to the 2.5 MV/m in the present drift-tube system. They will be installed in the space made available by removing the drift-tube tanks. They will be driven by 12 MW, 800 MHz klystron power supplies, thus replacing about half of the old 200 MHz output power amplifier tubes.

The plan also includes upgrading the Linac to Booster transport line to accommodate the higher energy, adding an rf debunching cavity in the line, new elements on the Booster injection girder, and new beam position, size, and

bunch length monitors. These changes to accommodate the higher energy can be done without scheduled interruption in the present operating schedule. The only conventional construction required will be a minor modification in the Linac gallery to provide the additional space for the 800 MHz rf systems.

III. ANTIPROTON SOURCE DESIGN

1. Introduction

During the construction of the Antiproton Source, the major areas for R&D work were in the areas of targeting and stochastic cooling. This will continue to be the case as the Source performance is improved and upgrades focused on improved stacking rate and improved pbar beam quality are implemented.

The improvement program for the Antiproton Source in phase 1 of the collider upgrade has the following components:

1. An increase in the effective repetition rate of the Main Ring for antiproton production using the "multi-batch" technique. This should provide a factor of 1.36 in the number of targeting cycles per hour for production, which will give the same factor increase in stacking rate, provided that the Source can cope with the increased cycle rate without a loss of efficiency. Major changes in the Source cooling systems will be required to prevent this loss of efficiency.

2. An increase in the transverse acceptance of the Debuncher ring from about 20 pi mm-mrad to about 28 pi mm-mrad. This improvement by itself has been measured to yield an increase of about 28% in pbar yield (i.e., the number of pbars collected per proton on target). With increases in the AP-2 beam line apertures an increase in the lithium lens gradient to 1000 T/m, the overall gain in pbar yield is calculated to be 50%.

3. An increase in the effective longitudinal acceptance of the Debuncher ring from 3% to 4%. This acceptance was originally limited by the voltage on the bunch rotation cavities. This voltage has been increased by a factor of 1.5 and further improvements are planned. In order to benefit from the increased voltage a Debuncher momentum cooling system must be implemented. Once the cooling system is operational, an increase of 1.3 in stacking rate is expected.

4. An increase of a factor of 1.7 in the proton beam intensity on the target; this will result from the Linac upgrade. It will be necessary at this point to move the primary proton beam across the target to avoid local melting in the target.

The overall gain in pbar stacking rate will thus be:

$1.36 \times 1.5 \times 1.3 \times 1.7 = 4.5$

The present stacking rate of 1.9 ma/hr is thus expected to rise to a value of 5.9x1.2=8.5 ma/hr at the end of phase 1.

2. Main Ring Operation for Antiproton Production

One of the major schemes for achieving increased stacking rate in phase 1 of the upgrade is the "multi-batch" mode of operation of the Main Ring for pbar production. In this mode, three batches are injected at 8 GeV in the Main Ring, accelerated to flat top simultaneously, and extracted one at a time to the pbar production target, with as short an interval between the extractions as possible. The limit on how short this interval can be is set by the Source, which must collect and cool the pbars during the interval between extractions. The goal for the minimum interval between extractions (i.e., the Source repetition period) has been set at 1.5 sec; this corresponds to an increase of a factor of about 1.36 over the present single-batch targeting cycle rate.

Operation in this mode was first attempted in tests in late 1987 and early 1988; problems were encountered both with Main Ring bunch narrowing and with the stacking efficiency of the Source. This kind of operation places great demands on the Source targeting and cooling systems. Most of the modifications to cooling systems described in the sections below are related to coping with this rapid cycle rate.

3. Debuncher Aperture

The factors contributing to the pbar yield which are under our control are the proton spot size and the collection system acceptances. The issues related to improvements in the proton spot size will be discussed in the section below, "Targeting". The collection system acceptances are defined by the transfer line from the target to the Debuncher, and the Debuncher ring aperture itself. The transverse aperture of the Debuncher is set by the physical dimensions of the pickup and kicker electrodes in the stochastic cooling system. During a study period in September, 1987, we measured[1] the Debuncher aperture and the pbar yield into the Debuncher with these cooling systems removed. The Debuncher aperture results are shown in figs 3.3.1 and 3.3.2. Fig. 3.3.3 shows a direct comparison of the difference in the measured pbar yield with and without the tanks in. The yield difference at small acceptances is due to the fact that the data were taken with two different proton spot sizes; after correcting for this difference, the conclusion is that the pbar yield increased by about 28% when the tanks were removed. We cannot of course collect pbars without the Debuncher stochastic cooling systems, but we can rebuild the systems to open the electrode gaps from 3

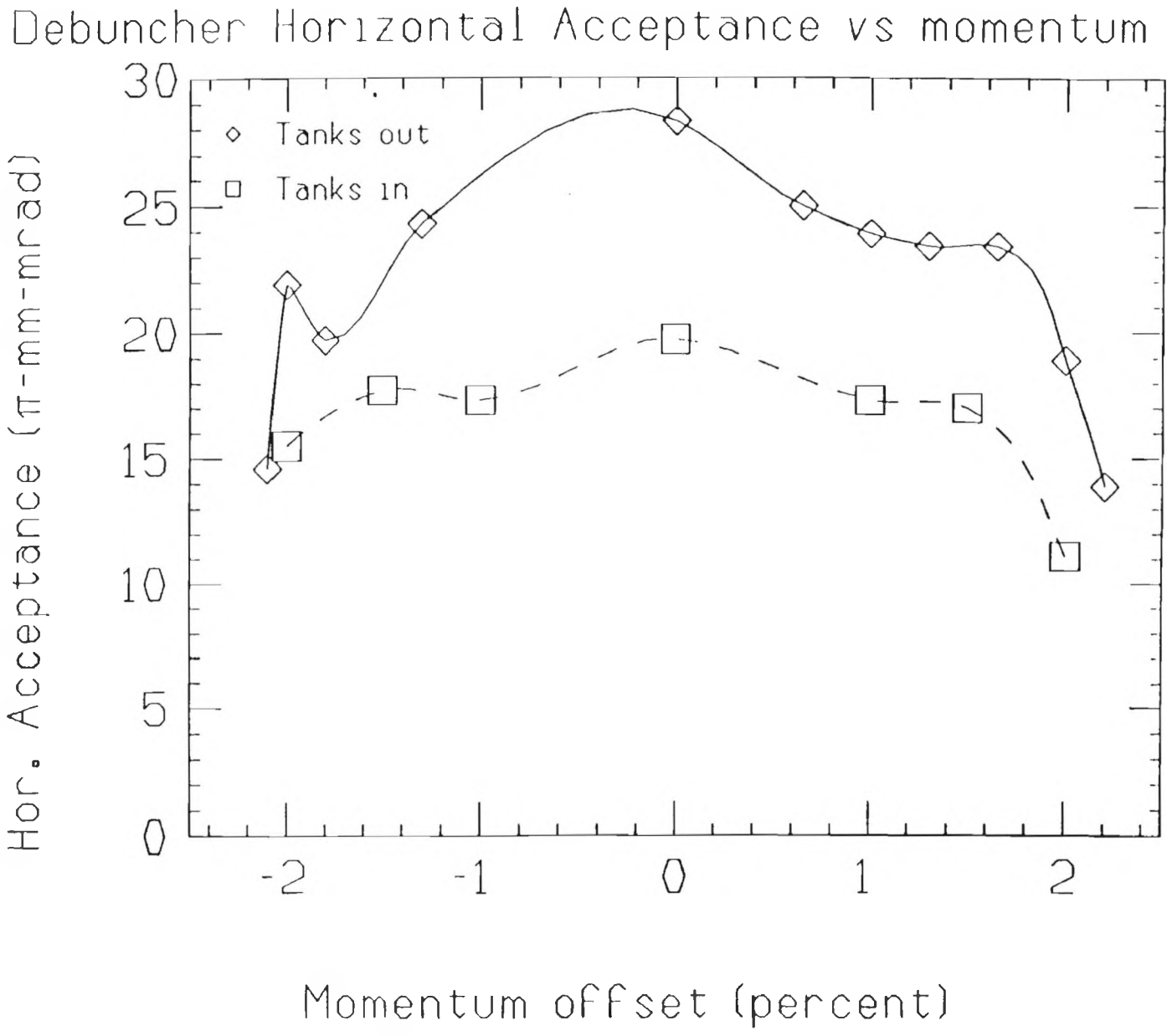
Debuncher Horizontal Acceptance vs momentum
Tanks out
Tanks in
Hor. Acceptance (π-mm-mrad)
30
25
20
15
10
5
0
-2
-1
0
1
2
Momentum offset (percent)

Figure 3.3.1

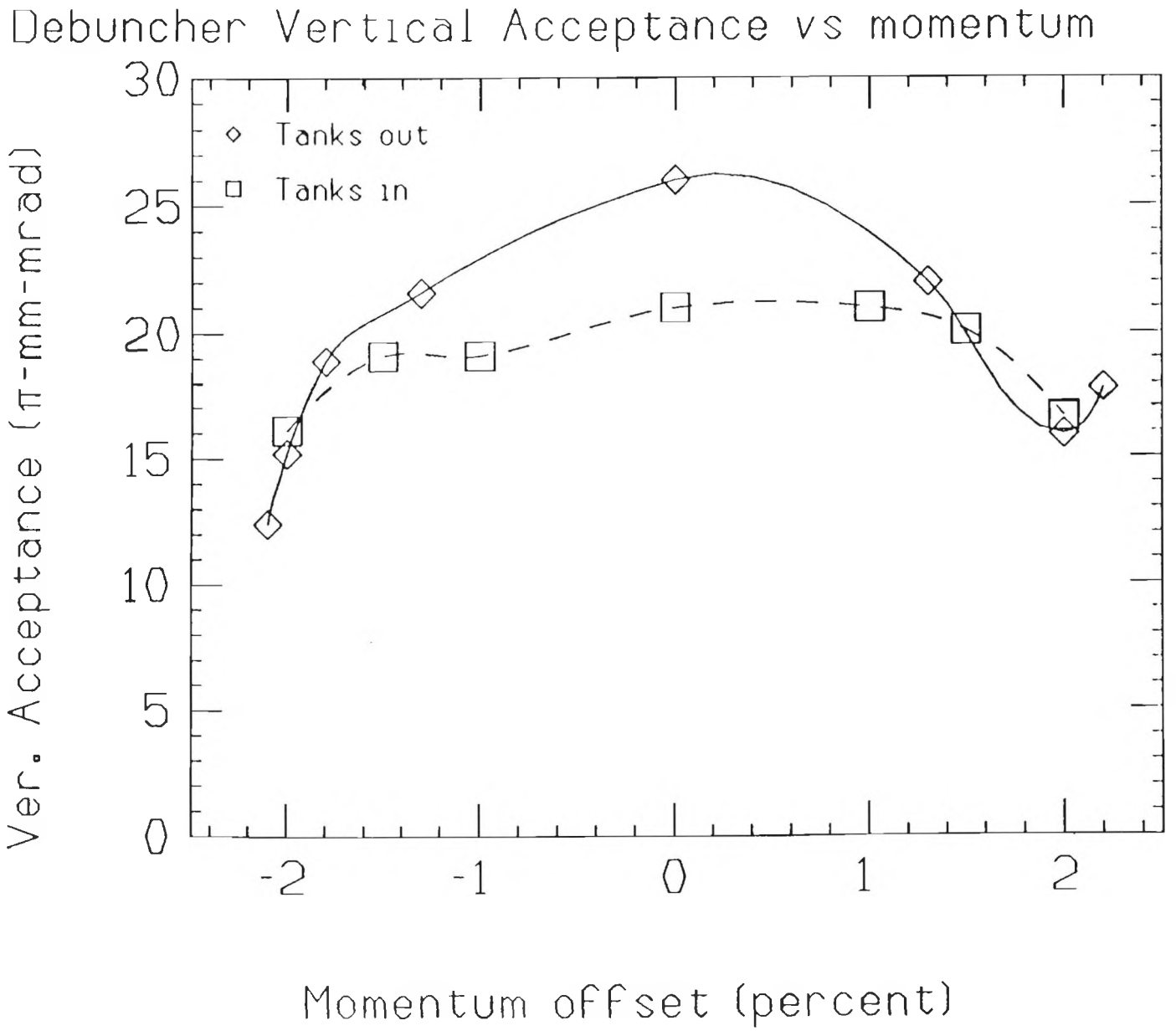
Debuncher Vertical Acceptance vs momentum
Tanks out
Tanks in
Ver. Acceptance (π-mm-mrad)
Momentum offset (percent)
30
25
20
15
10
5
0
-2
-1
0
1
2

Figure 3.3.2

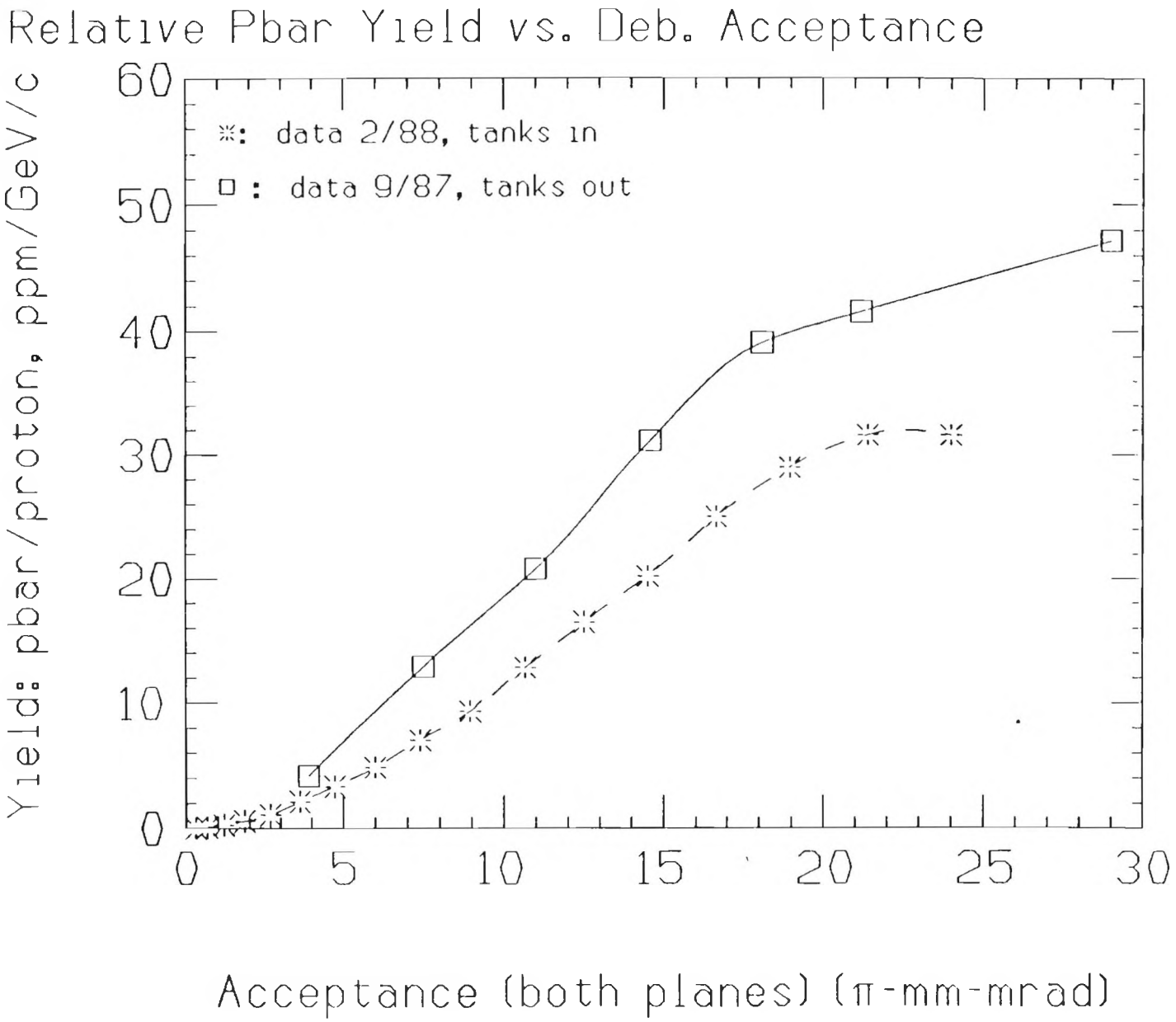
Relative Pbar Yield vs. Deb. Acceptance
Yield: pbar/proton, ppm/GeV/c
60
50
40
30
20
10
0
0
5
10
15
20
25
30
*: data 2/88, tanks in
□ : data 9/87, tanks out
Acceptance (both planes) (π-mm-mrad)

Figure 3.3.3

cm to 4 cm (maximum gap). This will correspond to a 30 pi mm-mrad aperture in the cooling tanks. Based on our September measurements, we will immediately realize a 28% gain in pbar yield.

At this point, the collection system is limited by the AP-2 beam line apertures. Calculations have indicated that further gains can be made if improvements are made to the beam line; the 28% yield increase measured as described above should increase to 40%. The details of the improvements are under study at this time; we expect to at least require the replacement of two or more dipoles in the beam line with larger-gap magnets. As will be discussed below, after the Debuncher aperture is increased, additional increases in the pbar yield (on the order of 10%) could be provided by the use of a higher gradient collection lens. The overall improvement factor in pbar yield could be as high as 50%, if the beam line improvements, Debuncher aperture increase, and higher gradient collection lens, are all implemented.

4. Debuncher RF

An additional increase in the pbar yield can be provided by utilizing the full momentum acceptance of the Debuncher. This will require an improvement to the Debuncher bunch-rotation RF system. The momentum acceptance of the AP-2 beam line and the Debuncher itself are both 4% or greater, but the momentum spread which can be effectively captured and bunch-rotated by the Debuncher RF is only 3%. The limitation can be relieved by higher voltage on the RF cavities. We believe that the cavities themselves can handle the required x2 voltage increase needed to accept a 4% momentum spread. Higher power tubes have increased the total bunch rotation voltage from under 4 MV to nearly 6 MV. Improvements in the drivers are expected to provide over 6 MV. However, we do not yet efficiently stack the additional beam which is rotated because of the wider momentum spread after rotation. We expect an increase of 30% in the pbar yield when the Debuncher momentum cooling is operational.

5. Debuncher Stochastic Cooling: transverse

In order to be able to better cope with the rapid cycle rate required for multi-batch Main Ring operation, improvements to the Debuncher transverse cooling systems were made last year. Here, we have been exploiting the fact that the system is power-limited, and can benefit from more power. Last year,we designed, built and installed two optical notch filters. These filters are tuned to notch out the thermal noise power in the system TWT's at the Debuncher revolution harmonics, while leaving the frequencies near the betatron sidebands, at which the cooling occurs, untouched. The net result is a reduction by almost a factor of two in the system power, at frequencies for

which there is no cooling. Since the total power is limited by the TWT's, the amplifier gain can now be increased to bring the total power back to the TWT limit. The net result is a gain of the square root of two in signal to noise and in cooling performance. We have also implemented gain and phase equalizers in the Debuncher, which provided an increase in the system effective bandwidth.

The optical notch filters were demonstrated[2] to enhance the cooling performance by about the expected amount last year. The number of TWT's in the system will be doubled in the summer. Together the optical notch filter and increased power will nearly compensate for the reduced sensitivity caused by increasing the electrode gaps.

6. Debuncher stochastic cooling: longitudinal

There are several advantages to Debuncher longitudinal cooling. First, the stacking will be improved by making the momentum spread wider. Currently, the accumulator stacking cavity does not produce enough voltage to stack all the beam that has been rotated in the Debuncher. This was already true when we were trying to rotate 3% momentum spread in the Debuncher - it is even more true now that we are trying to rotate 4%. While it would be possible to increase the stacking voltage, it would be rather expensive. One cannot simply add cavities because the Z/n limit is already nearly reached with the existing cavities. Furthermore, a wider momentum spread would only aggravate existing problems in the stack tail system. Second, the momentum cooling also has the nice feature that it performs a "cleanup" after bunch rotation, collecting the long tails on the momentum distribution after bunch rotation, due to the inherently non-linear nature of the process. Third, if the cooling works as well as we expect the rms width of the distribution presented to the stack-tail would be reduced compared to the current width. Consequently, the stack-tail gain would be reduced, which will reduce the betatron heating of the core by the stack tail and increase the stability of the cooling system. This will be particularly important in rapid cycle operation with "multi-batch" targeting, when the stack-tail gain must be increased to cope with the higher flux. Finally, the requirements on the bunch narrowing process in the Main Ring prior to extraction for pbar production would be less severe, because the momentum cooling can compensate for some inadequacies in the bunch rotation. This will be important, because the bunch narrowing process suffers inevitably in the "multi-batch" Main Ring operation. Debuncher momentum cooling will make the Pbar Source less sensitive to the proton longitudinal emittance and bunch shape at 120 GeV.

The Debuncher momentum cooling system will be a high-power 2-4 GHz system, with typically 1600 watts of power (mostly thermal). The system will initially use the existing pickups and kickers. Later the pickups and kickers will be replaced for both transverse and longitudinal cooling systems. Costs will be minimized by reusing the existing vacuum tanks. A high performance notch filter will be developed for the momentum cooling system.

7. Targeting

Attempts to increase the pbar yield at the target favor the use of heavy metal targets, and proton spot sizes as small as possible; the proton beam intensity should simultaneously be as high as the Main Ring can provide. Figure 3.7.1 illustrates the sensitivity of the yield to the spot size. Improvements in the tune of the AP-1 transport line have made spot sizes of 0.15 mm possible. This spot size is nearly optimal. However, increases in main ring intensity may come at the price of higher intensities. For this reason, we are exploring the possibility of a small radius pre-focusing lithium lens, located a few meters upstream from the target that could provide a substantial reduction in the spot size should the spot size grow any larger than its present 0.15 mm.

The energy density deposition in the target sets a limit on the primary proton beam density in the target. Experience in 1985 with the original design target material (a tungsten-rhenium alloy) revealed that the material failed after only a small fraction of its originally expected lifetime. During the 1987 collider run, copper targets were used for most of the run, with several week tests of tantalum and heavymet (tungsten-copper) near the end of the run. The copper yielded 10% less pbars than the heavy metals, but showed no sign of deterioration. The tantalum suffered pronounced swelling; the heavymet showed severe cracking.

A review of the calculations on which the original design choice of tungsten-rhenium was made have revealed[3] that the energy density deposition is much greater than the original estimate. Most of the energy is associated with electromagnetic showers in the heavy metal; for the Tev I design beam parameters, the tungsten is heated locally at the beam core to close to its melting point on each pulse. In such a situation, failure of the kind which was seen is not surprising. The situation is much better in copper because of the lower Z: the electromagnetic energy deposition is much less. The ductility of the copper is better than that of the heavier metals also, reducing its susceptibility to the thermal shocks generated by the beam.

Experimental tests of heavy metal candidates like tantalum and heavymet will continue, but the expectation is that one must limit the energy density deposition (and hence the proton beam intensity or spot size) severely

Figure 3.7.1

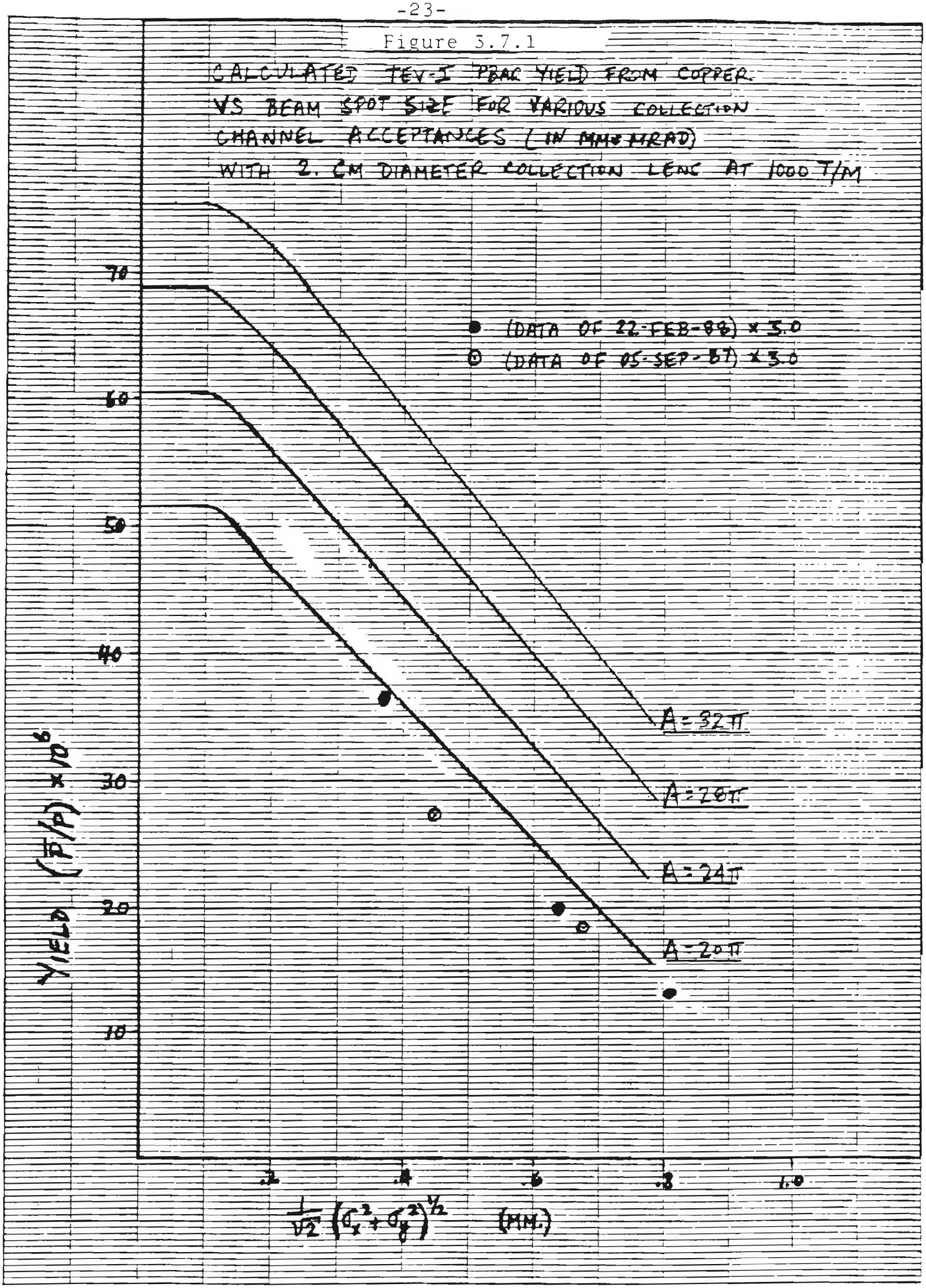

to be able to use these targets. Figure 3.7.2 (from ref. 3) illustrates the calculated limits on the number of protons and the proton spot size from recent calculations of energy density deposition (assuming a uniform limit for all materials of 200 Joules/gram). However, we know that these results are conservative for copper targets since our normal running point of 1.7×10^{12} protons in a 0.15 mm spot size exceeds the calculated limit. We believe, however, that we are near the limits of the structural integrity of the copper target since we already (according to calculations) have some local melting in the target.

Thus a method to decrease the energy density deposited by the beam in the target will soon be needed. This can be accomplished by the use of a sweeping system: a fast kicker which sweeps the beam across the target during the duration of the beam spill. To maintain the advantages in pbar production of the increased intensity and smaller spot size which this allows, the acceptance of the pbar collection system must also be swept, requiring another fast kicker downstream from the collection lens.

A second major issue in the area of targeting involves the collection lens technology. We are using, at present, a 1 cm radius lithium lens, at a gradient of 800 T/m, which is optimized for the present acceptance of the Debuncher. The lens was designed for a repetition period of 2 sec. The implementation of the "multi-batch" technique requires a cycle period of 1.5 sec. Last year, the existing lens was tested at this cycle rate, and was found to function satisfactorily. However, this is about the limit which it can handle reliably.

Higher gradient lenses are also anticipated to be required. Although the present lens gradient is optimum for the present, a 1000 T/m gradient lens will be required to fully capitalize on the increased (28 π mm-mrad) aperture. The present collection lens has a lifetime of 300,000 pulses when operated at 1000 T/m, after which it suffers fatigue failure. Improvements to certain welds in the present lens design, which appear to be the limiting design features, are being implemented. These improvements may enable the present design to operate reliability at 1000 T/m. Another possibility is the use of a lens of the CERN design, which was tested at Fermilab last year for 1,000,000 pulses at 1000 T/m. It is fully compatible with our transformer and target station environment.

A third major issue in the targeting area relates to reliability. Because all of the components of the target station are in a very severe radiation environment, reliability is a serious issue. The present versions of the lithium lens transformer and a pulsed magnet in the target station are not fully radiation-hard. Although we have not had a failure of the lens transformer for more than two years, the pulsed magnet has suffered numerous failures.

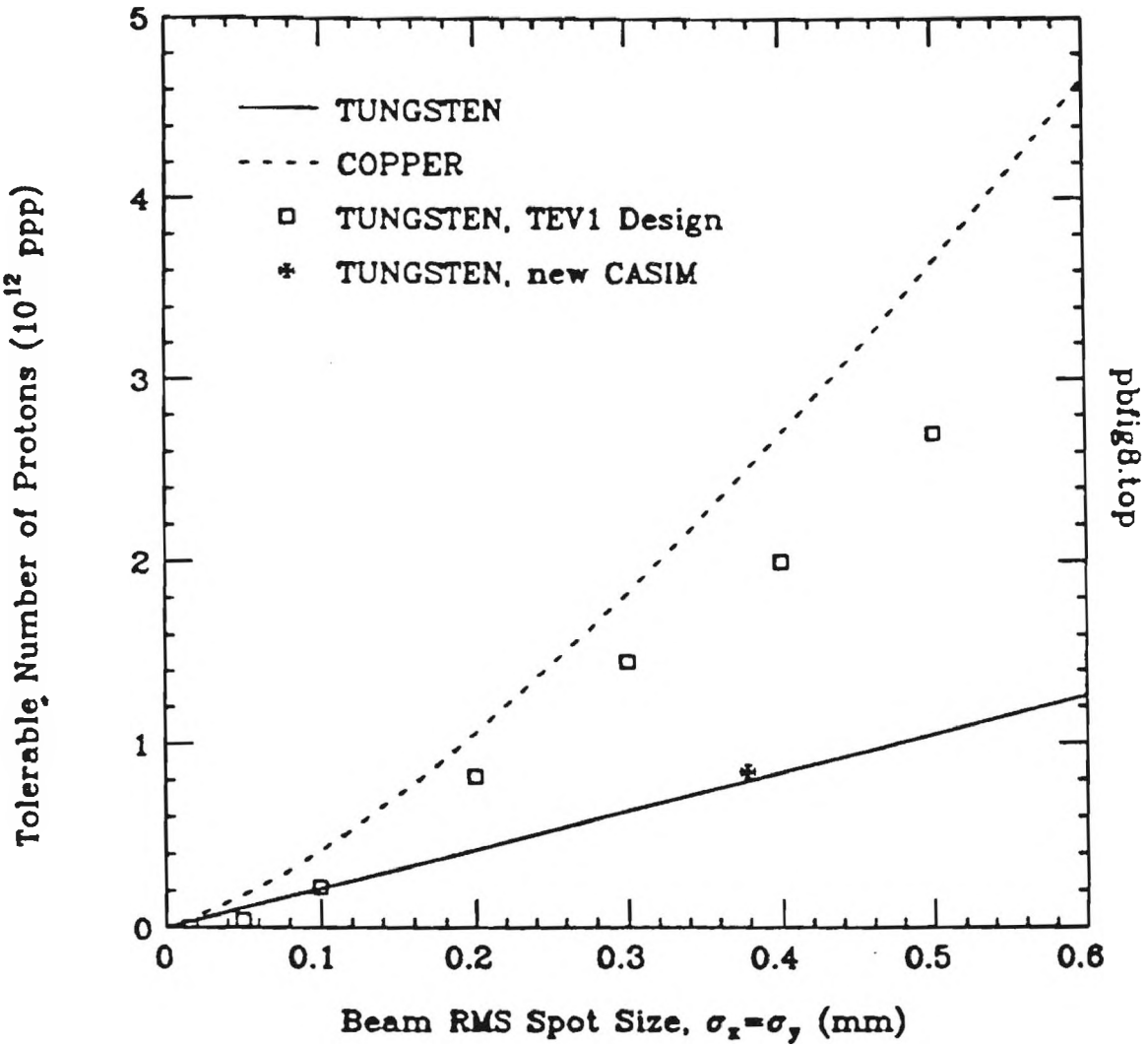

Figure 3.7.2 Tolerable number of protons on the Pbar tungsten and copper targets at 120 GeV/c as function of the beam spot size. Also shown are tungsten data from Ref. [4] and the new CASIM result.

We have several spares of each component on hand, but the ultimate solution is to provide radiation-hard versions of these devices. A prototype radiation-hard pulse magnet is being constructed. A radiation-hard design for a lens transformer exists at CERN, which could be adopted to our case. This program of radiation hardening will become more important as the proton beam intensity on the target is pushed higher during later stages of phase 1 of the collider upgrade.

8. Accumulator Stochastic Cooling: Core systems

The rapid cycling of the Source required by the "multi-batch" technique mode of operation of the Main Ring for pbar production places heavy demand on all the Source cooling systems. These demands will require higher bandwidth cooling systems for the Source. For this reason, in 1987 we embarked on a vigorous R&D effort in the design of pickups, kickers and preamplifier electronics which can operate in the 4-8 GHz frequency band. We designed a prototype pickup assembly and tested it on the bench. Considerable work was also done on low-noise wide-band pre-amplifiers. We also initiated the procurements for long-lead-time 4-8 GHZ TWT's and some associated electronics. A full prototype pickup system consisting of 8 pickup arrays of 8 pickups each, together with combiner boards, was constructed, and tested in the Debuncher in early in 1988. The prototype beam tests have provided valuable guidance in the design of an operational system.

The Accumulator core has been chosen as the first place to implement a 4-8 GHz cooling system for two reasons. First, it is a relatively inexpensive, low power system, which can be implemented rapidly. Second, it will provide immediate benefit in two ways:

(a). During pbar stacking, it will help to counteract the increased stack-tail heating of the core which will result from the higher stack-tail gain needed for the more rapid cycle rate associated with "multi-batch" operation; and

(b). the pbar emittance in the core will be reduced, so that smaller beams can be sent back to the Main Ring and Tevatron for collider operation. In general, this will make the pbar transfer efficiency better and, if the smaller emittance can be preserved to low beta, the collider luminosity will increase.

9. Accumulator Stochastic Cooling: Stack Tail system

In an important experiment carried out using Booster protons during the early part of 1988, the Accumulator stack tail system has demonstrated the ability to stack at a rate of about $3x10^{10}$/hr up to a stack in excess of $9x10^{11}$. Figure 3.9.1 shows the development of the core intensity and transverse emittances with time during this experiment; the notable feature is the relatively constant slope of the core intensity, indicating no major decrease in stacking efficiency during the experiment. Stacks of more than $8x10^{10}$ anti-protons have been achieved during normal operation. The stacking rate with stacks of this size is slightly over $1x10^{10}$ anti-protons per hour.

Although the results of the proton stacking experiment are gratifying in terms of prospects for the Source upgrade, it should be noted that the proton stacking rate was still less than half that which is anticipated for the pbars as the ultimate goal of phase 1 of the upgrade. While the stack tail system was originally designed for a flux of $10x^{10}$ per hour, the highest sustained stacking rate thus far achieved is $3x10^{10}$. We are not aware of any reason which would make it impossible to achieve the design rate, but we suspect that some modifications of the system may be required. It is of prime importance to perform experiments to define what these modifications may be.

The cycle period in the proton stacking experiment was 3 sec; normal anti-proton stacking uses a 2.6 sec cycle. Operation of the stack tail system with a 1.5 sec repetition period (as required for multi-batch operation) will require an increase in the system gain. This will have two consequences: an increase in the betatron heating of the core (this has been addressed above in connection with the core system upgrade), and an increase in the susceptibility of the system to instabilities. This latter problem, which was an operational concern at times even during single-batch stacking, appears to have been controlled by the installation in December 1988 of ferrite dampers in the stack tail pickups. Previously we had identified microwave mode problems in the core pickups and were able to reduce them significantly with resistive film dampers. The new 4-8 GHz pickups are expected to have superior mode suppression to the existing core cooling system.

References:

1. G. Dugan, "Pbar Yield Measurements vs. Debuncher Acceptance and comparison with predictions", Pbar Note 474, Fermilab.

2. R. Pasquinelli, W. Kells, D. Peterson, "Optical Correlator Notch Filters for Fermilab Debuncher Betatron Stochastic Cooling", APS spring meeting, April 1988.

CONSOLE LOCATION 02, MCR-N2 30-APR-1988 18:10
Data Log Plot Package

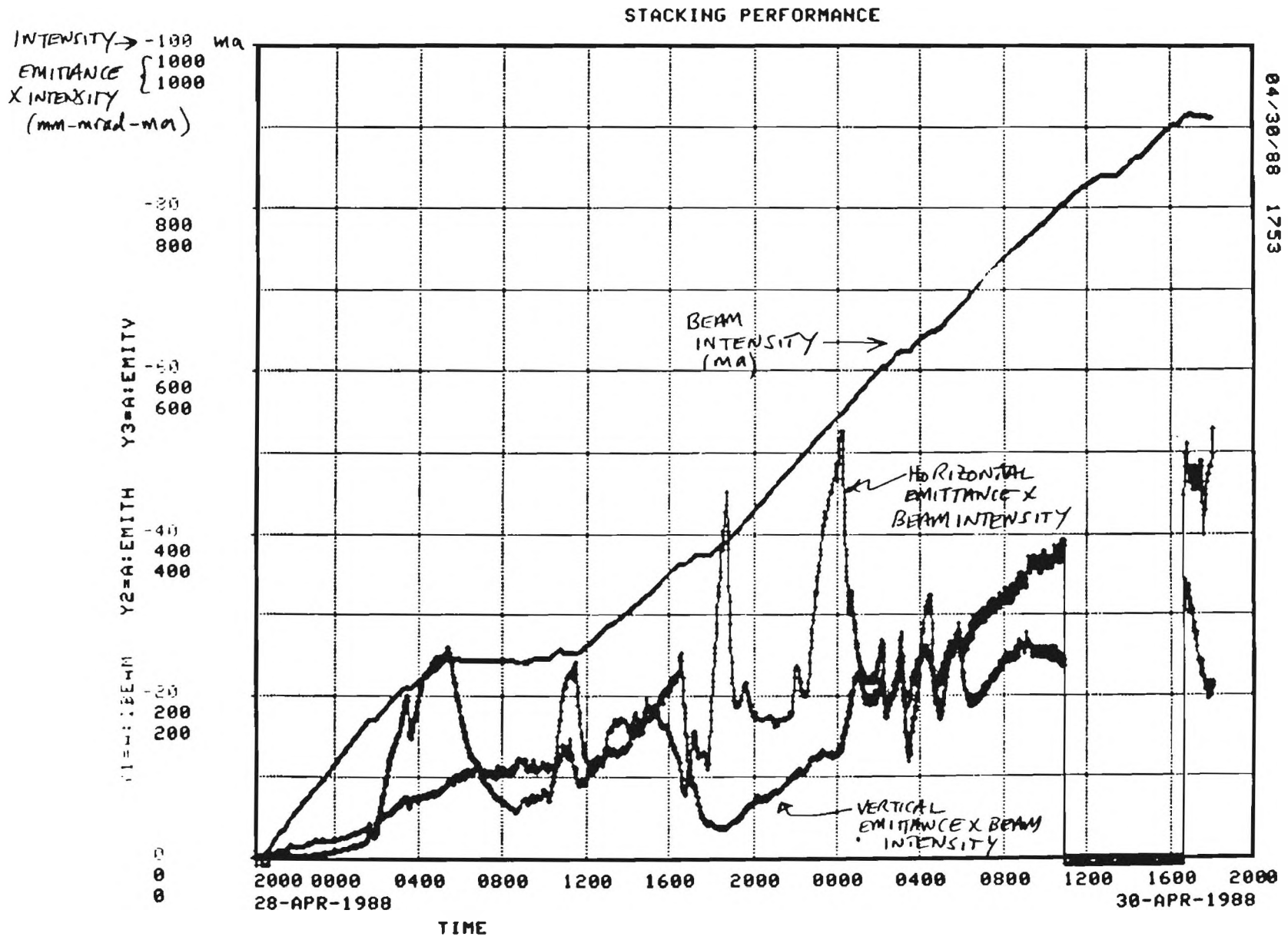

Figure 3.9.1

3. I. L. Azhgirey, N. V. Mokhov, "Antiproton Production and Energy Density Limitations in Targets for the Fermilab Pbar Source", TM-1529, Fermilab

IV. TEVATRON ORBIT SEPARATION DESIGN

1. HELICAL ORBITS AND APERTURE LIMITATIONS

In this section we describe an arrangement of electrostatic separators in the Tevatron to create helical beams. The same set of separators is used at injection and during acceleration, squeeze to low beta, and to make collisions at both intersection regions. The separators will fit in existing warm spaces; thus existence of 6 T dipoles is not required.

A sequence, as used in this discussion, is a series of steps going from injection to collisions and data taking. The parameters defining each step are the energy, the step number in the low beta squeezes (in principle, they can be different at the two experiments), and a set of separator voltages. At each step vertical and horizontal single beam closed orbits have been calculated and the beam-beam separation as well as the helix orientation determined. With the additional assumption of the beam properties the total separation in σ's between proton and anti-proton beams can be calculated. The beam properties assumed in these calculations are $\epsilon_H = \epsilon_V = 15\pi$, and a $\Delta p =$ that varies linearly from 75 MeV at 150 GeV to 112 MeV at 1000 GeV. The transverse normalized emittances are 95% figures, and the momentum spread is one σ. All distributions are assumed to be Gaussian. At injection, before the beams have had time to dilute due to intrabeam scattering, more optimistic values could have been used in the calculations. It is unclear if it is correct to assume that a given separation in σ's in momentum space is equivalent in its beam-beam effects to the same number of σ's of separation in betatron space, and therefore it may not be correct to combine horizontal Gausssian widths in momentum and betatron space in quadrature as has been done.

The details of the design of the system are a delicate balancing act between having sufficient separation so the long range beam-beam forces do not degrade the beam quality, while at the same time staying within the accelerator aperture. The design goals were minimum separation of 5 σ's and maximum separation of 15 mm (beam-beam center to center). As the tables and graphs show, the solution falls short of these goals in some instances.

2. INCORPORATION INTO THE LATTICE

The lattice for these calculations uses the low beta insertions at <u>both</u> BØ and DØ as described in section VI, (refs 1 & 2). These insertions are

matched in betatron and momentum space. The tune of the ring is set at: $\nu_x = 20.58$ $\nu_y = 20.59$. The beam is squeezed with $\beta_x = \beta_y$ starting from injection values of $\beta^* = 170$ cm (step 1) down to $\beta^* = 25$ cm (step 17). The only difference from Collins' original design is that one of the correctors has been moved further into the lattice to avoid the Tevatron feed can and the correctors are at unequal currents across the straight section. The figures below summarize the elements in the insertion and use the notation of ref 7.:

-43----44---46-----47-IP-13-----14---16----17-
-T9---T8---T7---T6-----T6'---T7'--T8'--T9'

and with the straight section expanded:

-48----49----------IP----------11----12-
-Q5---Q1--------Q2-Q3-Q4----Q4-Q3-Q2--------Q1---Q5-

Injection requires cogging. Furthermore, if injection is done at step 1 in the squeeze then the "natural" helix (defined below) is not well enough developed to allow collisions to begin. So the sequence proceeds through a series of steps during which the beams are separated in the entire ring. Then at some energy, and some step number in the squeeze the beams are brought into collision. Precisely at where this transition from no collisions to collisions occurs will depend on the aperture and the separator voltages.

There is furthermore an uncertainty about what happens to the beams during this transition. Clearly, there will be a period lasting for some thousands of revolutions (depends on the separator time constants) when the beams are "grazing", i.e. $< 5\ \sigma$ apart. Accelerator experiments are needed to determine how rapidly the transition between these two states must be made.

Once collisions begin the oppositely charged beams are kept apart except at the BØ and DØ experiments with local electrostatic "three bumps" in each plane. One pair of bumps creates helical orbits from B11 to C49. The other pair of bumps keeps the beams apart from D11 to A49. The high-β regions closest to the interaction region are used to obtain efficient separation, while getting the beams separated as soon as possible to minimize the number of head on crossings. This results in the geometry sketched below.

```
    BØ                                                          D
Ø   DØ                                                          B
Ø
    B11-→-→-→-→-→-→-→C49                  D11-→-→-→-→-→-→-→-→-→-→-→-→-→-A49
                  1/3 ring                                        2
/3 ring
```

≃ 6.5 betatron oscillations ≃
13 betatron oscillations

Since the number of betatron oscillations in these bumps is only approximately an integer or half-integer, the local bumps require 3 elements. After some trial and error the locations for the middle element of the 3-bumps in the vertical plane were chosen to be C17 and F17. The vertical 3-bump from DØ to BØ works well until β^* goes below 50 cm; then the F17 location is no longer effective in the vertical plane and an electrostatic kick needs to be turned on somewhere in the FØ straight section. There is room in the F17 medium straight section to also accomodate the middle element of the horizontal DØ to BØ 3-bump.

The horizontal plane "middle" element of the BØ - DØ 3-bump is more of a problem. For best separation, B48 is chosen, but there is interference with the existing pbar abort kicker. If B48 were not available then one could relax the requirement that the same set of separators be used during injection, and during collisions. Then one could use a horizontal separator at F48 before the beams are brought into collision and then turn it off and during collisions use a horizontal separator somewhere in the CØ straight section to provide the middle element of the BØ - DØ 3-bump. However, the calculations show that this works less well than the B48-C17 arrangement, so it should be regarded only as a fall back position if the abort system cannot be reconfigured to free up the 6 meter space at B48 and the 12 meter space at C17.

For this particular choice of separator locations and strengths the result is almost round helices when $\beta^* \sim 50$ cm (step 12). The reason for this is that with the separators placed at the "11" and "49" locations, there is close to a 90° phase shift ($\Delta\Phi$) between the vertical and horizontal betatron oscillations in the accelerator arcs. This "natural" vertical-horizontal phase difference decreases as β^* increases. At injection values of β^* near 2 m a nice helix can no longer be obtained with the separator geometry that works well for $\beta^* = 50$ cm. $\Delta\Phi$ is close to 20° degrees and the helix collapses. One approach for solving this problem would be to use additional correction elements to maintain the vertical-horizontal phase difference in the arcs as the beam is squeezed. However, this idea will not be pursued further in this report.

The helical separation solution

The sequence is best presented as a path in a 2-dimensional space (figure 4.2.1) where the axes are Tevatron energy, and β^* (or step number in the squeeze or, correlated with these parameters, β_{max}). It is desirable, though

not essential, for experiments to be able to run at energies as low as 315 GeV for comparison with CERN data, and also to have a range of β^* over which collisions can be observed. It is also desirable, and in principle possible with the matched low-β insertions, to have available as an operations parameter the ratio of luminosities at the two colliding beam regions.

The end points in figure 4.2.1 are

* 150 GeV, no collisions, β^* at both experiments 170 cm (step 1) and

* 1500 GeV, collisions, β^* at both experiments 25 cm (step 17).

The 1500 GeV point is included because one of the upgrade options currently under discussion is to build a 1500 GeV "new Tevatron" in the present tunnel. The calculations that have been done assume separated beams at 1500 GeV with the present Tevatron lattice. It appears that adequate separation between protons and antiprotons can be achieved although separator voltages are high. However, by the time this is contemplated experimental information will be in hand on spark rate vs. separator voltage and minimum beam separation requirements. Also it is likely that the lattice will be different.

The path chosen to go between the two end points depends on several considerations. During injection the beams must be separated everywhere while cogging occurs. Aperture limitations will prevent low energy operation at a high step number in the low β squeeze. However, until one reaches at least step 4, i.e. $\beta^* = 110$ cm, the helix has not developed sufficiently to allow the beams be brought into collision. At step 4 in the squeeze, β_{max} is about 350 m, and $\Delta\Phi$ is 45°. It should be noted that $\sigma = 2.3$ mm at 150 GeV and $\beta_{max} = 350$ m. This can be compared with a beam-beam separation that varies from 5 to 15 mm. (figure 4.2.2). Thus, if the Tevatron aperture can accomodate this amount of separation, it should be possible to inject at step 4 or more in the squeeze.

Another important constraint is the maximum voltage on the separators. In the proposed sequences the goal was to hold the separator electric field below 40 kV/cm during periods lasting the order of minutes (i.e. injection, cogging, acceleration), and below 25 kV/cm during periods lasting hours, i.e. during collisions and data taking runs. However, the solution falls short of these goals in some instances. It is important to emphasize that many of the factors affecting the design and proposed sequence need to be measured in accelerator experiments. These are discussed below.

Accelerator Experiments

Aperture requirements for the two beams must be studied in detail. With the strong nonlinear field components in superconducting magnets, the dynamic aperture is limited. The effects on the stored beams of operating off axis in the magnet aperture has been studied in accelerator experiments. Calculations using the tracking program TEVLAT have been made to try and reproduce the observed changes in tune as a function of position. More work is needed. A set of ν and ξ corrections on the helical orbit will be needed. Calculation of these effects are difficult and it is planned to install some electrostatic separators in the Tevatron at as early a date as possible in order to determine the magnitude of the effects experimentally. The effect of beam-beam forces at the collision point must also be evaluated.

Prototype electrostatic separators are under construction. Spark rates will be measured and various solutions for feed-through insulators will be studied experimentally. The high voltage power supplies required for the separators will be specified and initial prototype units obtained. The time constants for increasing and decreasing the separator voltages will be measured. It is important to determine spark rates vs. electric field with beams passing through the separators.

Summary of the proposed helical solution

* Beams injected at 150 GeV, separated at all locations around the ring allowing cogging, step 1 in the squeeze, $\beta^* = 170$ cm.

* Beams accelerated to 315 GeV, low beta squeeze through step 4 ($\beta^* = 110$ cm) or step 6 ($\beta^* = 90$ cm), beams still separated at all points around the ring.

* At either step 4 or step 6 in the low β squeeze, at 315 GeV, the beams are brought into collision at both experiments.

* With low β at step 6 the machine is ramped up to 600 GeV. The reason one cannot go all the way to 1000 GeV and then squeeze has to do with separator voltage limits.

* At 600 GeV the low beta can squeeze the beams further to step 12 ($\beta^* = 50$ cm).

* Accelerate to 1000 GeV and squeeze (if desired) to step 17 ($\beta^* = 25$ cm).

3. BUNCH SPACING SCENARIOS

It is desirable to retain the present 53 MHz, n=1113 (harmonic number), Main Ring and TEVATRON rf systems. If B = 53, there are 106 crossing points, spaced 59.3 meters apart. So with one collision point at BØ and one at DØ, at the nearest other crossings, the beams have reached almost their full separation of about 5 σ's. Minimum time between bunches is 396 ns.

If one is more ambitious and uses B = 159, then the crossing points are 19.8 meters apart. This gives three collisions each at BØ and DØ, plus at each of these straight sections two more places where there are "near" collisions, of < 2 σ separation. (figure 4.3.1). These extra "4" crossings can be increased to almost 3 σ with the use of cold, i.e. superfluid (1.8^{o} K) triplets which are shorter and therefore allow moving the separators closer to the interaction point. (ref 4). It is believed, although accelerator experiments need to be carried out, and further calculations performed, that these small separations will cause unacceptably large tune spreads. Minimum time betweeen bunches is 132 ns.

In each case only some of the subharmonic buckets available will be used and the filled ones can be distributed in a pattern to maximize the number of collisions at both BØ and DØ, and still leave gaps for kickers to rise and fall. If the number of filled buckets is small, e.g. in the 6-bunch vertical plane only separation discussed in the next section, additional freedom is available in the pattern to reduce difficulties caused by cogging.

4. BEAM SEPARATOR HARDWARE

Design efforts for the proton-antiproton electrostatic separator system are focused on providing maximum separator voltage consistent with virtually no sparks, which effectively destroys the antiproton beam. The goal is for an operational capability at up to 50 KV/cm, for a 5 cm electrode gap.

Significant inputs for the separator design have been obtained from the initial CERN experience and from FNAL fixed target electrostatic septa design.

Operational experience of the CERN separator system has indicated a sparking voltage limit of ~ 30 KV/cm, with a requirement for vacuum levels of a few x 10^{-10} Torr needed to achieve this. A comparable voltage capability would provide a usable Tevatron collider system; however,

significant gains in beam lifetimes can be achieved with a separator capability of up to 50 KV/cm, due to higher beam energy at the Tevatron.

Two projected improvements over present CERN design are an electrode shape better optimized to reduce maximum field gradients, and use of dual plus/minus HV power supplies to cut in half absolute voltage levels needed to achieve given electrode electrostatic fields.

The active length of the separator electrodes is determined by space constraints in the Tevatron mini-straight sections. The length chosen for each unit is 2.57m. By comparison, active length for fixed target splitter and extraction septa units is 3.05m.

Optimized high voltage design requires considerable attention to details of shape and surface finish of all components which might contribute to electrostatic field gradients. As seen in the cross-section figure 4.4.1, design of the electrodes and vacuum vessel has eliminated sharp edges which would enhance field gradients. Design of electrodes and vacuum vessel was as an integral unit. Maximum field gradient is expected to occur between the two electrodes, with only a few percent variation between peak and average gradients.

Surface finish of the electrodes will be polished to a granule size of $\leq$ 8 microns. In addition, cleaning of the complete system must be tightly controlled. Use of a multistage cleaning process is projected, to include both vapor degreasing and ultrasonic cleaning. Elimination of hydrocarbons from the system is a necessity.

High voltage capability is being designed for $\pm$ 180 KV to each separator electrode. This produces a maximum field strength of 360 KV across the 5 cm gap, or 72 KV/cm. High voltage conditioning at fields significantly above operating levels is necessary for minimizing sparks during operation.

Need for an ultra high vacuum requirement in the 10^{-10} Torr range is due to sparking problems which would otherwise be caused by beam-gas interactions in the electrode region. CERN's experience has been that separator operation at a few x 10^{-9} Torr is not viable. No experience from the fixed target electrostatic septa operation is relevant here, as for the extraction septa the intense circulating beam remains outside the field region. Separator operation, in contrast, requires the circulating beams positioned in the region of maximum field gradients.

To achieve these vacuum levels, all systems must be baked to 400^{o}C. Additionally, hydrogen degassing at 950^{o}C will be required for the stainless electrode and vacuum vessel assemblies. Each separator unit will be

ELECTROSTATIC SEPARATOR
CROSS SECTION VIEW

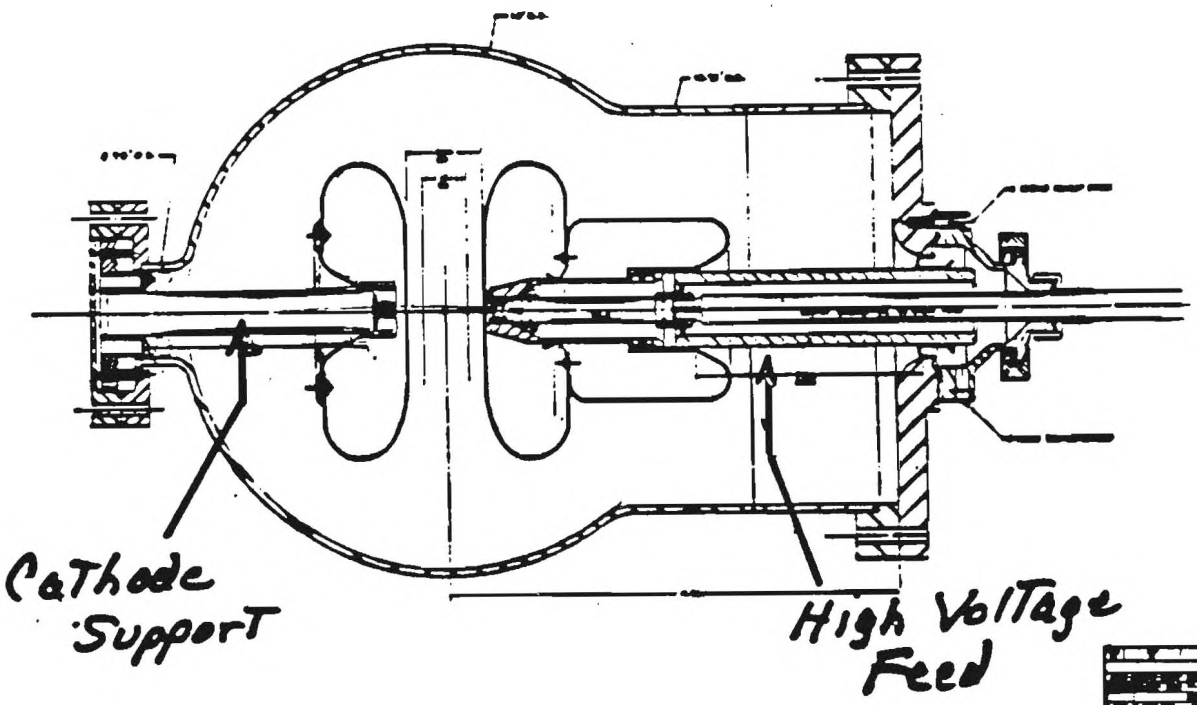

VACUUM VESSEL

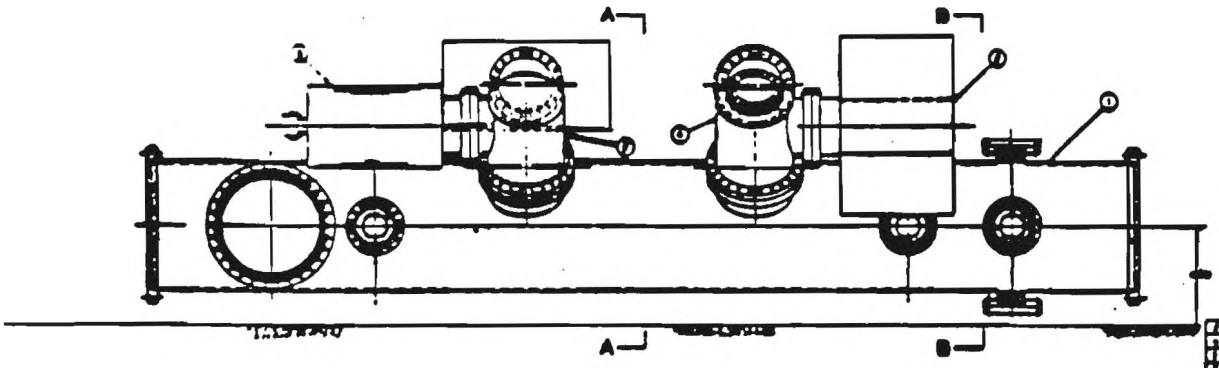

Fibure 4.4.1

continuously pumped with dual ion pumps and Titanium sublimation pumps to achieve required vacuum levels.

5. VERTICAL SEPARATION OPTION

Given the complexity of the solution presented above and the uncertainties of separating in the horizontal plane due to momentum spread, it is interesting to consider separating only in the vertical plane. As with the helical solution the hardest part of the sequence occurs at injection. A cusp in one plane at one point in the closed orbit generates roughly 20 betatron oscillations around the circumference. With two beams "cusped" in opposite directions, the beams come together every $\lambda/2$ or in roughly 40 places. The present 6-bunch cogging operation sweeps the azimuthal position through 56 buckets or about 1/20 of the circumference. Therefore the beams can start out not colliding, and end up not colliding, but the cogging operation sweeps them through azimuthal positions where they collide (and graze which is worse). Some horizontal plane separation must be introduced. This can be turned off after cogging is complete and from that point onward in the sequence separation is only in the vertical plane. Fewer separators are required than in the helical case but not by as much as one might think since the requirement of $> 5\sigma$ is still a design goal.

6. RESULTS

An important operational implication to either the helical or vertical separation proposal is the following. In contrast to current operation where the beam is first accelerated to maximum energy and then the low beta insertions go through their stepwise program from step 1 to step 17, it now becomes necessary to change β^* as a function of energy. The implications of figures 1 and 10 which show the path in E - β^* space are that the Tevatron has a "front-porch" at 315 GeV and another one at 600 GeV. This may be difficult or impossible due to persistent currents. If so the crude sequences shown will have to be divided up into many fine steps and the sequence run adiabatically enough so that the low beta quads, and the separators can track each other as well as the accelerator energy with adequate precision so the tune remains nearly constant and the closed orbits approximate those shown in the figures.

Tables 4.6.1 - 4.6.5, catalog the number of separator modules required and their voltage programs. The electric fields in the tables are based on a "standard" module with a physical length of 305 cm and an effective length of 257 cm (ref 5). If it is operated at 25 kV/cm ($\pm$ 50 kV on a 4 cm gap or $\pm$ 62.5 kV on a 5 cm gap) it will deflect a 1 TeV beam 6.4 μrad. This

is the unit kick used in the tables presented below. The calculations have been done assuming a point kick. A distributed kick is slightly larger for the same electric field. (ref 6). The separators being built can operate in excess of 50 kV/cm but it is not yet known what the spark rate will be as a function of electric field.

In addition to the modules a certain number of reversing switches are required. The minimum number is 2 in both the helical and vertical separation scheme: on the B48 set and on the C17 set. This is necessary to set up the pbar closed orbit using reverse injection and protons.

Details of the helical separation solution are presented in Tables 4.6.1 - 4.6.3 and figures 4.6.1 - 4.6.9. Figure 4.6.1 shows the sequence in E - β^* space. Figure 4.6.2 shows total beam-beam (center-center) separations at injection, 150 GeV and step 1. The top part of the figure shows the separation in mm. The total aperture requirement would be these numbers plus a certain number of σ's for each beam. The lower portion shows the separation in σ's using the beam properties described above. In figure 4.6.3 the regions near BØ and DØ are expanded. In this figure are shown the single beam horizontal and vertical trajectories and also the beam-beam separation in σ's. From this figure it can be seen that the largest aperture requirements of over $\pm$ 7 mm are in the horizontal plane and occur in the new low beta quads: Q5, Q1, Q2, Q3 upstream and the entire triplet and T6 downstream.

Figure 4.6.4 shows the situation with cogging complete and after acceleration to 315 GeV but before the beams are brought into collision. The separation in σ's at steps 1 and 4 are shown. Bunches spaced a minimum of 21 buckets apart are filled in a pattern having 3-fold symmetry around BØ-DØ-FØ. The black diamonds in the figure show the crossing points. As long as this pattern is maintained and since cogging is complete, what is important is the minimum number of σ's at a crossing point. Raising the energy lessens the aperture problem at BØ and DØ but as the low beta squeeze is applied the problem arises again reflecting the increase in β_{max}. Only the B48 and C17 separators are on through this step. As shown in Tables 4.6.2 and 4.6.3 their voltages are increased slightly as the low beta squeeze is applied.

Figures 4.6.5 and 4.6.6 illustrate the situation at 315 GeV and step 4 after the beams are brought into collision. In figure 4.6.5 the horizontal (solid line) and vertical (dashed line) are single beam trajectories. The "natural" $\Delta\Phi$ of 45° can be seen clearly. Figure 4.6.6 shows the beam-beam separations. With the beams in collision the aperture problems at BØ and DØ have disappeared but there is a new aperture problem at AØ because of the existing high-β insertion there. This problem diminishes as the energy is

raised or at a higher step number and might be an argument to wait until step 6 before bringing the beams into collision at 315 GeV. However, during collider runs A$\emptyset$ can be changed back to a normal-β insertion (by quadrupole polarity reversal) in which case the required aperture in this region will be reduced.

From here it is straightforward to accelerate to 1000 GeV and squeeze further. Figure 4.6.7 shows the beam-beam separations at 1000 GeV and step 12, and figures 4.6.8a and 4.6.9 show the same plots at step 17. Figure 4.6.8b is a 1500 GeV run, also at step 17. At step 17 the minimum 5σ has not quite been achieved at 1000 GeV, so perhaps the voltages should be somewhat higher, and at 1500 GeV the goal has been exceeded, so those voltages, which are quite high could be reduced. Figure 4.6.9 is an expanded view of the upstream half of each collision region. Shown are the single beam horizontal and vertical trajectories and also the beam-beam separation in σ's. From this figure one can see the difficulties that arise with the 7 bucket (20 m) or 9 bucket (25 m) bunch spacing scenarios.

The total number of modules required in the helical separation scheme is 21 as shown in Table 4.6.1. To avoid the F17 horizontal and vertical reversing switches, the number could be increased to 4, raising the total to 23.

Details of the vertical separation solution are presented in Tables 4.6.4 and 4.6.5 and figures 4.6.10 - 4.6.15. Figure 4.6.10 shows the sequence chosen in the 2-dimensional E - β^* space. As before, one starts by considering injection: 150 GeV and step 1. Six bunch operation is assumed. Figure 4.6.11 shows beam-beam separations; the open triangles are crossing points before cogging and the solid diamonds are crossing points after cogging is complete. It is clear from the figure that cogging sweeps each crossing point through zero or small σ configurations. Thus some horizontal separation is necessary until cogging is complete. Even with this "squashed helix", the beams will sweep through 2σ separation and until accelerator experiments are performed it will not be know what the effects of this will be. It is difficult to raise the separator voltages further because of aperture limitations.

Figures 4.6.12 and 4.6.13 show the separations at 315 GeV and step 6 both before and after the beams are brought into collision. In figure 4.6.12 the minimum separation in vertical betatron space is 3.6 σ. The main separator is at C17. A small voltage on one of the other vertical separators seems to help. There is clearly an aperture problem at B$\emptyset$ and D$\emptyset$. This goes away when the beams are colliding (figure 4.6.13) but now there is a severe aperture problem at A$\emptyset$. As remarked on above, in the discussion on the helical solution, this may be solved by reversing A$\emptyset$ quadrupole polarities during collider runs.

Figures 4.6.14 and 4.6.15 are at 1000 GeV. Figure 4.6.14 is at step 12, and figure 4.6.15 is at step 17, but with the local bump from BØ to DØ turned off. So there are now 5 head on collisions. However, the separators at B48 and C17 are still present and used at injection. The total module count of 18 for two head-on collisions is given in Table 4.6.4. The voltages on the B11 group are modest so one could probably have 2 modules there instead of 3 reducing the total to 17. However at F17 instead of having 1 module, it would be better to have 3 modules, one operating at positive polarity and 2 operating at negative polarity. This reduces operating voltages and eliminates a reversing switch and raises the total to 19. If one drops to the 5 head-on collision case then the total number is reduced by 6 although it might be possible to use the F17 separators during injection instead of those at C17 further reducing the total number needed.

Tables

Figure Captions

4.6.1. Helical solution. Sequence chosen in the 2-dimensional E - β^* space.

4.6.2. Helical solution. 150 GeV, step 1. The top part of the figure shows the beam-beam (center-center) separation in mm. The lower portion shows the separation in σ's using the beam properties described in the text. The low β points at BØ and DØ are at azimuthal positions of 2000 and 4095 meters. The minimum separation of 4.03 σ occurs at azimuth 5682 m.

4.6.3. Helical solution. 150 GeV, step 1. Expanded view of (a) the region near BØ and (b) the region near DØ. The single beam horizontal trajectory is the solid line; the single beam vertical trajectory is the long-dashed line. Their scale is on the left. The short-dashed line with scale on the right is the beam-beam separation in σ's.

4.6.4. Helical solution. Separation in σ's at two different steps in the sequence before the beams are brought into collision. The black diamonds show the crossing points assuming 21-bucket spacing. 3 groups of 15 bunches each (3-fold symmetry) cross in the 87 places shown.

(a) 315 GeV, step 1

(b) 315 GeV, step 4. The minimum separation of 3.64 σ occurs at azimuth 5682 meters, but fortunately this is not a crossing point.

4.6.5. Helical solution. 315 GeV, step 4 after beams are brought into collision. Horizontal (solid line) and vertical (dashed line) single beam trajectories. Note that the "helicity" shown in this figure does not correspond to the separator polarities in Tables II and III.

4.6.6. Helical solution. 315 GeV, step 4 after beams are in collision. Shown are the beam-beam separation in mm (top) and in σ's (bottom).

4.6.7. Helical solution. 1000 GeV, step 12.

4.6.8. Helical solution. Separation in σ's at two different steps in the sequence after the beams are brought into collision.

(a) 1000 GeV, step 17.
(b) 1500 GeV, step 17.

4.6.9. Helical solution. 1000 GeV, step 17. Expanded view of (a) the region near BØ and (b) the region near DØ. see figure 3 caption for legend.

4.6.10. Vertical solution. Sequence chosen in the 2-dimensional E - β^* space.

4.6.11. Vertical solution. 150 GeV, step 1, 6 bunch operation. In the lower part of the figure the open triangles are the crossing points before cogging and the solid diamonds are the crossing points after cogging is complete.

4.6.12. Vertical solution. 315 GeV, step 6, before the beams are brought into collision.

4.6.13. Vertical solution. 315 GeV, step 6, after the beams are brought into collision.

4.6.14. Vertical solution. 1000 GeV, step 12 with beams in collision.

4.6.15. Vertical solution. 1000 GeV, step 17 with the local bump separators leaving out the separators at B11 and C49. This eliminates the vertical BØ and DØ local bump. However, the separators at B48 and C17 are still present and used at injection.

References.

1. T. Collins, "On the design of LOW-BETAS for BØ and DØ", Apr.,'87.

2. Karl Koepke: "BØ/DØ Low Beta Lattice", July 1, 1987. "BØ/DØ Low Beta Lattice--Revision 1", Sept. 24, 1987.

3. E. Malamud, "An Electrostatic Separator Scheme for the Tevatron", Sept. 1, 1987; Mar. 17, 1988.

4. E. Malamud, "Comparison of Superfluid and Regular Triplets for β^* = 50 cm", November 28, 1987.

5. S. Childress.

6. G. Goderre.

7. Tevatron Low-Beta Quadrupoles: Requirements and Specifications. "Pink Book". July 25, 1988. (revised periodically).

TABLE 4.6.1: HELICAL SEPARATION SCHEME

NUMBER OF SEPARATOR MODULES and THEIR LOCATIONS

Location, if $\beta^* \geq 50$ cm			allowing β^* to reach 25 cm	
	Horizontal	Vertical	Horizontal	Vertical
A49	1	2	1	2
B11	2	1	2	1
C49	1	2	1	2
D11	2	1	2	1
C17		2		4
B48	2		2	
F17	1	1	1	1
F0				1
TOTAL	9	9	9	12
Grand Total	18		21	

TABLE 4.6.2: HELICAL SEPARATION SCHEME

HORIZONTAL SEPARATOR VOLTAGE PROGRAMS (kV/cm)

STEP	GeV	β^*	β_{max}	A49	B11	B48	C49	D11	F17
<u>no collisions</u>									
1-A	150	170	241			43.9			
1-B	315	170	241			43.9			
2	315	143	265			45.7			
3	315	125	305			47.5			
4-A	315	110	351			49.2			
<u>collisions</u>									
4-B	315	110	351	-34.4	25.8	16.5	44.5	25.8	1.9
6	315	87	442	-33.2	25.8	17.8	40.9	25.8	-0.5
6	600	87	442	* * * same as above * * *					
12	600	50	789	-32.2	25.8	22.1	34.1	25.8	-5.1
12	1000	50	789	* * * same as above * * *					
17	1000	25	1614	-37.2	29.3	39.8	37.3	29.3	-15.8
17	1500	25	1614	-55.9	43.9	59.7	53.9	43.9	-23.8

TABLE 4.6.3: HELICAL SEPARATION SCHEME

VERTICAL SEPARATOR VOLTAGE PROGRAMS (kV/cm)

STEP	GeV	β^*	β_{max}	A49	B11	C17	C49	D11	FØ	F17
<u>no collisions</u>										
1-A	150	170	252				20.5			
1-B	315	170	252				20.5			
2	315	143	264				22.9			
3	315	125	305				25.3			
4-A	315	110	345				27.7			
<u>collisions</u>										
4-B	315	110	345	-30.7	-28.2	8.1	-15.5	35.6		15.0
6	315	87	441	-31.2	-28.2	9.5	-16.9	35.6		13.8
6	600	87	441	* * * same as above * * *						
12	600	50	784	-27.5	-28.2	14.4	-20.6	35.6		-6.0
12	1000	50	784	* * * same as above * * *						
17	1000	25	1614	-35.8	-39.0	34.4	-29.7	38.9	-31.5	
17	1500	25	1614	-53.6	-58.4	51.7	-44.5	58.4	-47.2	

TABLE 4.6.4: VERTICAL SEPARATION SCHEME

NUMBER OF SEPARATOR MODULES and THEIR LOCATIONS

One horizontal separator module is required at B48. It is operated at 29.3 kV/cm until cogging is completed.

Vertical modules required are

A49	3
B11	3
C17	4
C49	3
D11	3
F17	1
TOTAL	17
Grand TOTAL	18

TABLE 4.6.5: VERTICAL SEPARATION SCHEME

VERTICAL SEPARATOR VOLTAGE PROGRAMS (kV/cm)

STEP	GeV	β^*	β_{max}	A49	B11	C17	C49	D11	F17
<u>no collisions--cogging</u>									
1-A	150	170	252			29.3			
<u>no collisions</u>									
1-B	150	170	252			29.3			
2	150	143	264			29.3			
3-A	150	125	305			29.3		2.93	
3-B	315	125	305			46.1		6.2	
6-A	315	87	441			46.1		4.1	
<u>collisions</u>									
6-B	315	87	441	-26.4	-11.9	11.9	-14.3	15.0	17.5
6-C	600	87	441	-38.6	-17.4	17.4	-20.8	22.0	25.7
12	600	50	784	-33.8	-17.4	26.5	-25.3	22.0	-11.9
12	1000	50	784	-36.6	-18.9	28.7	-27.4	23.8	-11.9
17	1000	25	1614	-23.8	-13.0	34.3	-19.8	13.0	33.7
17	1500	25	1614	-25.2	-13.7	36.3	-20.8	13.7	33.2

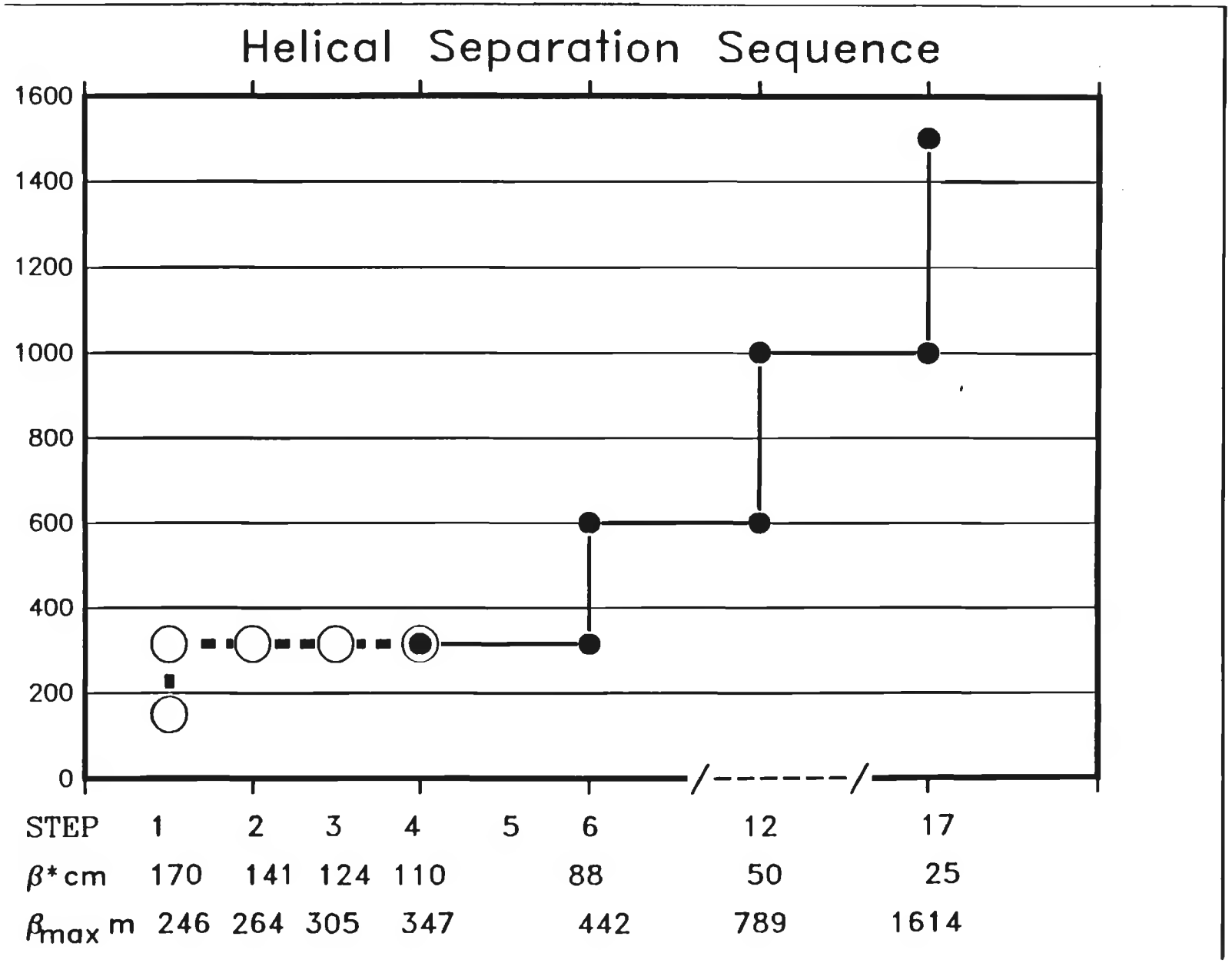
Helical Separation Sequence
1600
1400
1200
1000
800
600
400
200
0
STEP 1 2 3 4 5 6 12 17
β*cm 170 141 124 110 88 50 25
βmax m 246 264 305 347 442 789 1614

Figure 4.6.1

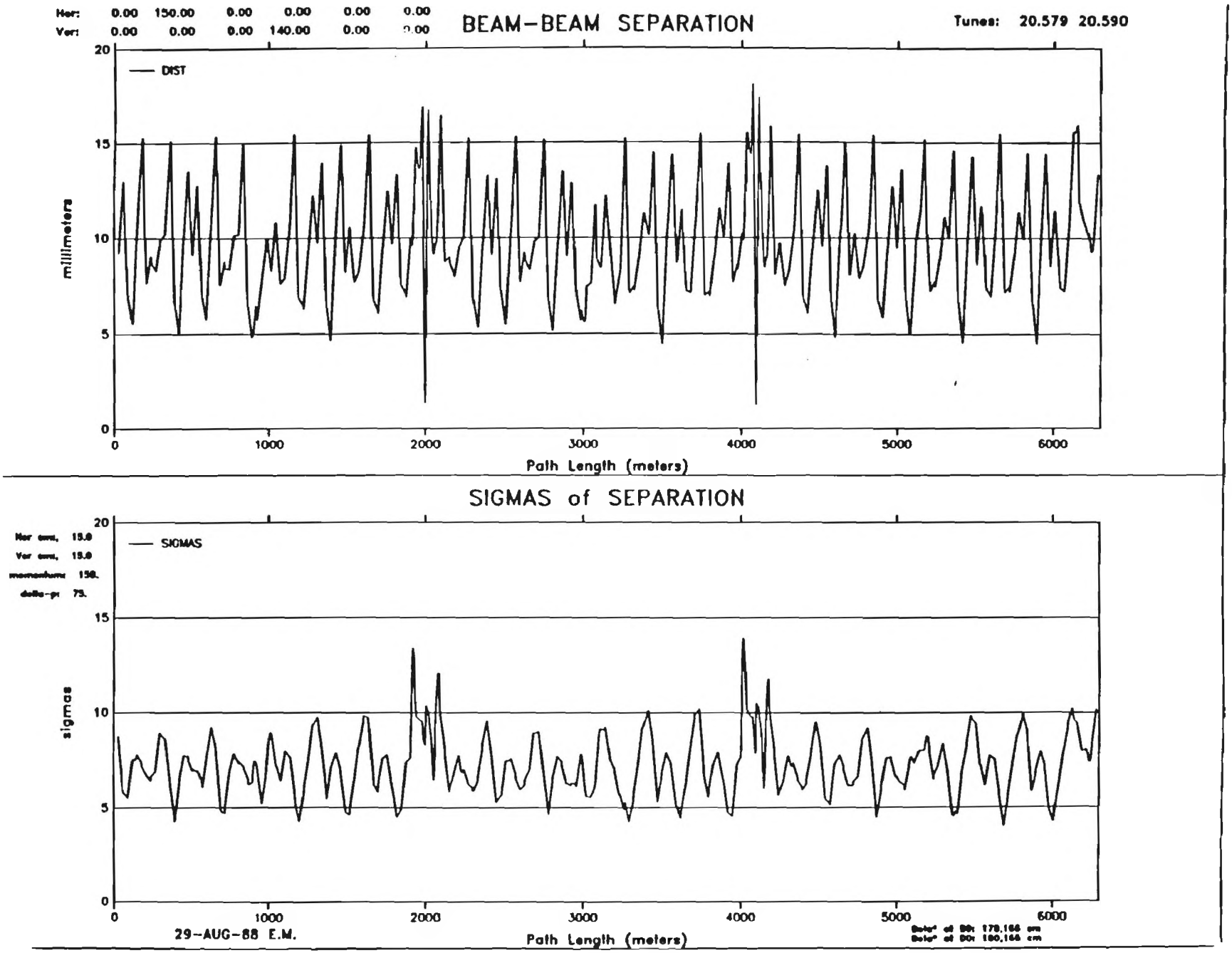
Hor: 0.00 150.00 0.00 0.00 0.00 0.00
Ver: 0.00 0.00 0.00 140.00 0.00 0.00
BEAM-BEAM SEPARATION
Tunes: 20.579 20.590
DIST
millimeters
Path Length (meters)
SIGMAS of SEPARATION
SIGMAS
sigmas
29-AUG-88 E.M.
Path Length (meters)

Figure 4.6.2

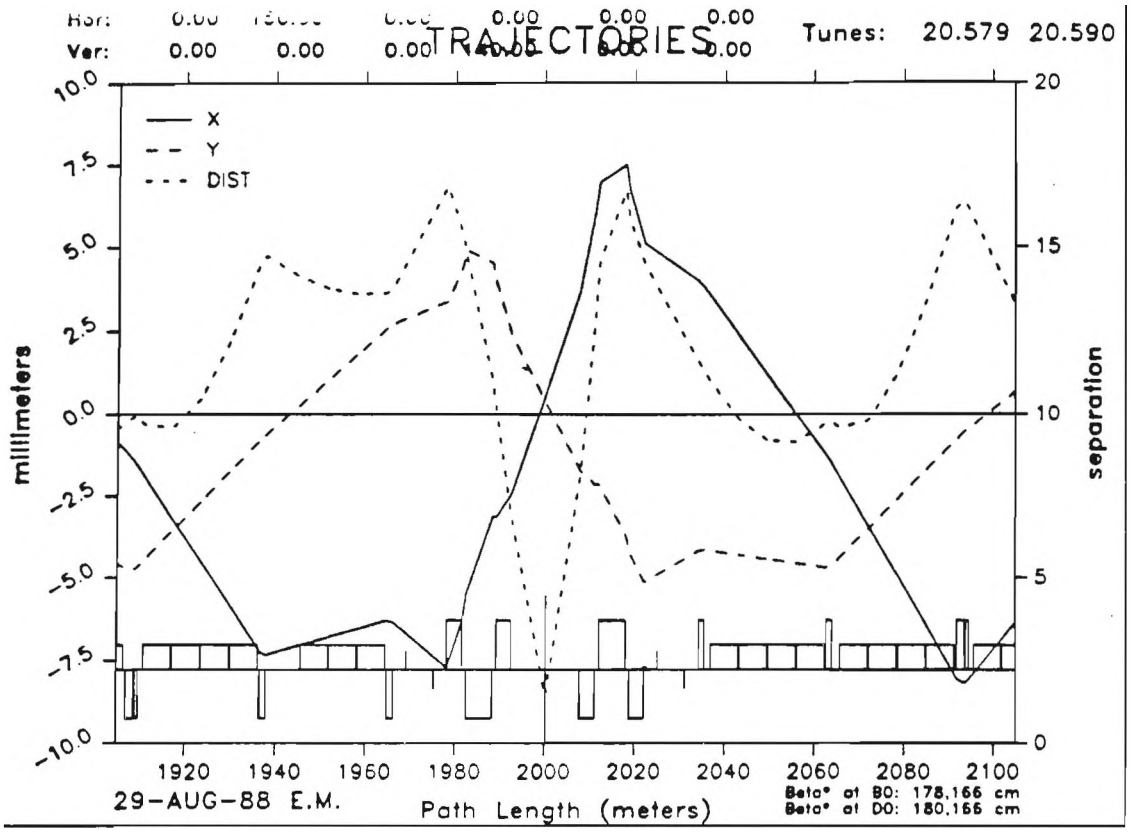

Figure 4.6.3b

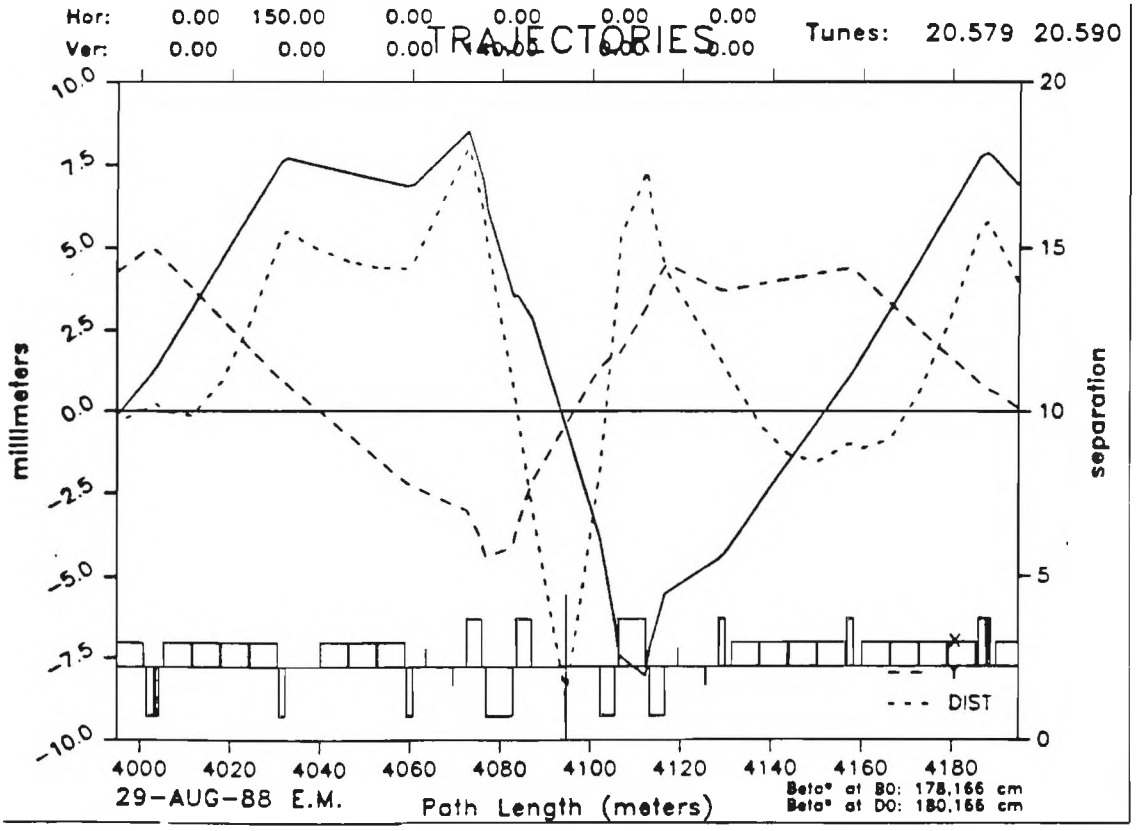

Figure 4.6.3b

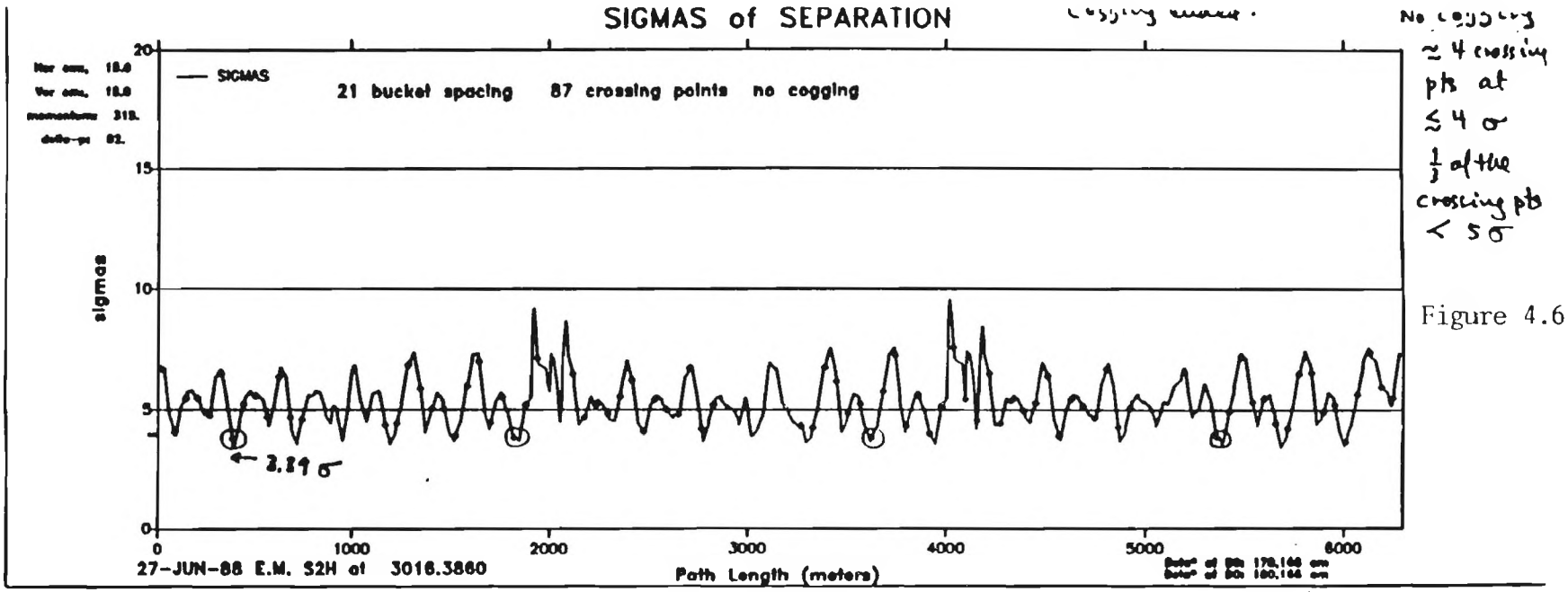

No cogging
≃ 4 crossing pts at ≤ 4 σ
⅓ of the crossing pts < 5 σ

Figure 4.6.4a

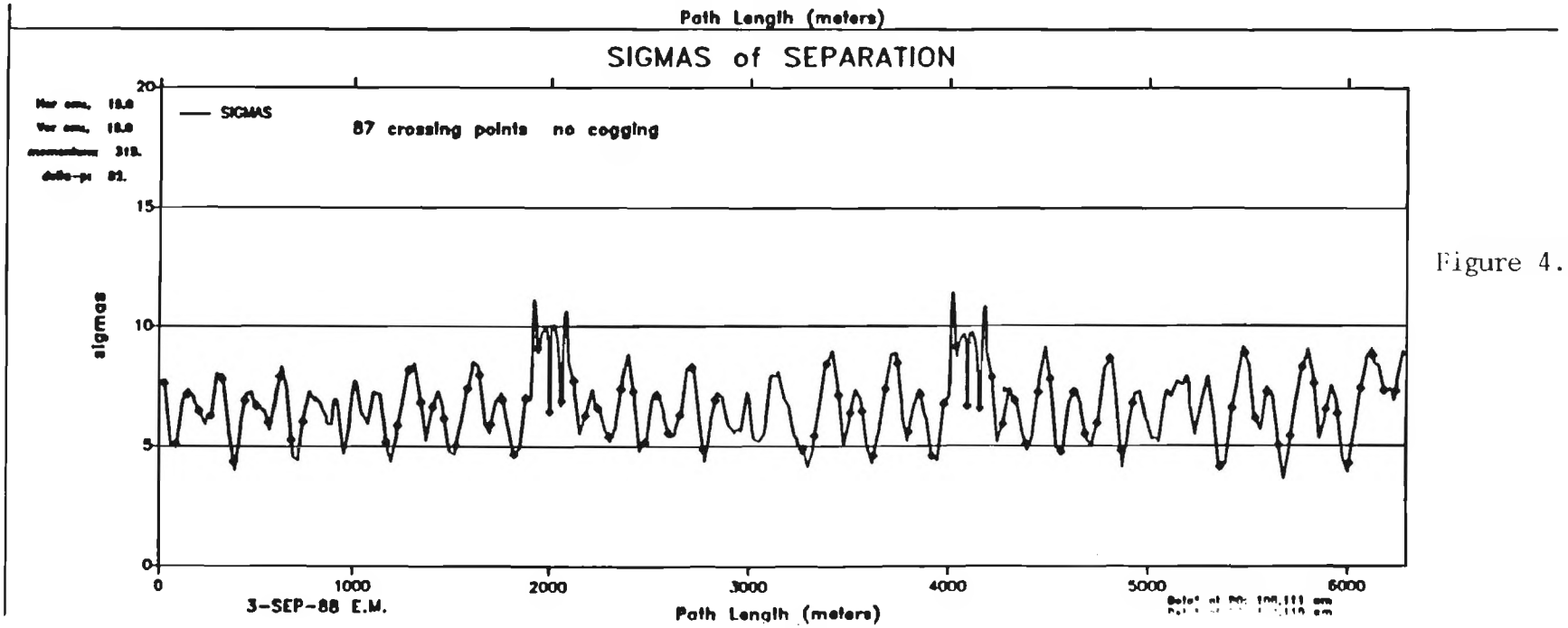

Figure 4.6.4b

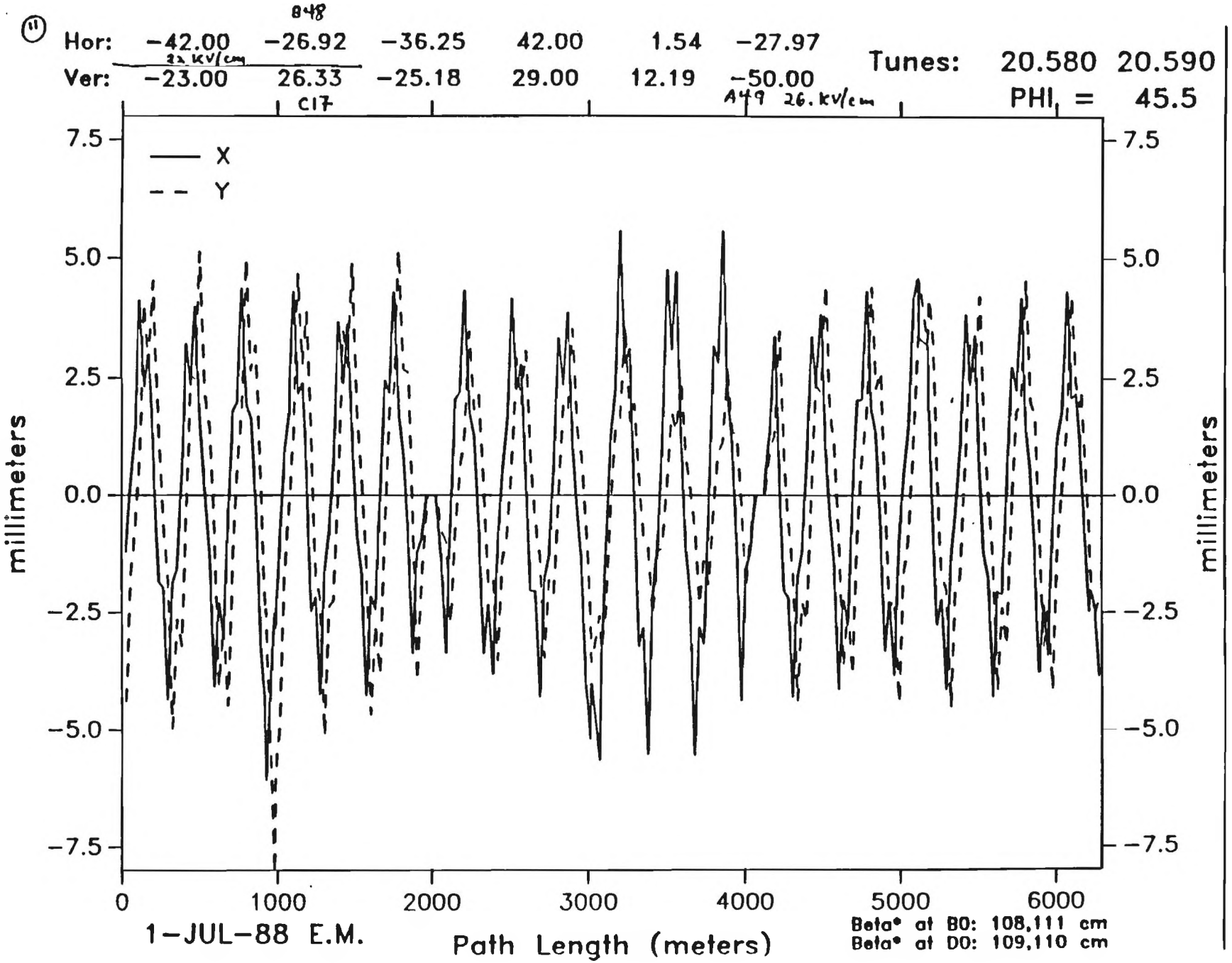
Hor: -42.00 -26.92 -36.25 42.00 1.54 -27.97
Ver: -23.00 26.33 -25.18 29.00 12.19 -50.00
Tunes: 20.580 20.590
PHI = 45.5
X
Y
millimeters
7.5
5.0
2.5
0.0
-2.5
-5.0
-7.5
0
1000
2000
3000
4000
5000
6000
1-JUL-88 E.M.
Path Length (meters)
Beta* at B0: 108.111 cm
Beta* at D0: 109.110 cm

Figure 4.6.5

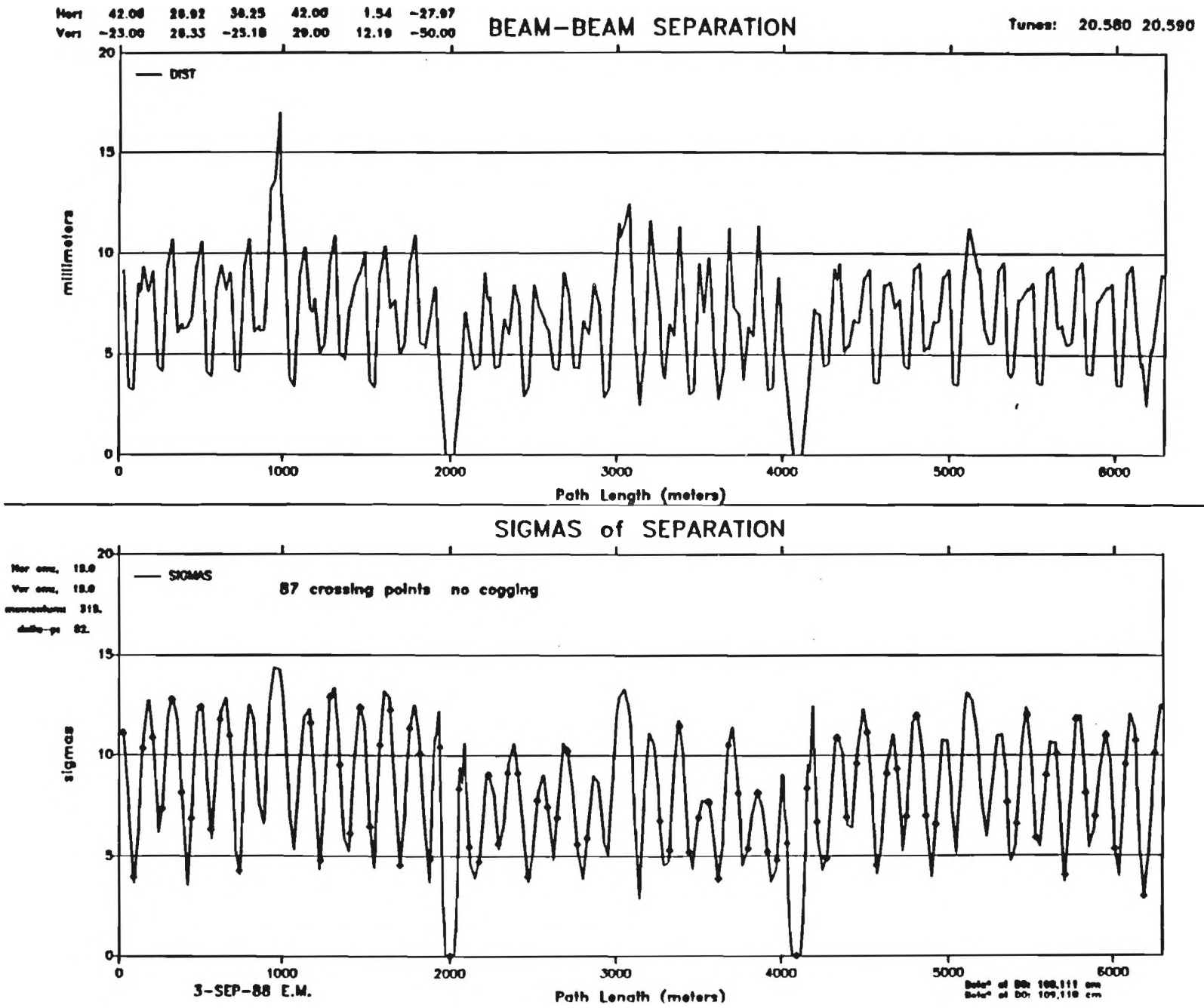
Hori 42.00 28.92 38.25 42.00 1.54 -27.97
Vert -23.00 28.33 -25.18 29.00 12.19 -50.00
BEAM-BEAM SEPARATION
Tunes: 20.580 20.590
DIST
millimeters
Path Length (meters)
SIGMAS of SEPARATION
SIGMAS
87 crossing points no cogging
sigmas
3-SEP-88 E.M.
Path Length (meters)

Figure 4.6.6

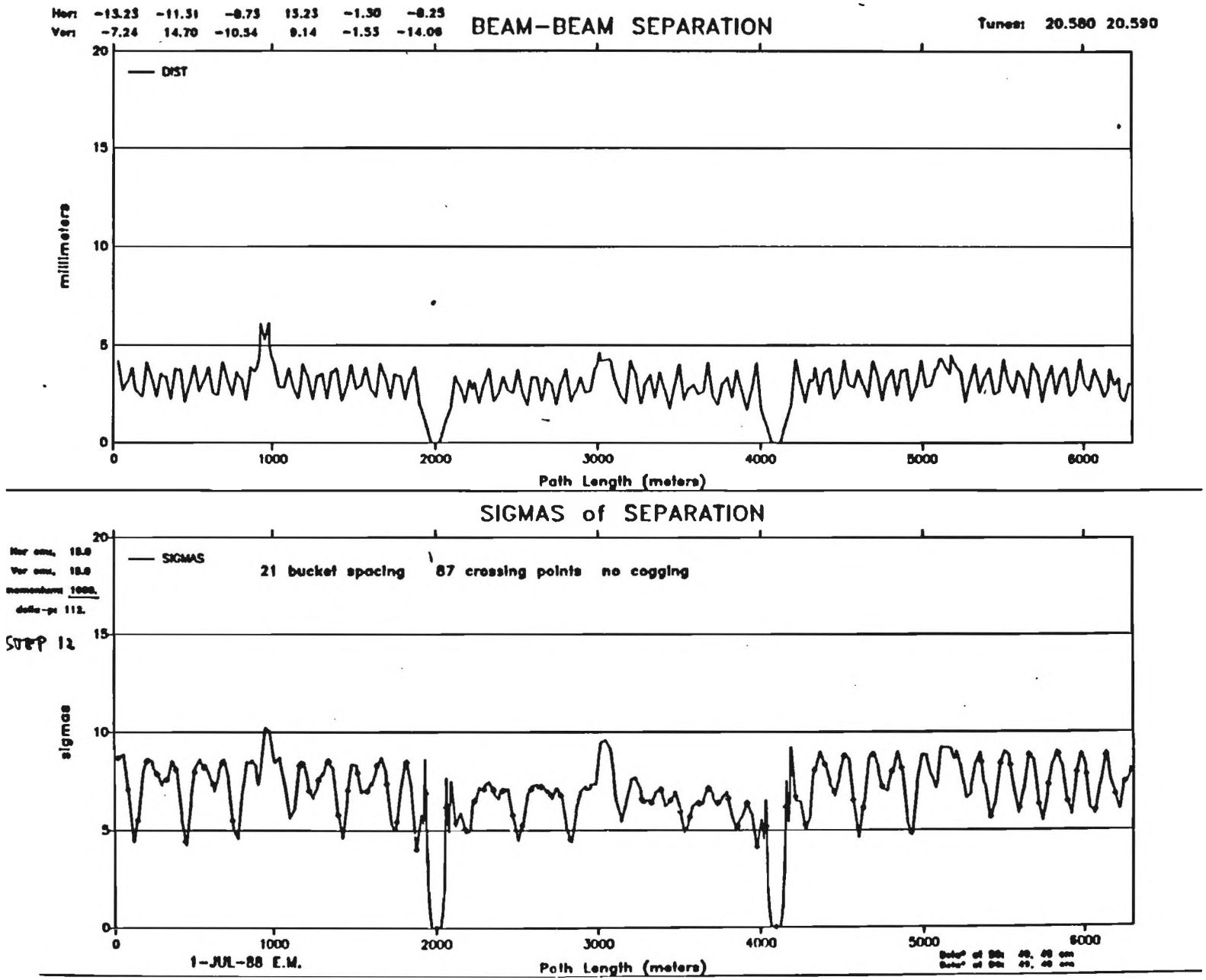
Hor: -13.23 -11.31 -8.73 13.23 -1.30 -8.25
Ver: -7.24 14.70 -10.34 9.14 -1.55 -14.08
BEAM-BEAM SEPARATION
Tunes: 20.580 20.590
DIST
millimeters
Path Length (meters)
SIGMAS of SEPARATION
SIGMAS
21 bucket spacing 87 crossing points no cogging
sigmas
1-JUL-88 E.M.
Path Length (meters)

Figure 4.6.7

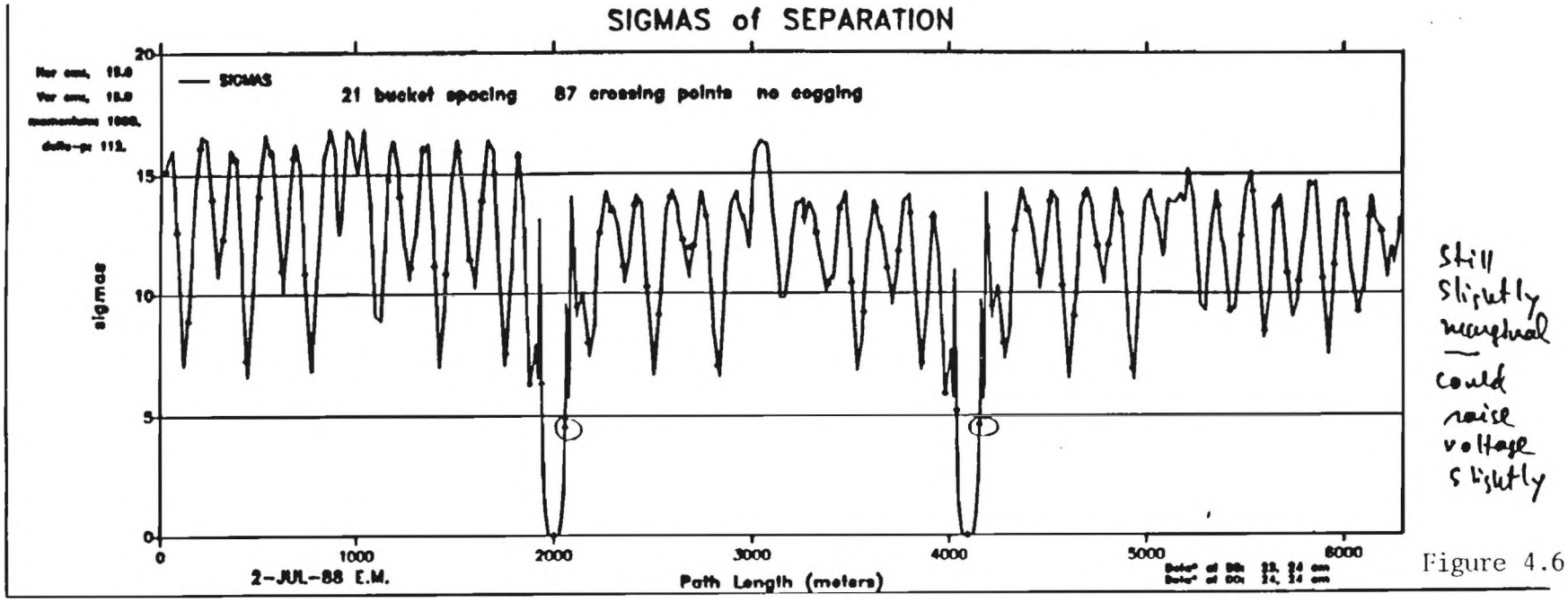

Still slightly marginal — could raise voltage slightly

Figure 4.6.8a

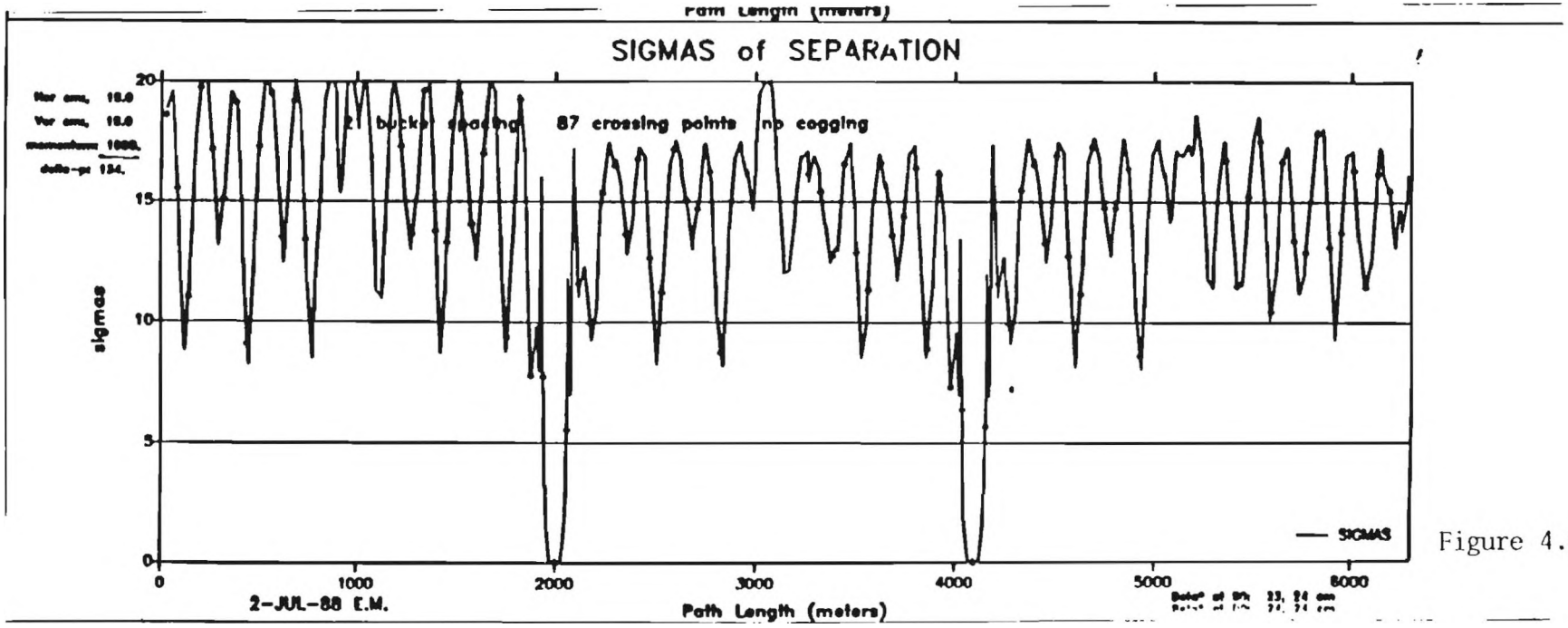

Figure 4.6.8b

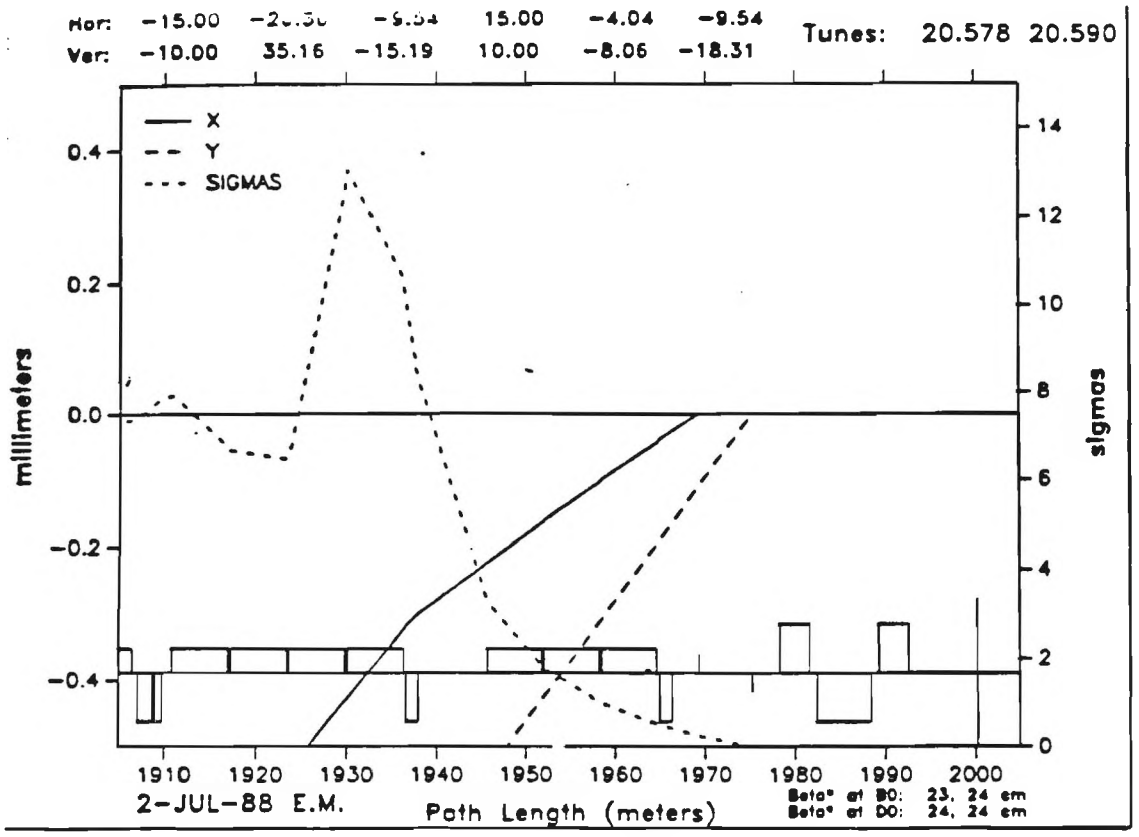

Figure 4.6.9a

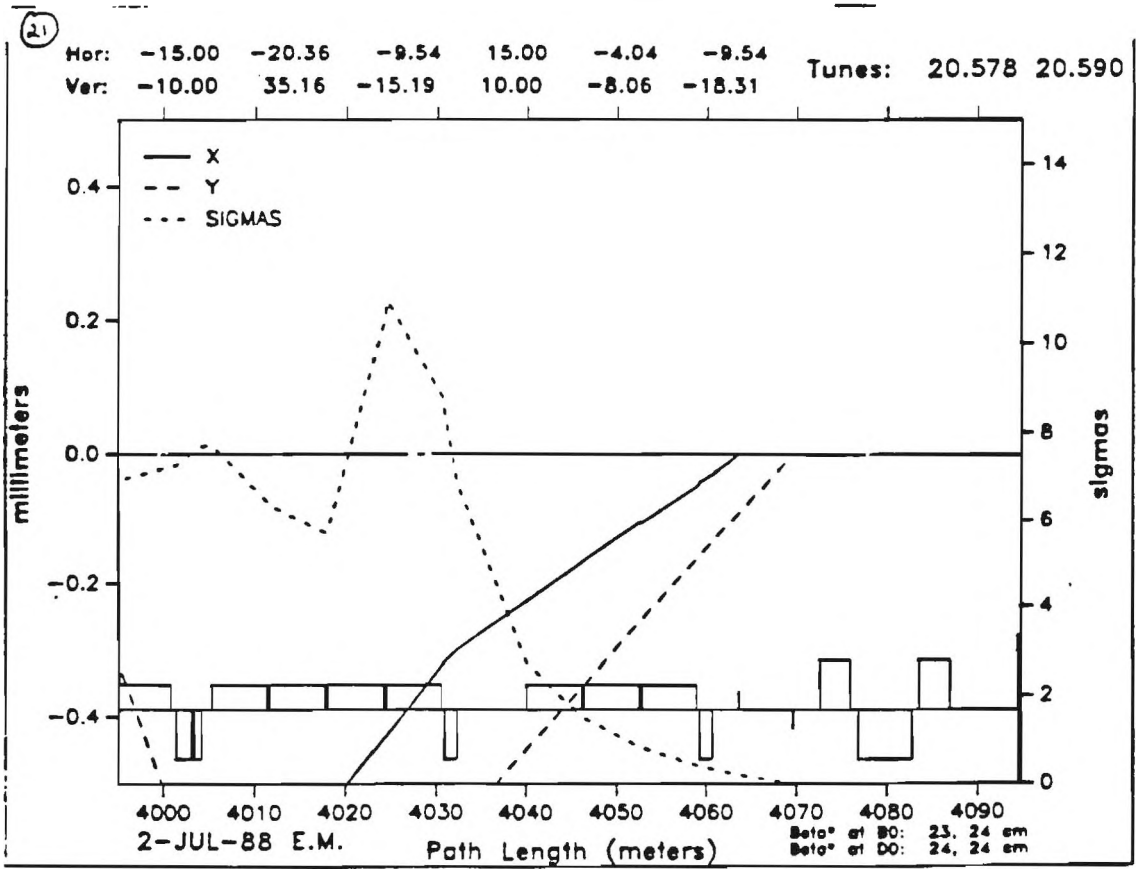

Figure 4.6.9b

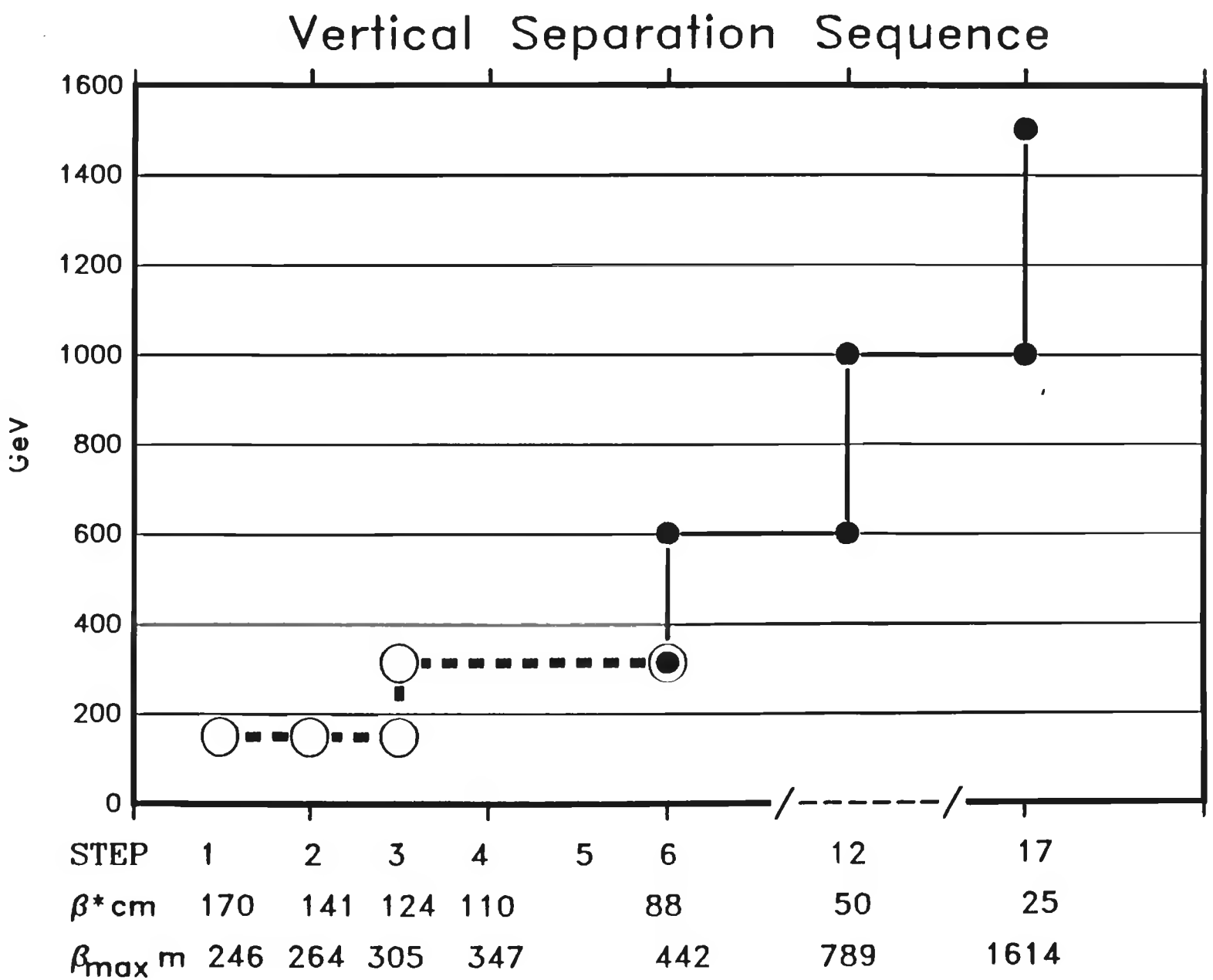
Vertical Separation Sequence
1600
1400
1200
1000
800
600
400
200
0
GeV
STEP 1 2 3 4 5 6 12 17
β*cm 170 141 124 110 88 50 25
βmax m 246 264 305 347 442 789 1614

Figure 4.6.10

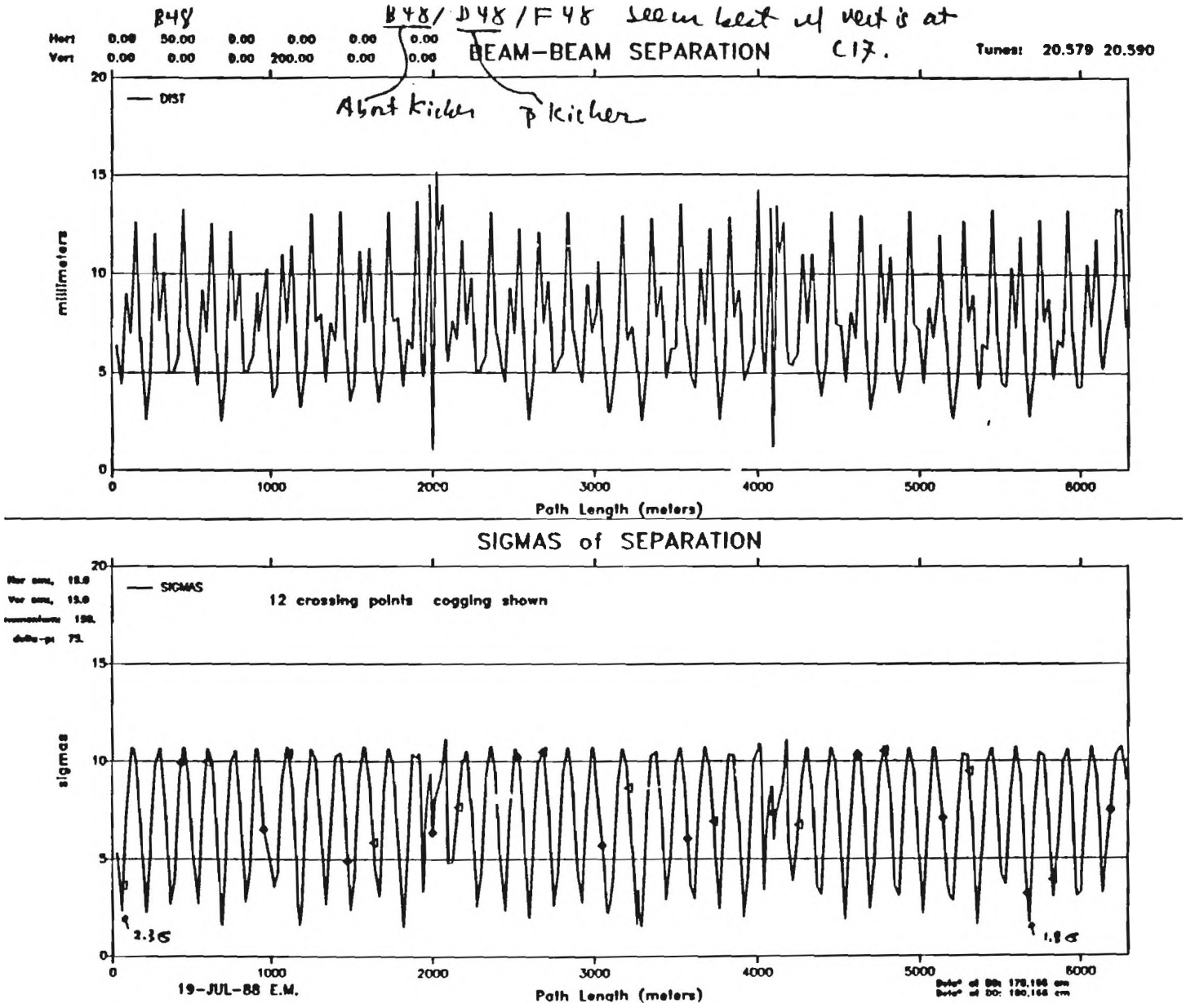
B48
B48/D48/F48 seem best if vert is at
Hori 0.00 50.00 0.00 0.00 0.00 0.00
Vert 0.00 0.00 0.00 200.00 0.00 0.00
BEAM-BEAM SEPARATION C17.
Tunes: 20.579 20.590
— DIST
Abt kicker
p kicker
millimeters
Path Length (meters)
SIGMAS of SEPARATION
— SIGMAS
12 crossing points cogging shown
sigmas
2.3σ
1.8σ
19-JUL-88 E.M.
Path Length (meters)

Figure 4.6.11

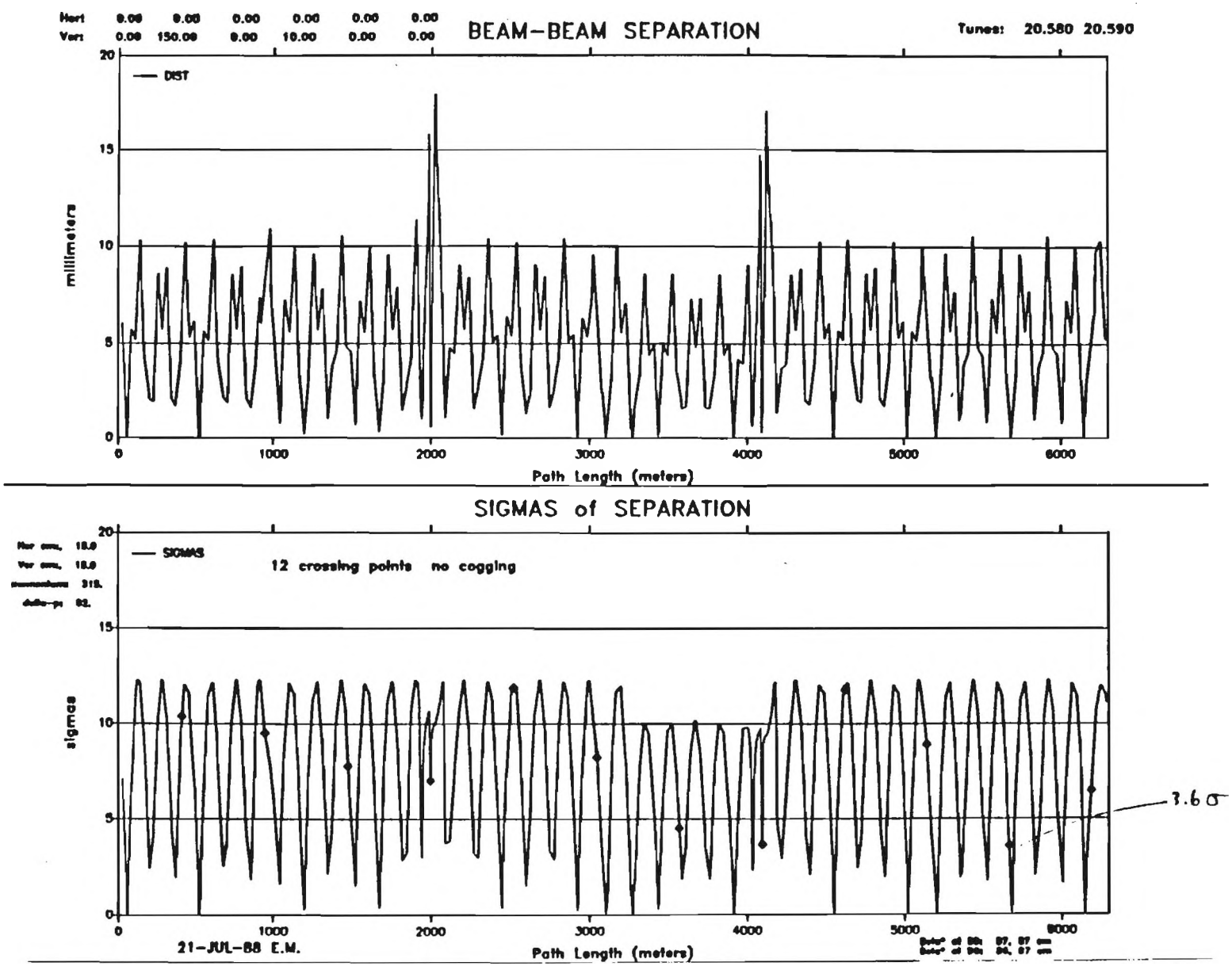
Hori 0.00 0.00 0.00 0.00 0.00 0.00
Vert 0.00 150.00 0.00 10.00 0.00 0.00
BEAM–BEAM SEPARATION
Tunes: 20.580 20.590
DIST
millimeters
Path Length (meters)
SIGMAS of SEPARATION
SIGMAS
12 crossing points no cogging
sigmas
21–JUL–88 E.M.
Path Length (meters)
3.6σ

Figure 4.6.12

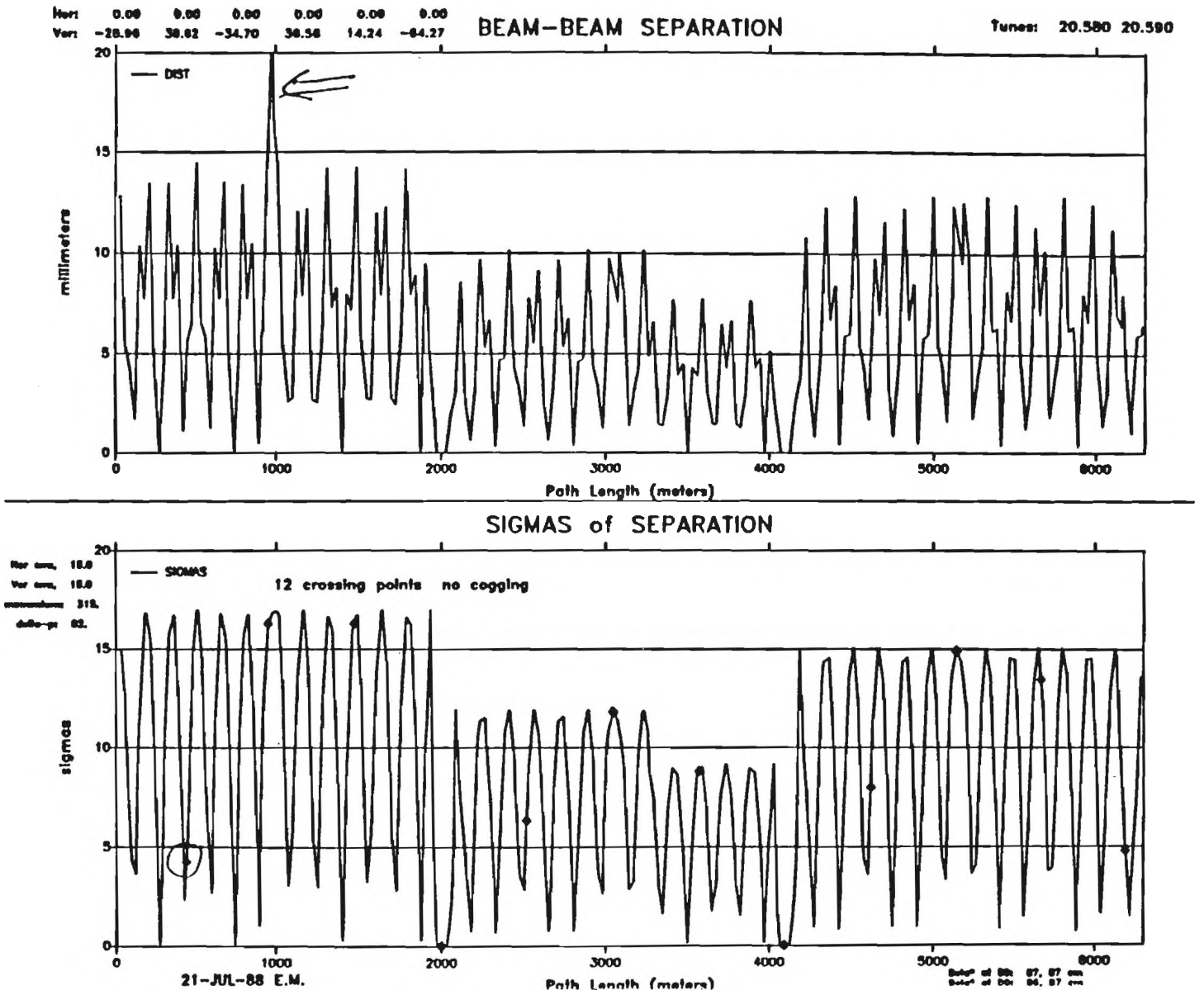
Hor: 0.00 0.00 0.00 0.00 0.00 0.00
Ver: -28.96 38.62 -34.70 38.56 14.24 -84.27
BEAM-BEAM SEPARATION
Tunes: 20.580 20.590
DIST
millimeters
Path Length (meters)
SIGMAS of SEPARATION
SIGMAS
12 crossing points no cogging
sigmas
21-JUL-88 E.M.
Path Length (meters)

Figure 4.6.13

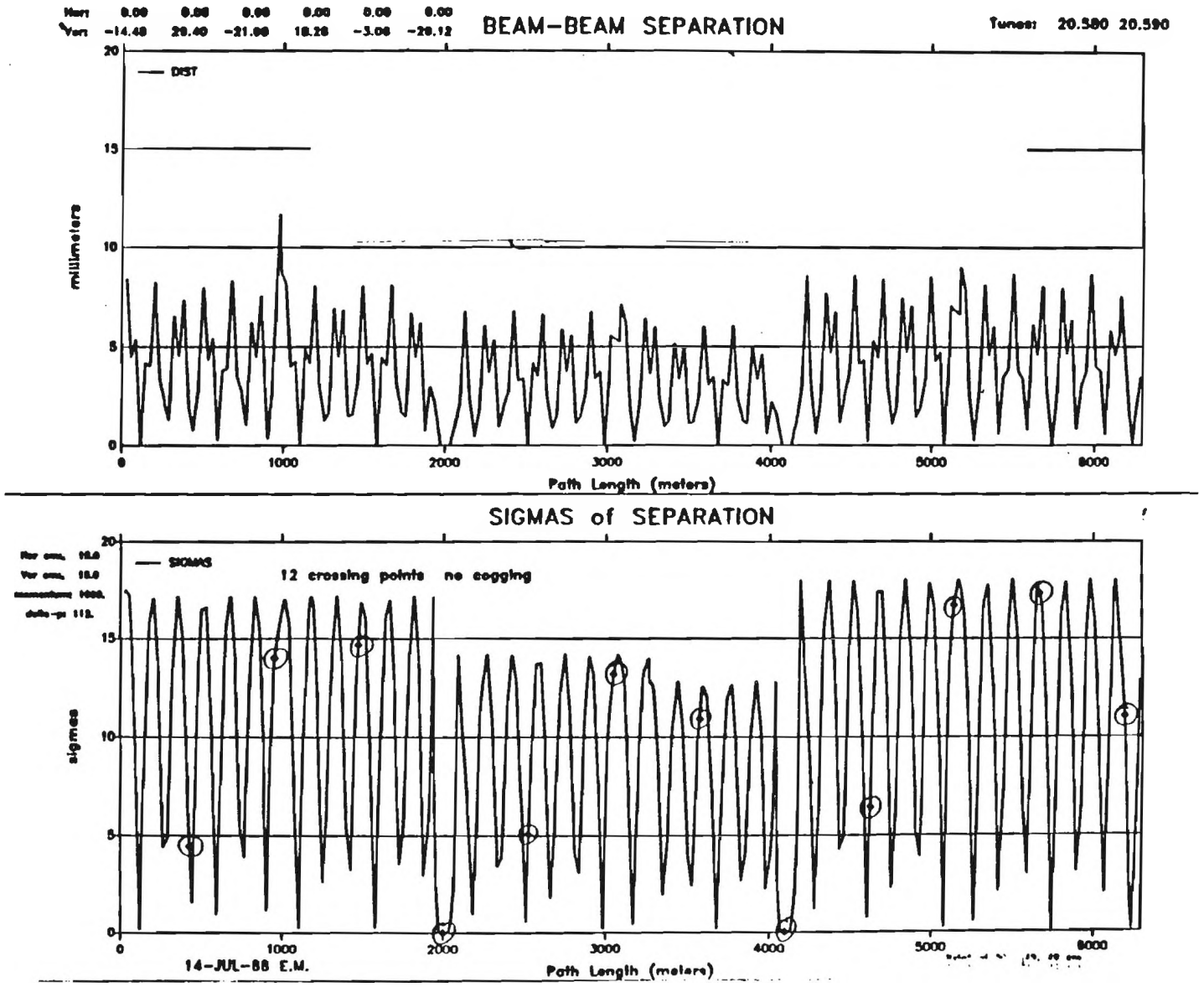
BEAM–BEAM SEPARATION
Tunes: 20.580 20.590
DIST
millimeters
Path Length (meters)
SIGMAS of SEPARATION
SIGMAS
12 crossing points no cogging
sigmas
14-JUL-88 E.M.
Path Length (meters)

Figure 4.6.14

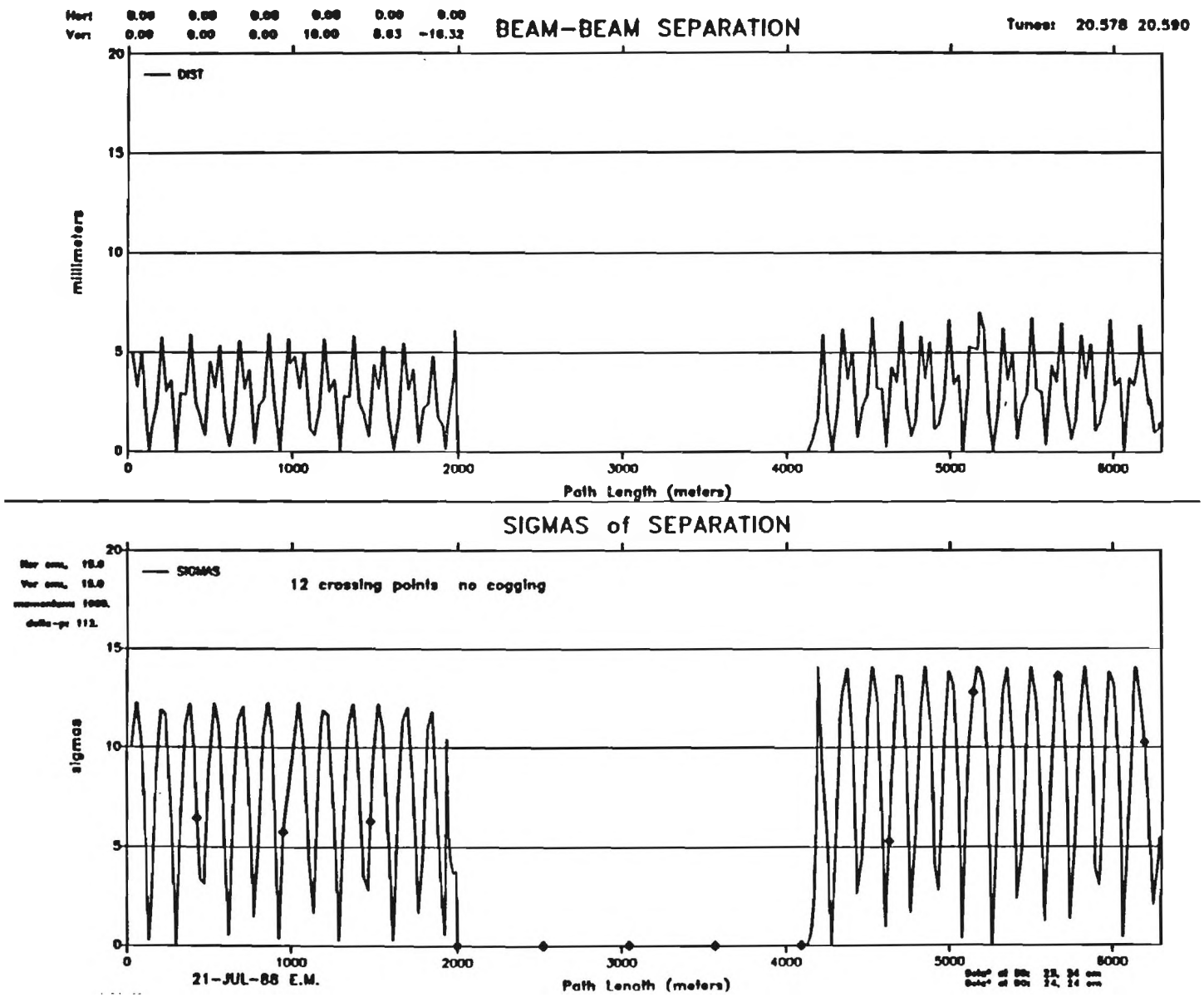
BEAM–BEAM SEPARATION
Tunes: 20.578 20.590
DIST
millimeters
Path Length (meters)
SIGMAS of SEPARATION
SIGMAS
12 crossing points no cogging
sigmas
21-JUL-88 E.M.
Path Length (meters)

Figure 4.6.15

V. TEVATRON INJECTION AND ABORT DESIGN

V.1 BUNCH LOADING SCHEME

Injecting more beam bunches into the Collider is necessary for the upgrade proposal. In order that all the bunches collide at a single detector, the azimuthal proton bunch distribution need only be mirror symmetric to the azimuthal distribution of the counter-rotating antiproton bunches. With two detectors in the Collider, operating simultaneously and located one third of the ring apart at B0 and D0, the two beams need to be azimuthally threefold symmetric as well.

The harmonic number of the Collider and its injector, the Main Ring, is 1113. Threefold symmetry in the Collider requires that its bunch geometry repeats at 371 bucket intervals. The minimum bunch spacing is defined by the Collider separator system which guides the proton and antiproton beams into collision as they enter the detector and again separates their orbits as they leave the detector. The minimum bunch spacing must also be compatable with the production of high intensity bunches by coalescing low intensity ones in the Main Ring prior to injection into the Collider. The Main Ring coalescing harmonic number is h=53 which corresponds to a bunch spacing of 21 buckets.

The maximum number of bunches that fit into the Collider with a bunch spacing of 21 buckets is 53. This number is further reduced by the need for symmetry, injection and abort gaps. A possible 44-on-44 bunch geometry is shown in Figure 5.1.1. The proton and antiproton bunches are grouped in batches of 64 buckets that contain 4 bunches at a 21 bucket spacing. A 122 bucket gap for beam injection and beam abort is obtained by leaving one of the 12 batch locations empty. The gaps between normal batches are 28 or 29 buckets.

It is assumed that all protons are injected into the Collider first. Eleven booster cycles are injected into the Main Ring, accelerated to 150 Gev, coalesced to 44 bunches and injected as one turn into the Collider. Each Booster cycle (h=84) produces one batch containing 4 coalesced bunches. The bunches not accepted by the coalescing procedure of the Main Ring need to be removed in the Main Ring with a suitable damper. The proton injection cycle is similar to fixed target operation of the Tevatron and modification of existing proton beam transfer kickers is not required.

The 11 antiproton batches are injected into the missing proton batch gap of the Collider one batch at a time. After an antiproton batch has been injected into the Collider, the antiproton bunches in the Collider have to be

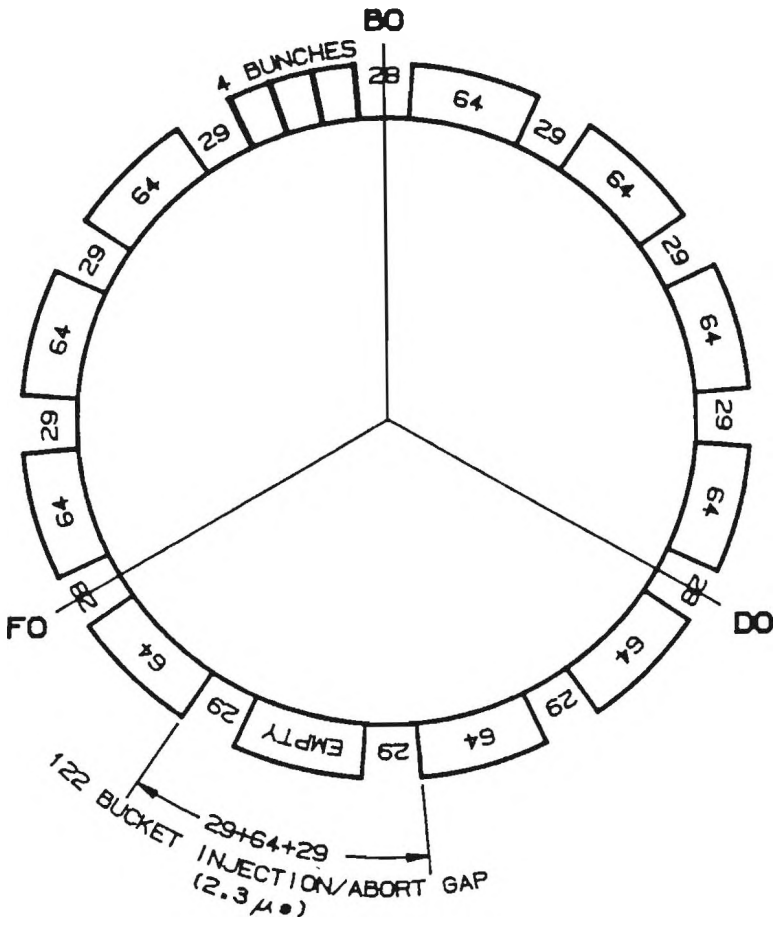

Figure 5.1.1 44 bunch injection pattern

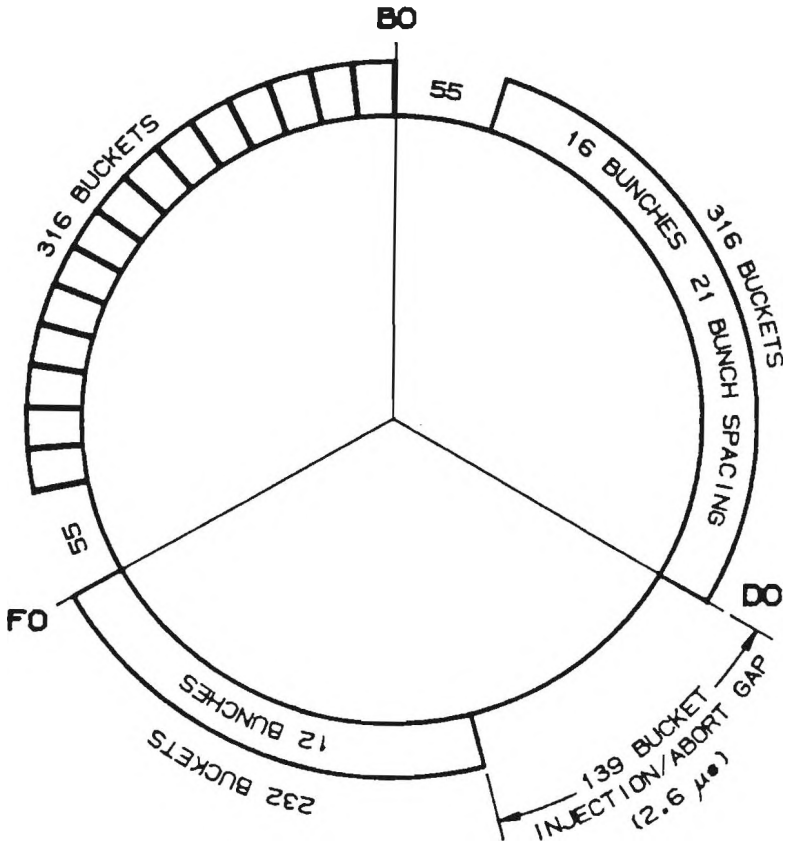

Figure 5.1.2 Alternate 44 bunch injection pattern.

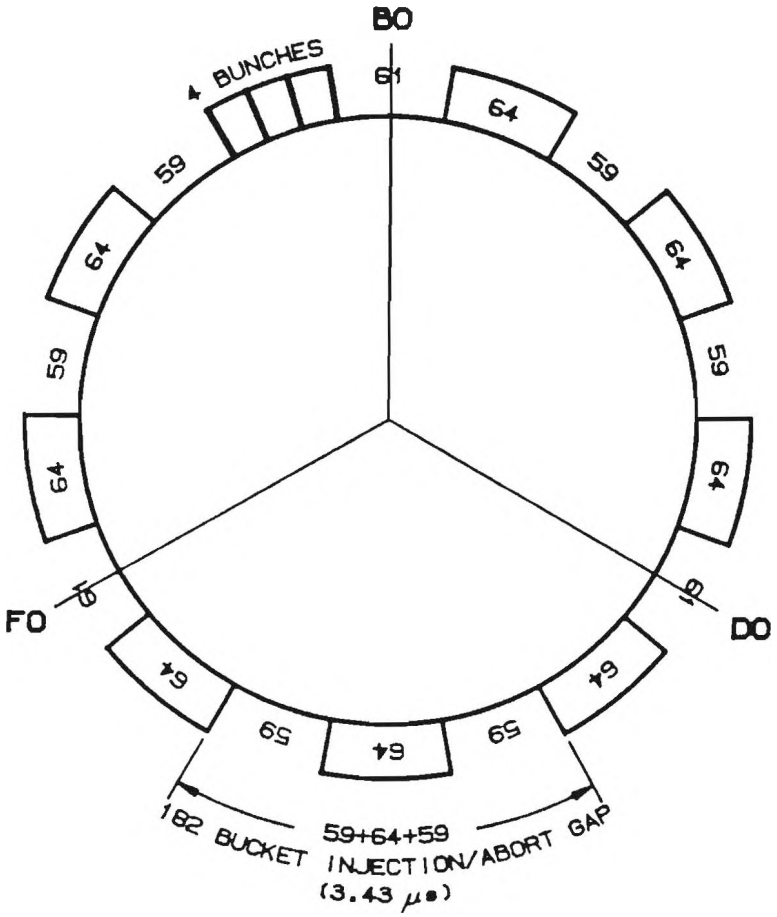

Figure 5.1.3 32 bunch injection pattern.

cogged 92 or 93 buckets to clear the injection gap for the next antiproton transfer.

At present, the Accumulator unstacks one bunch of antiprotons at a time with an h=2 rf system with one bucket suppressed. This bunch is injected into the Main Ring and the unstacking process is repeated. The adoption of an h=4 unstacking system in the Accumulator would produce 4 antiproton bunches for injection into the Main ring and reduces the time required to fill the Collider with antiprotons.

The required Collider antiproton injection kicker rise and fall time for the geometry depicted in Figure 5.1.1 is 0.53 μs (28 buckets). In general, the rise and fall times of the antiproton injection kicker need not be equal. Figure 5.1.2 shows a modified 44-on-44 distribution. This example requires the antiproton injection kicker to rise within 20 buckets (0.38 μs) and fall within 55 buckets (1.0 μs).

A lower luminosity can be obtained by reducing the number of batches injected into the Collider. An example of a 32-on-32 bunch Collider geometry is shown in Figure 5.1.3. The 4 bunch, 64 bucket batches are retained and 8 proton and antiproton batches are injected into the Collider. This increases the batch spacing to 59 or 61 buckets and the antiproton injection gap to 182 buckets. The corresponding antiproton injection kicker rise and fall times are 59 buckets (1.1 μs).

V.2 INJECTION FROM THE MAIN RING TO THE TEVATRON

In the presence of separated orbits the primary question relating to the injection process is whether or not the extra aperture demands resulting from the displacement of the two beams can be accomodated. The critcal aperture during this process is at the antiproton injection magnetic septum.

The proton and antiproton transfers from Main Ring to Tevatron will be accomplished in the following way. Protons are injected into the Tevatron with separators turned off along the same closed orbit as that currently used. The proton injection Lambertsons are retracted eliminating possible aperture restrictions at his location. The separators are then turned on and antiprotons are injected onto the new closed orbit. Figure 5.2.1 shows the difference between the closed orbit before and after separators are energised. To accomplish this both proton and antiproton bunches must fit inside the reverse injection Lambertson notch.

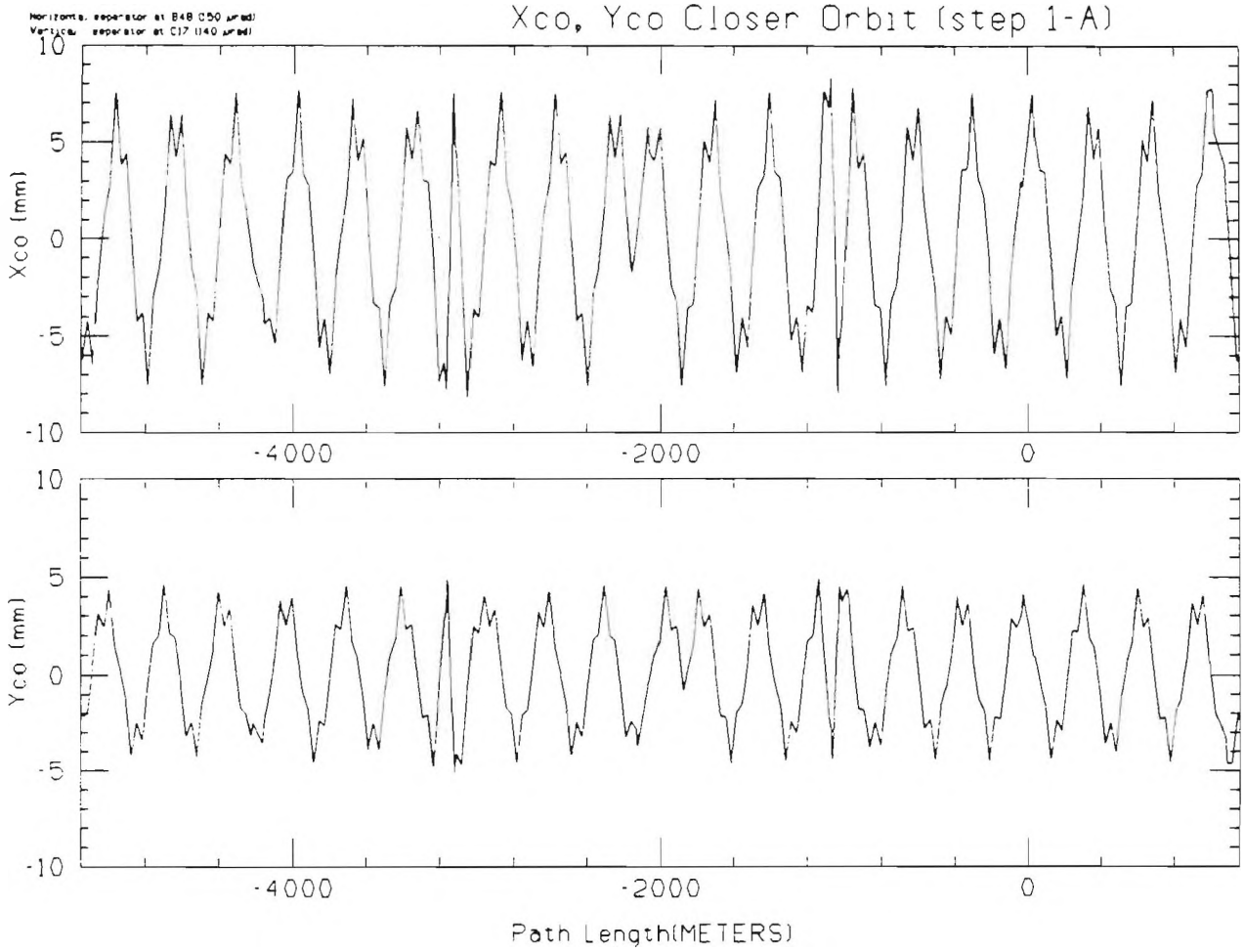
Xco, Yco Closer Orbit (step 1-A)
Xco (mm)
Yco (mm)
10
5
0
-5
-10
-4000
-2000
0
Path Length(METERS)

Figure 5.2.1

Figure 5.2.2 shows the results of an aperture scan done on the reverse injection Lambertson notch. The solid and dashed lines are the 50% and 10% apertures, respectively. That is a beam (transverse emittance 12 π mm-mrad) whose centroid lies on the solid or dashed line will lose 50% or 10% of it's initial intensity. Figure 5.2.3 is the projection of the beam position measured at the vertical and horizontal BPM's at D49 onto the reverse injection Lambertson plane. The dashed line in figure 5.2.3 is the projected 10% aperture of the upstream Lambertson and the dotted line is the projected 10% aperture of the downstream one. The Lambertson notch is 90 degrees and the downstream Lambertson has a 15 degree roll relative to the upstream Lambertson. The roll angle is designed to be approximately 7 degrees and the discrepency between measurement and design is interpreted as measurement error arising from the digitizing accuracy of the BPM system. However, even with this measured reduction in aperture figure 5.2.2 indicates that the proton beam centroid is approximately 2 sigma from the 10% aperture and the antiproton beam centroid is more than 4 sigma. Thus the present closed orbit in the Tevatron is probably acceptable with the proton beam presenting the possible problem.

However, if necessary the protons could be moved further from the aperture of the downstream Lambertson in three different ways. First an additional separator can be turned on to change the relative phase of the vertical and horizontal betatron oscillations (see figure 5.2.1). Thus rotating the proton centroid away from the aperture. A change in phase equivalent to a 1 sigma motion of the protons away from the aperture would reduce the average beam separation by only ~5%. It is also possible that the position of the closed orbit could be moved out horizontally thus moving both the antiprotons and the protons away from the magnet without any loss in beam separation. There is a limit to the amount the beam can be moved horizontally and still be kicked onto the closed orbit by the D48 kicker. This possibility has not been fully explored but if the antiproton bunch is positioned in the notch such that it's horizontal position is at the same point as the present closed orbit the protons would be 2.5 sigma away from the 10% aperture. Also the horizontal position of the Lambertsons may not be optimized and it may be possible to move the septum position out by 5 mm, this would place the protons aproximately 4 sigma from the 10% aperture.

In conclusion, the reverse injection lambertson aperture is large enough to contain both proton and antiproton beams with neglegible beam loss. If additional aperture is required there are three options which can move the beams away from the aperture restriction

V.3 ANTIPROTON AND PROTON ABORT SYSTEMS

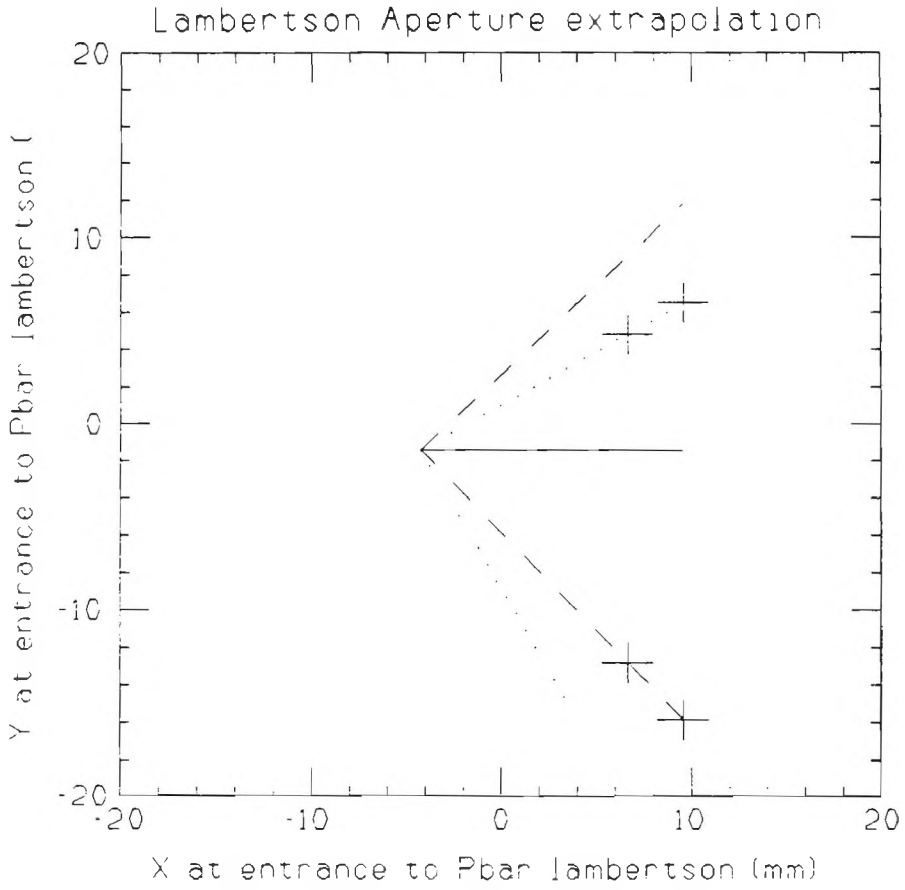
Lambertson Aperture extrapolation
Y at entrance to Pbar lambertson (
X at entrance to Pbar lambertson (mm)
20
10
0
-10
-20
-20
-10
0
10
20

Figure 5.2.2

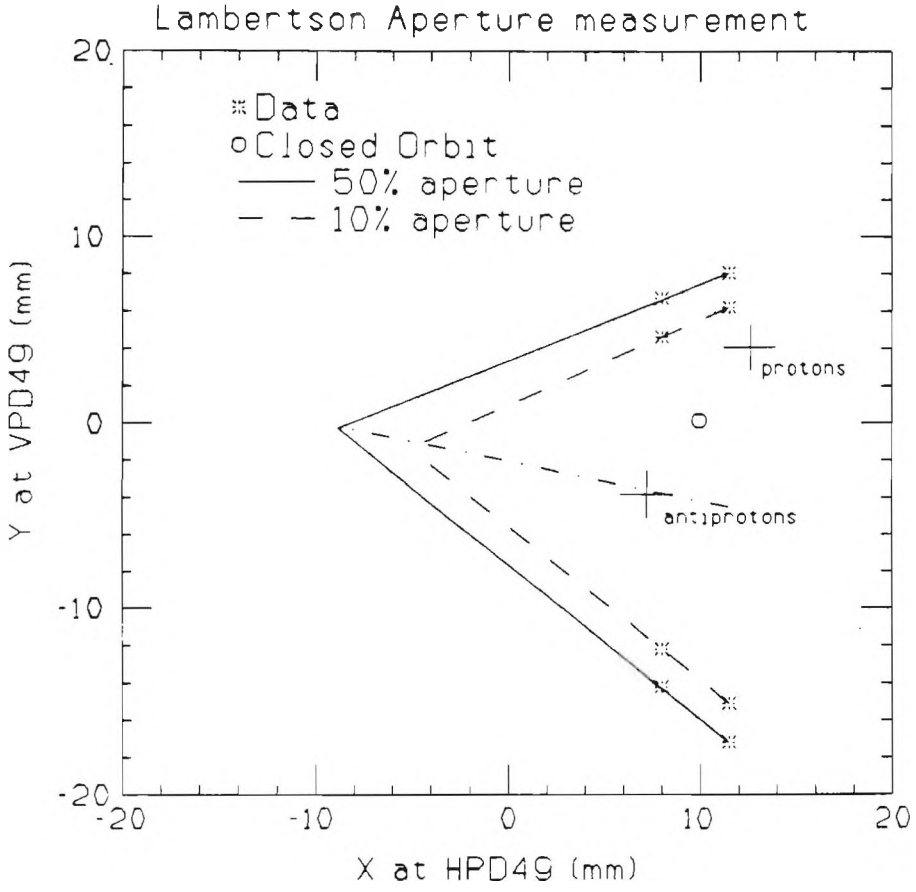
Lambertson Aperture measurement
Data
Closed Orbit
50% aperture
10% aperture
protons
antiprotons
Y at VPD49 (mm)
X at HPD49 (mm)
20
10
0
-10
-20
-20
-10
0
10
20

Figure 5.2.3

The design of the orbit separation system utilises space in the Tevatron lattice for the electrostatic plates that is presently used by the proton and antiproton abort kickers. In order to make this space available another location for the abort system must be found. In this section we present a compact design for the abort system where the elements (kickers and dump) reside completely within the existing straight section freeing up the warm sections in the arcs (the 48 and 17 locations).

The layout of the abort region is shown schematically in fig. 5.3.1. The beam dump is located in the center of the straight section and is bi-directional. Two sets of kicker magnets located at each end of the straight section deflect both the proton and antiproton beams vertically onto the dump. Each set of kicker magnets consists of 5 modules of the type presently used in the proton abort system. The magnets, each of length 2m, result in a total downward beam deflection of 1.3 mrad. The dump is ~10m long and the resulting drift length gives a beam displacement of 20mm at the dump location. The kicker magnet field is 4.6 KG which corresponds to a current pulse in the magnets of 23 KA, similar to the present operational conditions.

For a given circulating beam current, the more intense the transverse phase-space density the greater the instanteous temperature rise inside the dump. Since the dump lies within the machine lattice there is no possibility of blowing up the beam spot at the dump as is customary when using external abort lines. The lattice functions at the abort dump location and the upgrade beam parameters result in a spot size of 0.77 x 0.32 mm (H and V) rms at 1 Tev.

In order to estimate abort beam intensities we have assumed a single high energy full-intensity abort of 2×10^{12} particles can occur once per hour, and low energy injection aborts of this intensity can occur once every 120s for a period of four hours per day. Power dissipation and residual activation levels can be scaled to different operating scenarios from these numbers

Design Criteria

Taking into account the dump materials and optimizing the overall scheme, we require the following criteria to be fulfilled:

1 For a single abort the maximum energy deposition in any region of the dump system and corresponding temperature rise must be less than the melting points and the shock wave limits for the given materials[1].

2 The cooling system should provide the necessary heat transfer from the core to prepare the dump for the next abort.

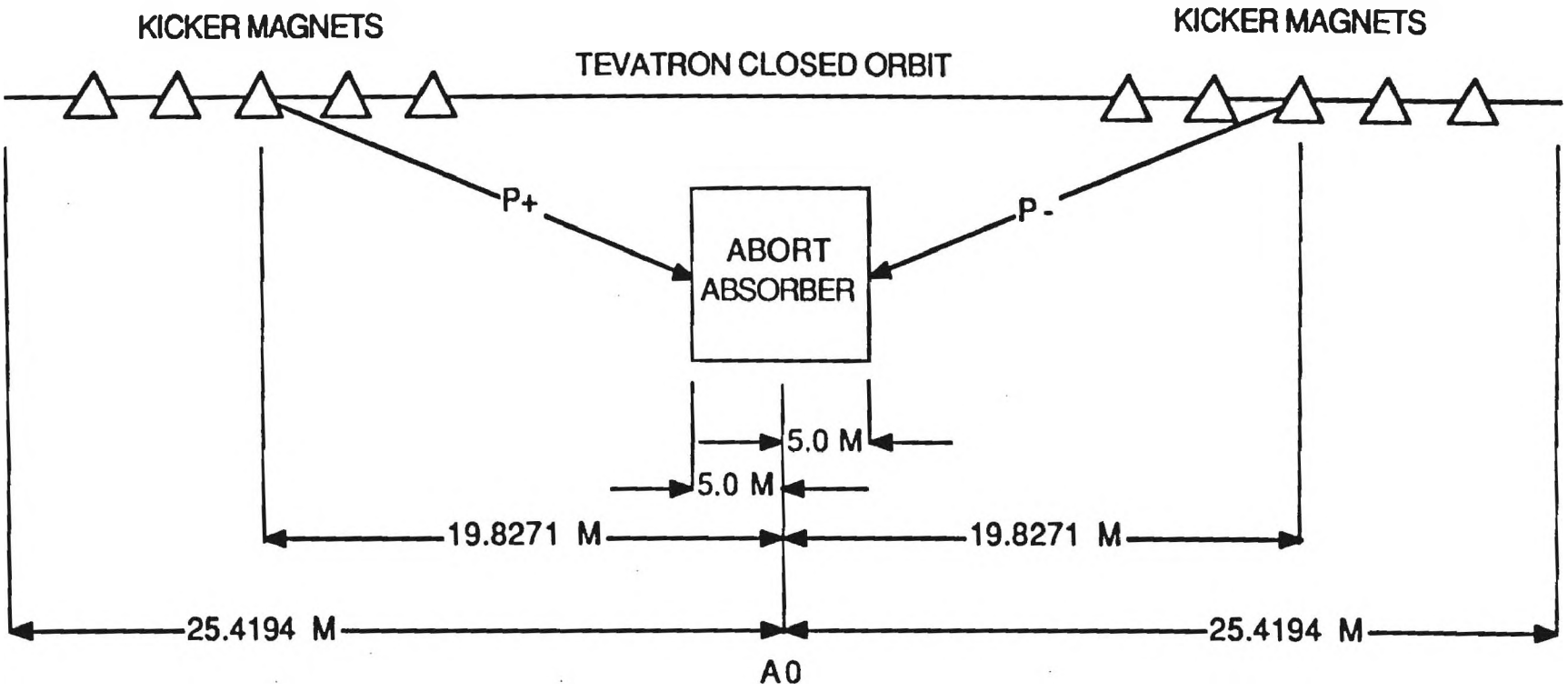

FLANGE TO FLANGE LENGTH OF EACH MAGNET IS 2.2369 METERS

Figure 5.3.1 Tevatron Upgrade Abort Layout

3 The energy deposition in the superconducting quadrupoles immediately downstream of the straight section must be well below the quench limit[2].

4 The induced radioactivity levels near the dumps should be within acceptable limits[3,4].

5 Ground water activation around the abort region by hadron fluxes escaping the dump must be prevented.

6 The lifetime of the dump should exceed a few years at least.

Energy deposition and temperature rise

The cross-section design of the abort dump is shown in fig. 5.3.2, and consists of graphite absorber surrounded by a closed loop water cooling system in an aluminium box. This box is then surrounded by a steel shield. The graphite core consists of 13.5 x 9.0 x 2.0 cm slabs in an argon atmosphere. Figure 5.3.3 shows the two dimensional energy deposition density distribution in the graphite absorber. The results demonstrate the familiar hadronic cascade properties: the very sharp radial fall off and the relatively slow longtitudinal dependence. The instananeous temperature rise can be determined from this data and the enthalpy reserve[5]. The results with the core at an initial temperture of 27C for the 1 Tev abort of 2 x 10^{12} are shown in fig. 5.3.4. The maximum temperature of ~300C is reached on the beam axis at a longtitudinal distance of 140 cm. Experience with the existing beam dump indicates that if the graphite is contained in an inert (argon) atmosphere then lifetime effects at this temperture rise are not a problem. The temperture rise at radii > 3.5 cm is ~ 25C and in the steel central portion is 50C.

Coolins system

The cooling system parameters follow directly from the assumed abort scenario. The total power deposited into the dump during a 1 Tev abort of 2 x 10^{12} is ~260 KJ, the 150 Gev case gives 43 KJ. With 30 low energy and one high energy aborts per hour then the total power is 1550 KJ/hr per beam or ~0.86 KW total, a relatively modest requirement of heat transfer to the cooling system.

Quenching

The primary cause of heating in the downstream superconducting elements is low energy secondary particles scattering back out of the edge of the graphite absorber[6]. The beam displacement and incident angle ensure

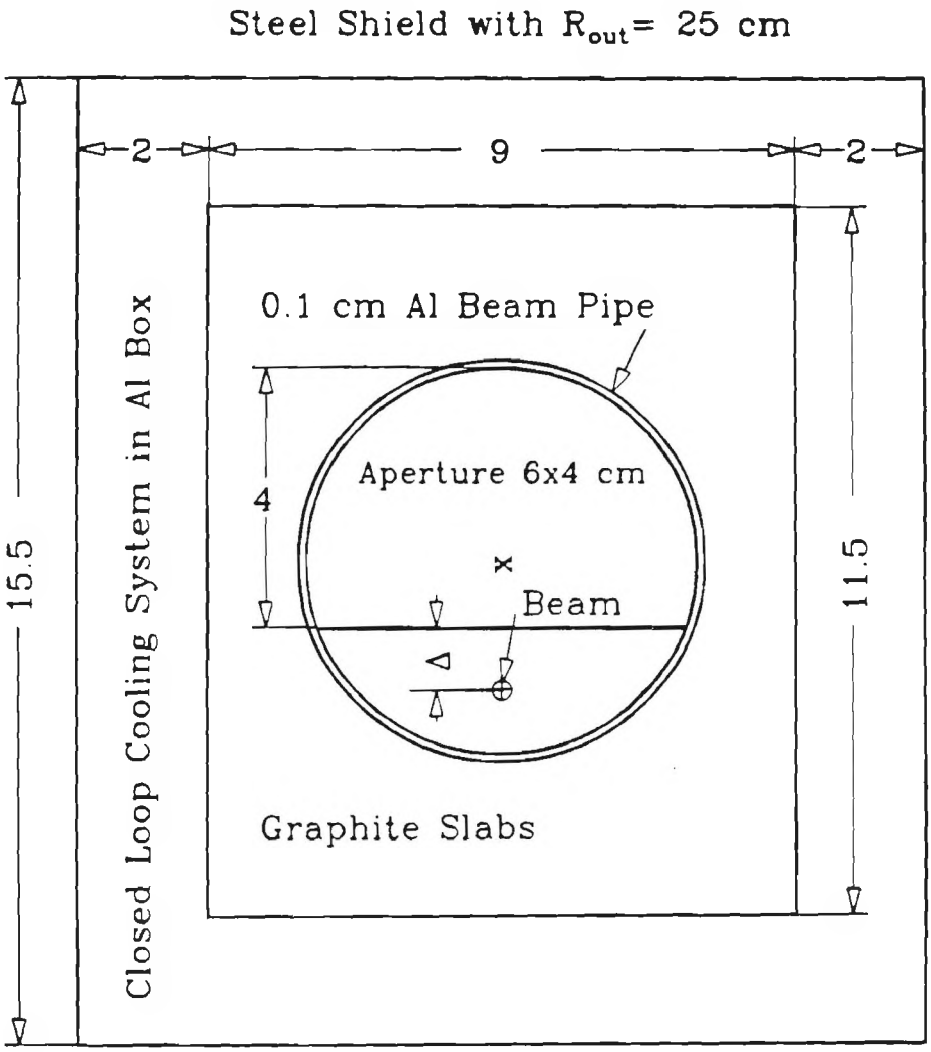

Figure 5.3.2 Core of the internal beam abort dump. Scheme 1(A). All dimensions are in cm.

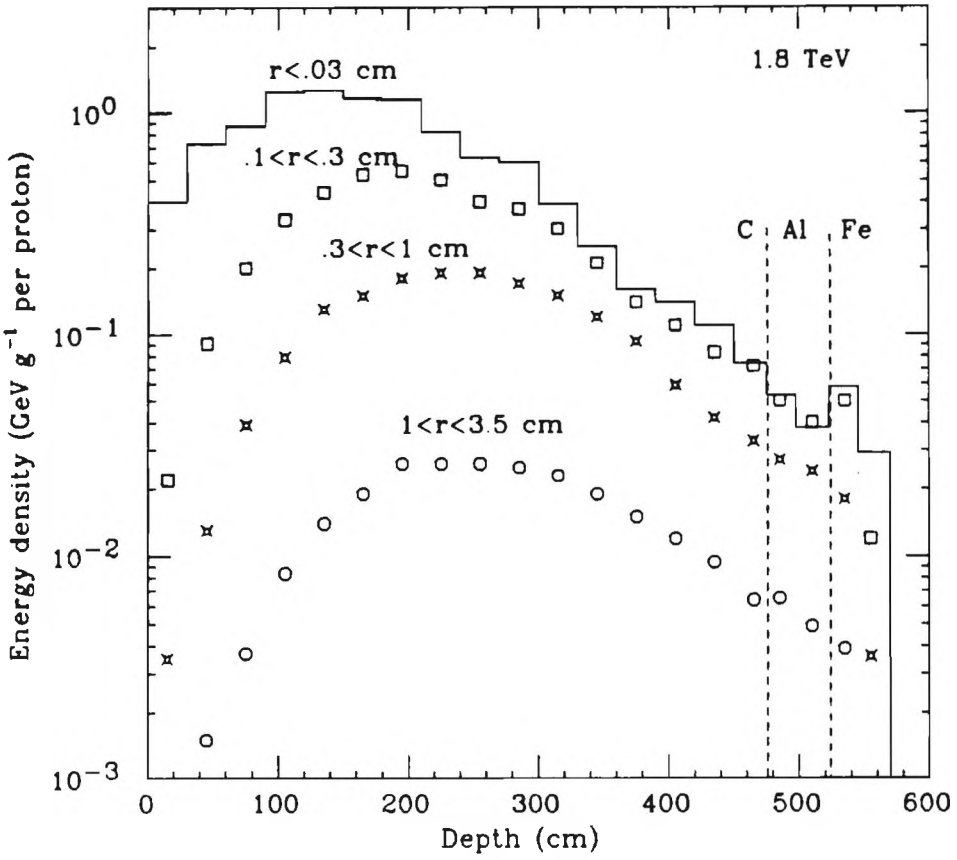

Figure 5.3.3 Longitudinal distributions of energy deposition density in the various radial bins of the core of the internal beam dump at the 1.8 TeV proton abort with a beam spot of 0.48*0.34mm (H*V) rms.

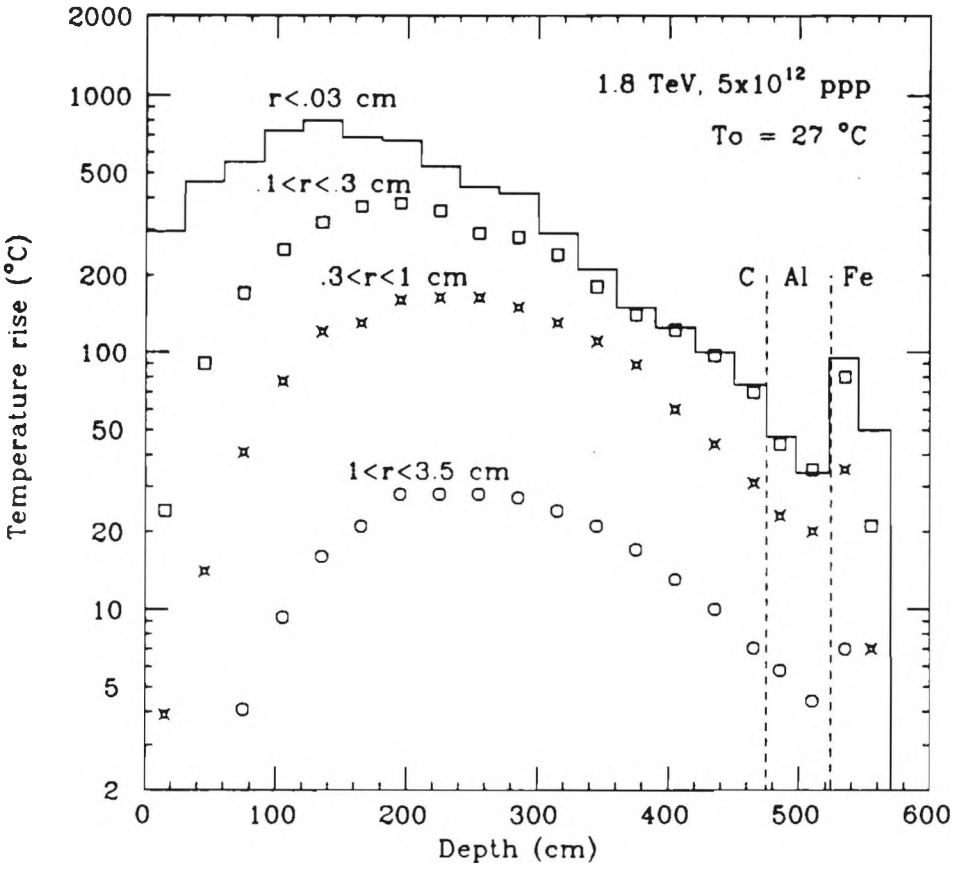

Figure 5.3.4 Instantaneous temperature rise distribution correspondingly to Fig. 3 for the beam abort of 5×10^{12} protons.

that essentially no high energy protons leave the dump and hence long distance irradiation into the machine lattice is minimal. The kicker magnets also serve as absorbers to further decrease the flux in the forward direction.

Calculations show that the maximum energy deposition density in the first quadrupole superconducting coils is ~ 3×10^{-6} Gev per gram per incident proton on the reference trajectory. With 2×10^{12} incident particles this gives 0.01 mJ per gram of deposited energy which is a factor of at least 50 below the quench threshold.

The energy deposition increases as the incident beam moves away from the reference trajectory i.e. less far into the dump. The aborted beam trajectory can always differ from the reference due equipment malfunctions of the type that the abort system must protect the accelerator from. The minimum beam offset at the dump for a clean abort is ~4mm, which corresponds to a vertical orbit error of ~8mm in the arcs.

Shielding

Averaged over a year of operation the tolerable flux of hadrons with an energy > 10 Mev at the outer surface of the shield is ~ 10^7 particles/cm^2 sec. This value gives ~100 mrad/hr of contact dose of induced and is acceptable from the ground water activation point of view (a flux of 10^6 to the water). Assuming a 50% operating time per year then this consideration requires the aluminium dump container must be surrounded by a steel shield of outer radius 25 cm as shown in fig. 5.3.2

Muons

For the design parameters one needs to have ~1.5 km of soil shield in the direction of the aborts to provide on the surface an annual dose of <10 $mrem^3$. The minimum thickness of soil above the aborted beam axis and the dump should be ~4m. The Fermilab tunnel fulfills these conditions and the only requirement is to kick the beams downwards.

Lifetime

The yearly integrated hadron dose at the hottest point in the dump is in the range $1.5 - 4 \times 10^{18}$ cm^{-2}. The allowable flux before radiation damage for graphite in an inert atmosphere id ~ 10^{20} cm^{-2}. The dump lifetime will be many years.

References

1 N.V. Mokhov. Fermilab FN-328 (1980)

2 Superconducting Accelerator Design Report, Fermilab (1979)
M.A. Maslov and N.V. Mokhov, Part. Accel., Vol.11, Pg.91 (1980)
A.I. Drozhdin, M. Harrison and N.V. Mokhov. Fermilab FN-418 (1985)

3 Radiation Guide, Fermilab (1983)

4 I.S. Baishev, S.L. Kuchinin and N.V. Mokhov. Preprint IHEP 86-76
Serpukov (1986)

5 Y.S. Toulokian. Thermophysical Properties of Matter. Vol.1, Plenum,
New York - Washington (1970)

6 N.V. Mokhov and M. Harrison, to be published Snowmass 88 proceedings

VI. TEVATRON LOW BETA DESIGN

VI.1. Lattice

The construction of a colliding beam facility at the D0 long straight section of the Collider, coupled with the presence of CDF at the B0 straight section of the Collider, has produced the need for a low beta insertion that unlike the system presently installed at B0, permits the simultaneous and essentially independent operation of more than one low beta insertion.

The new "D0 low beta insertion" enables simultaneous operation of multiple low beta insertions by matching each insertion to the arcs of the accelerator in betatron and momentum space. Matched low beta insertions in the Collider are independent except for the need to maintain a constant tune with distributed tune correction quadrupoles. The addition of each low beta insertion to the accelerator lattice raises the tune of the accelerator approximately a half integer unless compensated. The vertical and horizontal tunes of the Collider with low beta insertions at B0 and D0 are 20.59 and 20.58 respectively.

The insertions at B0 and D0 will eventually be optically identical. The currently operating low beta insertion at B0 produces a large dispersion wave and will be replaced. The number and location of the new low beta elements in the accelerator lattice are shown in Figure 6.1.1 and dimensioned in Figure 6.1.2. Each insertion is composed of 18 quadrupoles that are physically placed approximately symmetric around the straight section and have magnetic gradients that are antisymmetric relative to the center of the straight section. A field free region, 15.24 m long and equal to the field free region presently available to the detector at B0, has been left for the detectors. Two 9 m long regions located between Q1 and Q2 on both sides of the interaction region are reserved for the future installation of electrostatic separators.

Two new cold iron quadrupoles have been developed for the "D0 low beta insertion"; a 1.4 T/cm, 2-shell quadrupole and a .7 T/cm, 1-shell quadrupole. Quadrupoles Q1 through Q5 and T6 are 1.4 T/cm magnets; quadrupoles T7 through T9 are 1-shell magnets. The 1.4 T/cm magnets have essentially the same aperture as the quadrupoles utilized in the older B0 low beta insertion but have gradients which are 40% stronger. The availability of higher gradient quadrupoles permits a low beta insertion which can be programmed down to a β^* value of 25 cm, a fourfold reduction in β^* relative to the older B0 insertion design value.

Figure 6.1.1

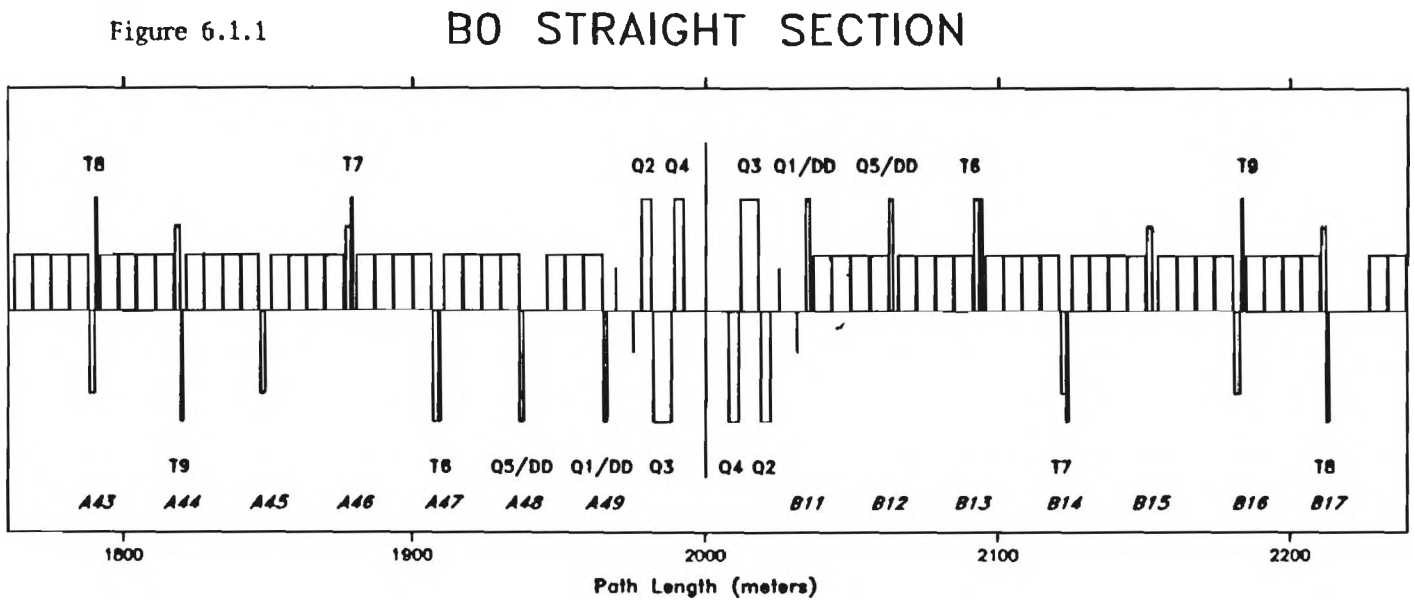

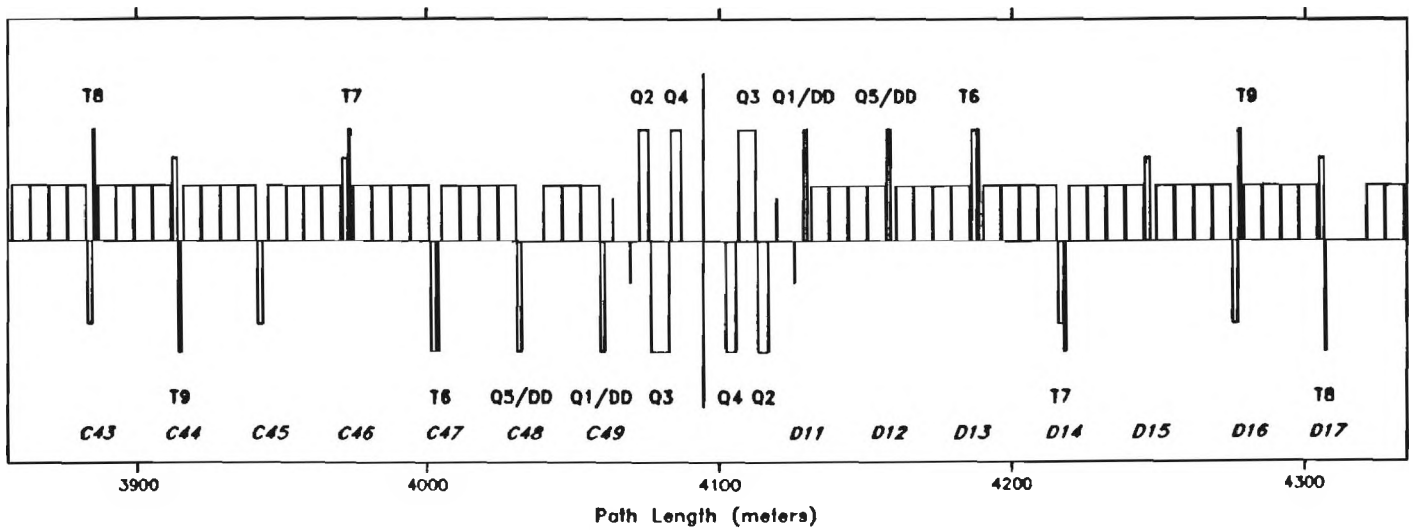

Figure 6.1.1

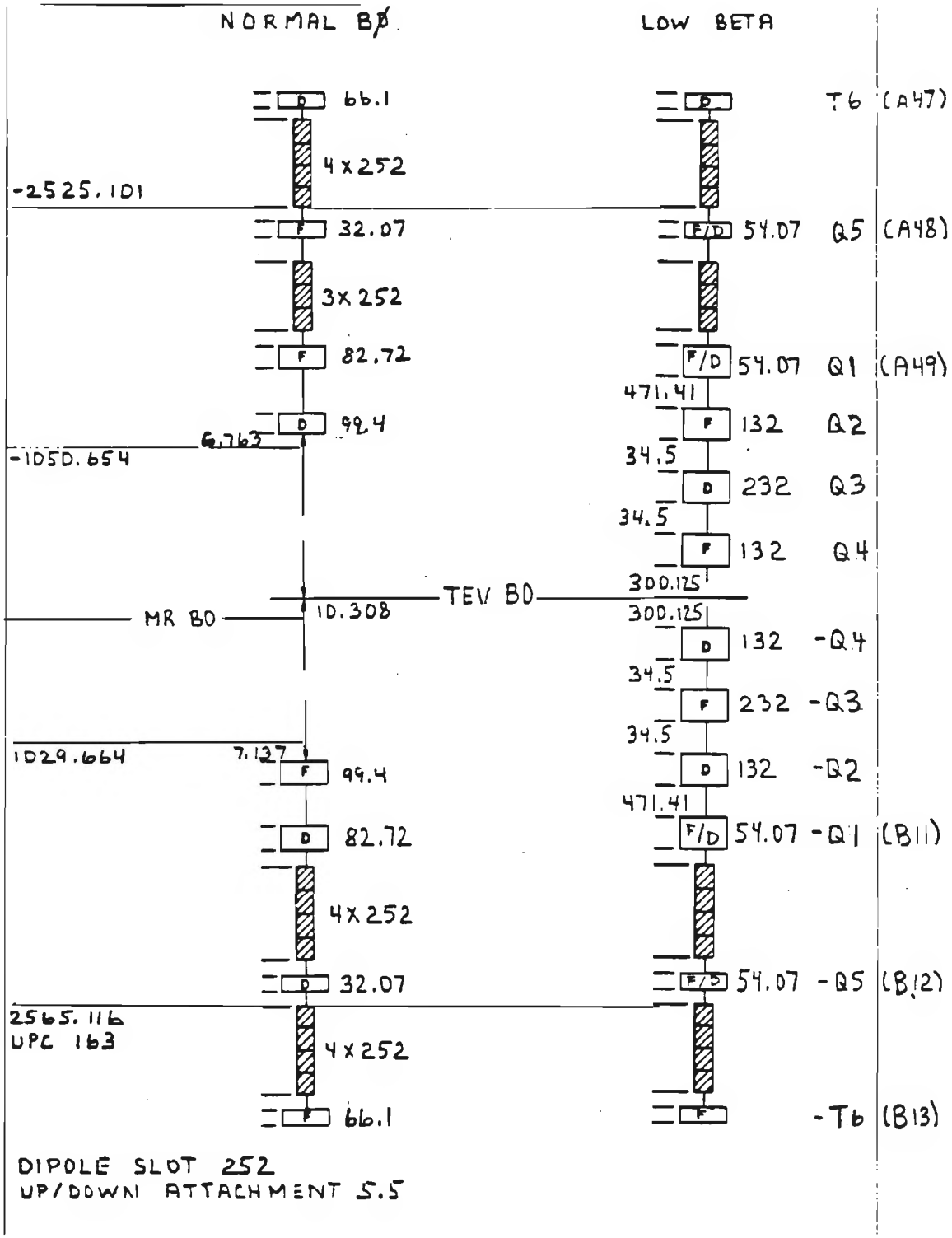
NORMAL BØ
LOW BETA
66.1
4X252
-2525.101
32.07
3X252
82.72
99.4
6.763
-1050.654
MR BØ
10.308
TEV BØ
7.137
1029.664
82.72
4X252
32.07
2565.116
UPC 163
4X252
66.1
DIPOLE SLOT 252
UP/DOWN ATTACHMENT 5.5
T6 (A47)
54.07 Q5 (A48)
54.07 Q1 (A49)
471.41
132 Q2
34.5
232 Q3
34.5
132 Q4
300.125
300.125
132 -Q4
34.5
232 -Q3
34.5
132 -Q2
471.41
54.07 -Q1 (B11)
54.07 -Q5 (B12)
-T6 (B13)

Figure 6.1.2

Figures 6.1.3 and 6.1.4 show the beta functions and horizontal dispersion of a low beta insertion for a β^* value of 25 cm. The β functions follow the symmmetry of the low beta quadrupole gradients and are approximately antisymmetric relative to the center of the insertion. The peaks in the β functions (1600 m), the bore tube and unavoidable field errors in the low beta quadrupoles combine to set the lower β^* limit for the lattice. The lack of symmetry in dipole placement explains the lack of symmmetry of the horizontal dispersion through the straight section. The horizontal dispersion is approximately zero at the interaction point. The vertical dispersion is essentially zero throughout the ring.

The required low beta insertion gradients for a 25 cm through 1.7 m β^* range with B0 and D0 operating at equal β^* values and a beam energy of 1 Tev is shown in Table 6.1.1. QFC and QDC are the gradients of the distributed tune correction quadrupoles which maintain a constant tune as β^* varies. Beam injection occurs at Step 1 with the low beta quadrupole gradients scaled to the 150 Gev injection energy. After acceleration, the low beta gradients are programmed to obtain the desired β^* at the interaction regions. The gradients listed in Table 6.1.1 are only valid if B0 and D0 have the same β^* values. If B0 and D0 have different β^* values or a third low beta insertion is added to the Collider, the gradients will have to be recomputed at the new tune correction quadrupole values.

VI.2. Magnet Specifications and Design

Two-shell Quadrupole.

The cross-section of the 1.4 T/cm low beta quadrupole is shown in Figure 6.2.1. The quadrupole is a cold iron, 2-shell superconducting magnet with a cryostat based on the design of the SSC dipole. The coils are rigidly clamped with aluminum collars which in turn are clamped by the cold iron magnetic yoke. Channels located at the 4-fold symmetric low field regions of the yoke are used to align in azimuth the collared coil to the yoke or contain high current buses and instrumentation leads. A zero clearance stainless steel shell surrounds the yoke and is longitudinally seam-welded to produce a rigid "cold mass". The cold mass is surrounded by a 2-phase helium channel, a liquid nitrogen temperature shield and a thick-walled vacuum vessel. Shorter versions of the SSC style post support the cold mass and the heat shields within the steel vacuum vessel. The load line of the 2-shell quadrupole is shown in Figure 6.2.2. The quadrupole will reach the required peak gradient of 1.4 T/cm at a nominal current of 4.8 kA.

A partial specification of the 2-shell quadrupole is listed in Table 6.2.1. The coil structure is typical of NbTi magnets now developed for accelerator

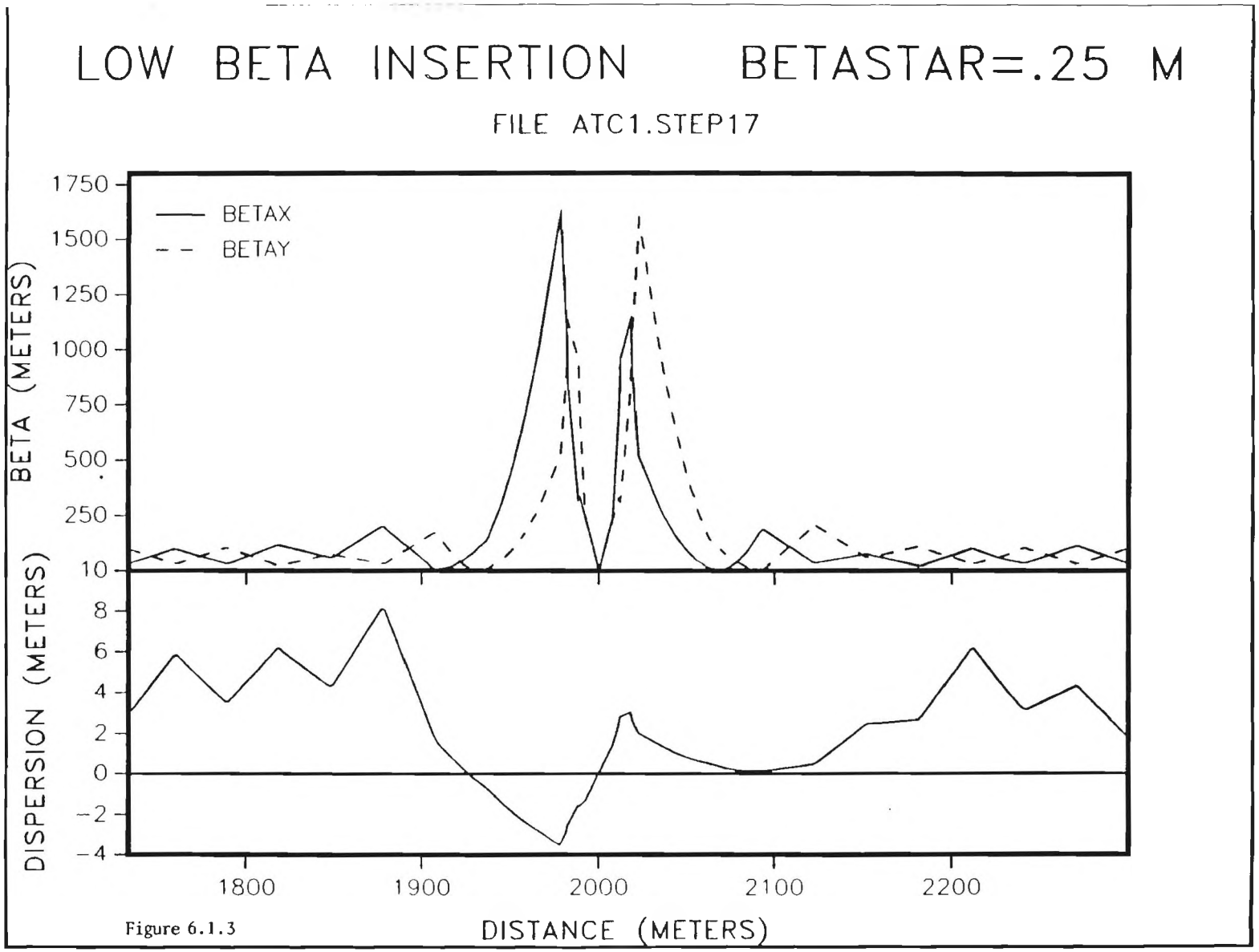
LOW BETA INSERTION BETASTAR=.25 M
FILE ATC1.STEP17
BETAX
BETAY
BETA (METERS)
1750
1500
1250
1000
750
500
250
10
DISPERSION (METERS)
8
6
4
2
0
-2
-4
1800
1900
2000
2100
2200
DISTANCE (METERS)

Figure 6.1.3

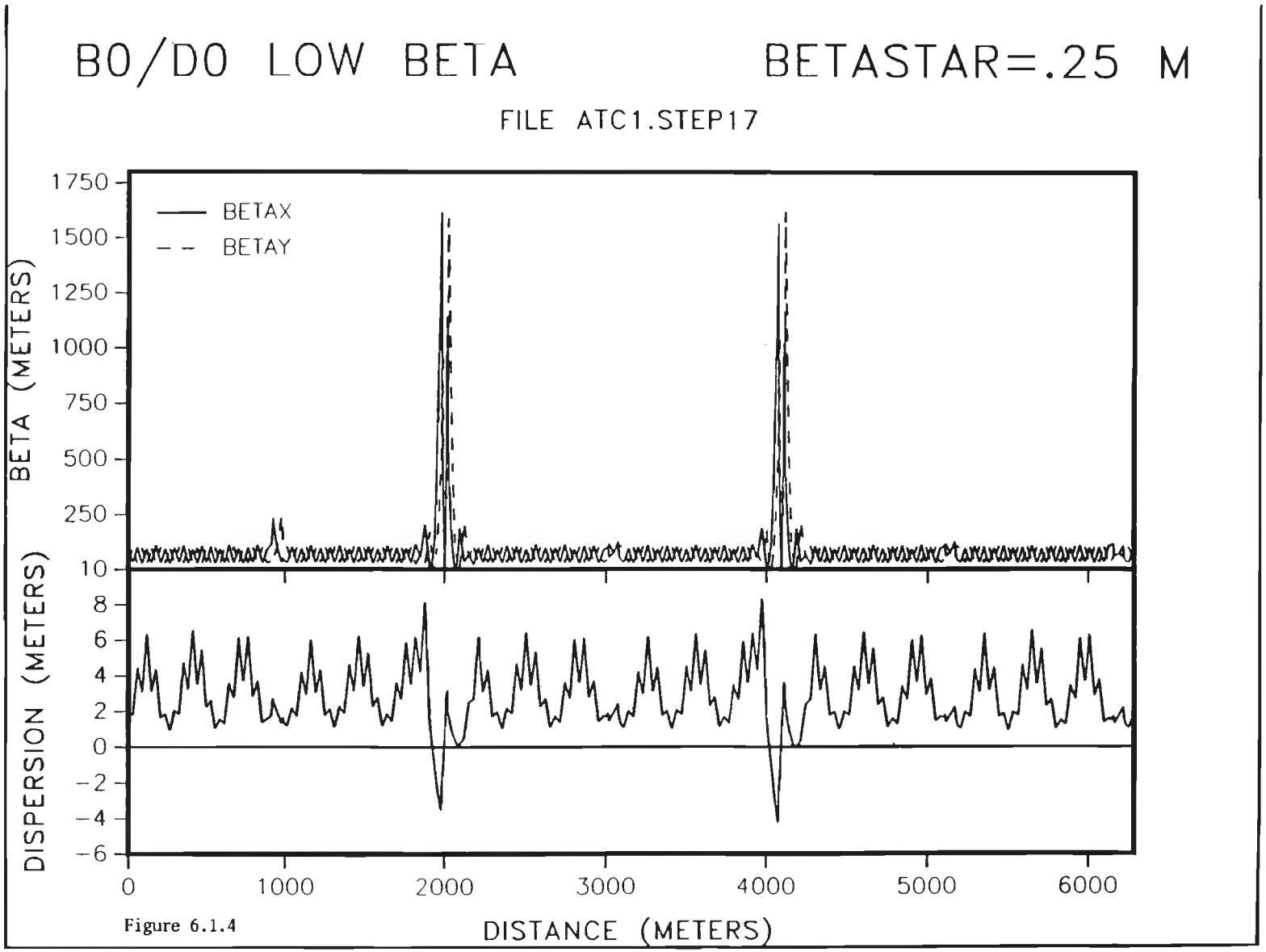
B0/D0 LOW BETA
BETASTAR=.25 M
FILE ATC1.STEP17
BETAX
BETAY
BETA (METERS)
DISPERSION (METERS)
1750
1500
1250
1000
750
500
250
10
8
6
4
2
0
-2
-4
-6
0
1000
2000
3000
4000
5000
6000
DISTANCE (METERS)

Figure 6.1.4

TABLE 6.1.1 SQUEEZE PARAMETERS FOR LOW BETA INSERTION
GRADIENTS IN KG/M FILE ATC1
T6 THROUGH T9 ARE TRIM MAGNETS IN SPOOLS
TRIMS ASSUME A MAGNETIC LENGTH OF 30"

STEP	Q4	Q3	Q2	Q1	Q5	T6	T7	T9	T8	QFC	QDC
INJ	1401.3	-1347.70	1401.3	-686.80	821.70	449.6	441.0	-294.0	-87.6	-1.77	4.63
						-513.7	-453.5	354.7	96.0		
2	1401.3	-1364.90	1401.3	-447.40	700.00	483.6	437.4	-281.8	-82.2	-3.68	4.82
						-600.7	-420.4	342.2	92.6		
3	1401.3	-1362.20	1401.3	-363.20	600.00	507.3	426.0	-302.2	-73.1	-6.21	5.36
						-626.8	-404.1	379.2	103.3		
4	1401.3	-1366.80	1401.3	-304.80	500.00	527.2	416.4	-298.6	-71.2	-7.59	7.50
						-656.2	-400.5	363.5	98.3		
5	1401.3	-1371.20	1401.3	-253.60	400.00	549.0	406.8	-298.2	-57.2	-9.75	9.69
						-681.0	-392.1	370.1	82.4		
6	1401.3	-1373.80	1401.3	-210.70	300.00	570.5	396.6	-293.6	-54.4	-10.80	10.89
						-604.2	-384.6	362.8	80.2		
7	1401.3	-1376.70	1401.3	-172.10	200.00	583.5	384.5	-297.9	-37.6	-12.30	13.35
						-617.1	-378.4	350.7	48.7		
8	1401.3	-1378.50	1401.3	-139.80	100.00	602.7	375.4	-295.8	-28.4	-13.33	14.72
						-634.3	-372.1	340.6	34.0		
9	1401.3	-1380.00	1401.3	-110.6	0.00	620.5	366.2	-299.1	-21.9	-14.15	15.70
						-653.4	-364.6	340.3	26.7		
10	1401.3	-1381.4	1401.3	-85.6	-100.00	632.2	356.5	-297.2	-4.7	-14.87	17.49
						-653.2	-360.4	310.2	-11.1		
11	1401.3	-1381.9	1401.3	-64.0	-200.00	666.6	351.5	-297.7	-1.8	-15.55	17.97
						-687.0	-354.8	308.5	-9.8		
12	1401.3	-1382.1	1401.3	-42.5	-300.00	707.1	349.4	-310.8	-6.0	-16.51	18.05
						-748.2	-350.9	349.6	17.3		
13	1399.8	-1382.4	1399.8	-12.8	-431.10	741.8	344.6	-319.7	6.8	-17.67	19.26
						-786.1	-347.2	356.1	6.6		
14	1400.6	-1382.1	1400.6	4.4	-581.50	818.3	344.9	-312.7	10.8	-18.34	19.47
						-868.3	-339.4	346.0	1.8		
15	1400.7	-1380.6	1400.7	4.5	-683.70	890.0	365.0	-333.3	29.9	-21.01	21.99
						-960.3	-369.6	403.8	-10.2		
16	1401.1	-1379.4	1401.1	-1.7	-696.80	967.6	381.9	-309.7	31.6	-20.96	23.95
						-1039.6	-400.7	373.8	-47.6		
17	1400.8	-1377.6	1400.8	-3.7	-689.70	1058.0	416.5	-335.0	63.2	-24.43	27.65
						-1120.0	-442.4	368.6	-84.6		

STEP	BSTAR	BXMAX	BYMAX	ETAMAX
INJ	1.75	241	252	6.3
2	1.43	285	284	6.2
3	1.25	305	305	6.4
4	1.1	351	345	6.5
5	.97	398	400	6.6
6	.875	442	441	6.5
7	.785	494	493	6.8
8	.71	547	546	6.9
9	.65	599	597	7.0
10	.59	668	666	7.3
11	.54	730	729	7.3
12	.5	789	784	7.4
13	.45	876	870	7.7
14	.4	1026	980	7.8
15	.35	1120	1160	8.1
16	.29	1383	1355	7.8
17	.25	1614	1614	8.3

Low-Beta Quad

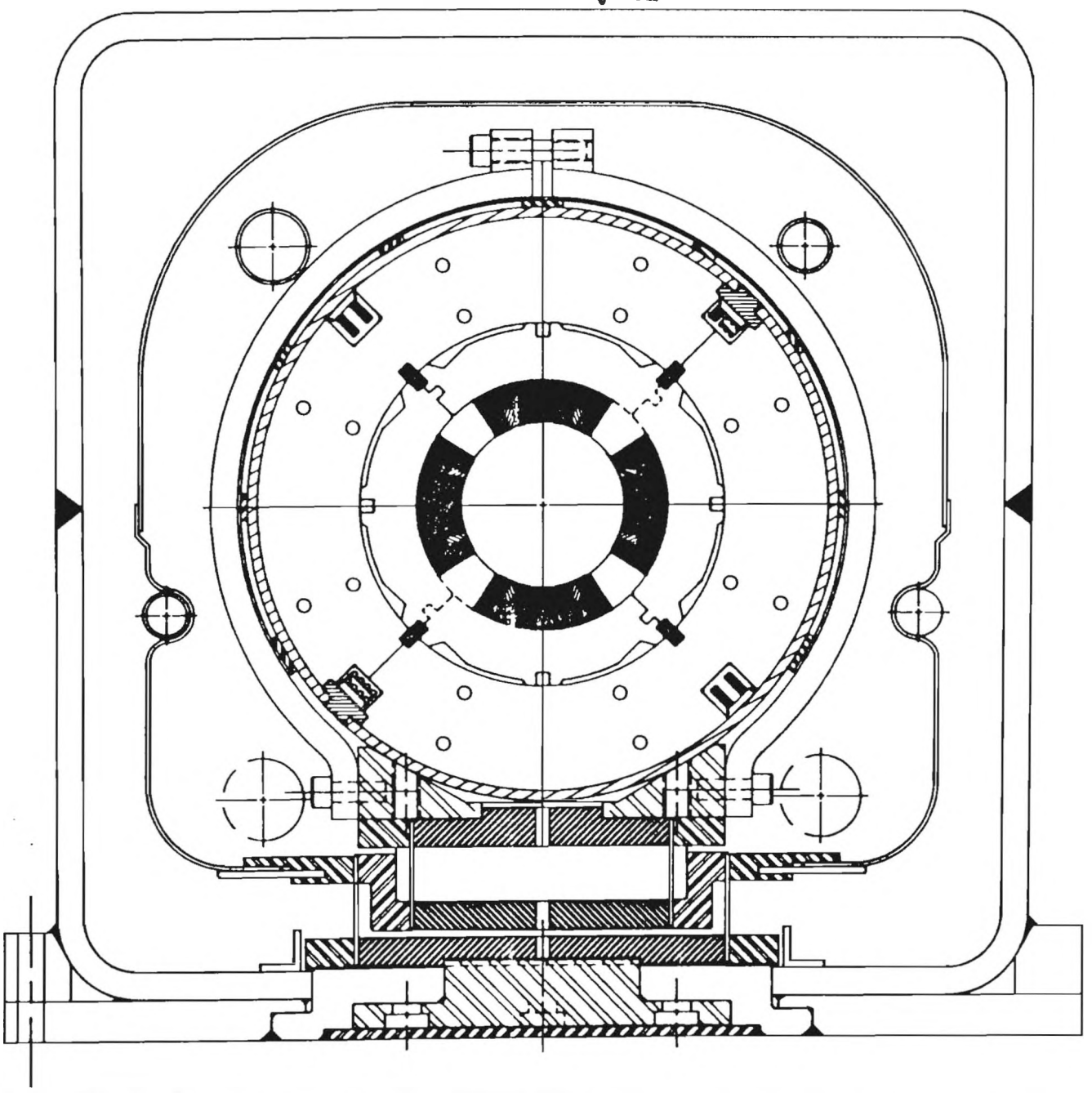

Figure 6.2.1

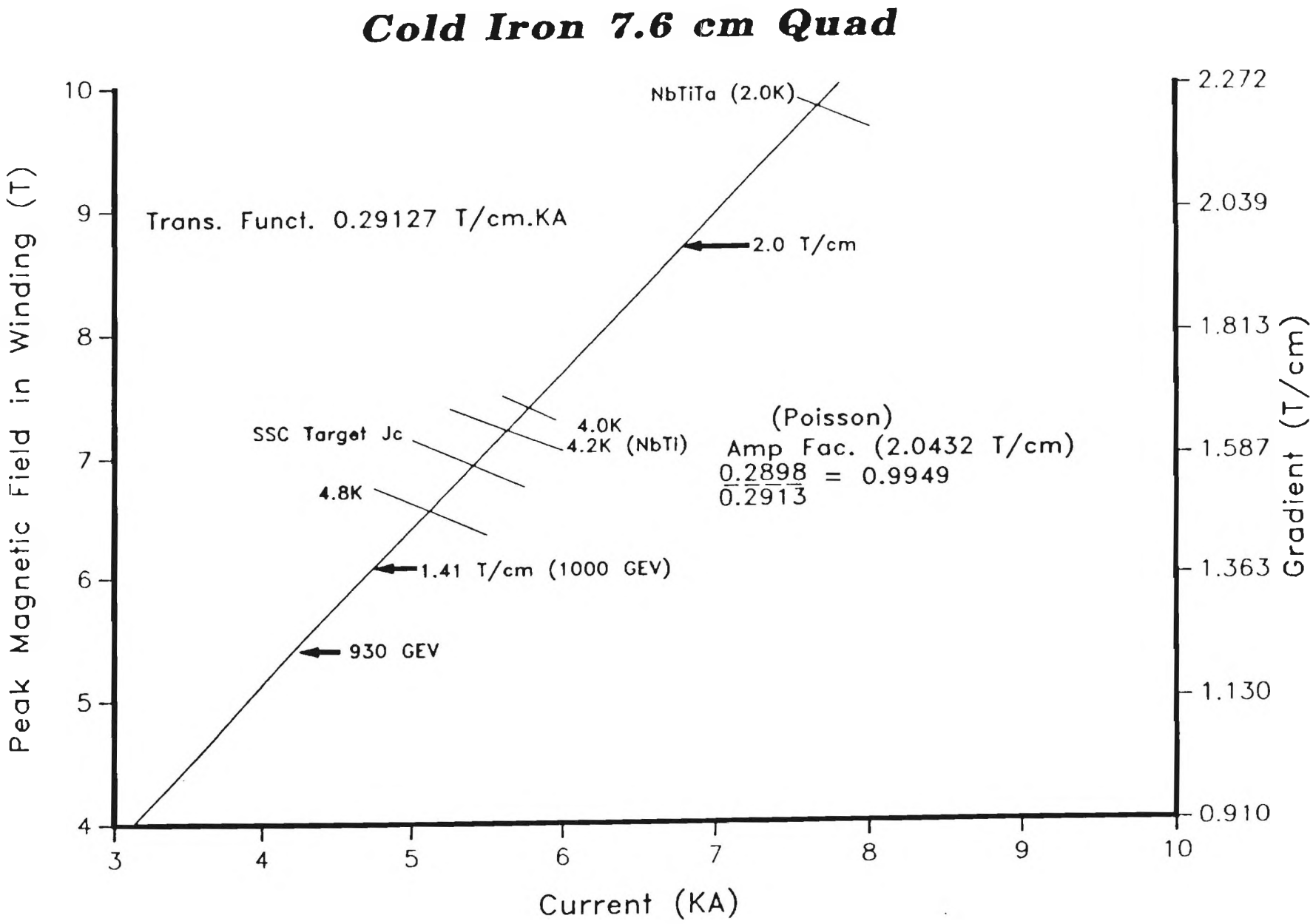
Cold Iron 7.6 cm Quad
NbTiTa (2.0K)
Trans. Funct. 0.29127 T/cm.KA
2.0 T/cm
SSC Target Jc
4.0K
4.2K (NbTi)
4.8K
(Poisson)
Amp Fac. (2.0432 T/cm)
0.2898 / 0.2913 = 0.9949
1.41 T/cm (1000 GEV)
930 GEV
Peak Magnetic Field in Winding (T)
Gradient (T/cm)
Current (KA)
10
9
8
7
6
5
4
3
4
5
6
7
8
9
10
2.272
2.039
1.813
1.587
1.363
1.130
0.910

Figure 6.2.2

Table 6.2.1 2-Shell Magnet Specifications

Superconductor

Alloy	NbTi
Strand diameter (inches)	$.0208^{+.0002}_{-.0000}$
Number of strands	36
Strand twist (twist/inch)	2 left hand
Copper to superconductor ratio	1.5:1
Number of filaments	612
Filament diameter (μm)	13
Minimum filament spacing (μm)	>1.5
J_c 4.2(4.6)K 5T (A/mm^2)	3000 (2600)
J_c 4.2 K 8T (A/mm^2)	1350
J_c 1.8 K 8T (A/mm^2)	2560

Cable

Twist length (inches)	2.85 to 3.2 right hand
Mid-thickness (inches)	.0353 +/- .0006
Width (inches)	0.385 +/- .0005
Keystone angle (degrees)	1.06 +/- .03
Insulation (inches)	.001 x .375 Kapton .0001 B-stage coated right hand wraps total insulation appr. .003

Coils

	Inner	Outer
Turns per pole	19	28
Number of wedges	1	1
Inner dia. w/o ins. (inches)	3.008	3.814
Outer dia. w/o ins. (inches)	3.778	4.584

Cold mass inductance (calculated)	7.58 mH/m
Yoke inner diameter (inches)	6.692
Yoke outer diameter (inches)	10.5

Calculated body harmonics radius = 1.0 inch	pole=	10^4
	4	0.46
	12	-0.15
	20	1.20
	28	-0.53
	36	0.0014
	44	0.012
	52	

systems. The significantly higher gradient of the quadrupole is due to gains in the critical current density of superconducting cable. The field harmonics far from the ends of the quadrupole have been evaluated at a radius of 2.54 cm using the MAGFLD and POISSON computer codes. The 12-pole and 20-pole have been reduced with copper wedges. The quadrupole ends will be made "neutral" by spacing the end turns with spacers. The actual magnet field quality will also depend on construction errors which can introduce other normal and skew harmonics, principally a sextupole component.

Single-Shell Quadrupole

The 1-shell magnets replace unused correction magnets in existing spools adjacent to lattice quadrupoles flanking the low beta straight section and therefore do not require a new cryostat design. The cross-section of the 1-shell cold mass is shown in Figure 6.2.3. In order to reduce the operating current (Figure 6.2.4) and the heat load from the power leads, this magnet is wound with 5-in-1 cable. Each pole has 13 turns and each turn contains 5 insulated monolithic conductors for an effective 65 turns per pole. The monolithic conductors are manufactured from the same superconducting material as the 2-shell magnets. A partial specification for the 1-shell quadrupole is given in Table 6.2.2. As in the 2-shell quadrupole, shims have been used in the coil and end turns to minimize the 12-pole and 20 pole.

VI.3. Magnet Support Systems

Power Circuit and Quench Protection

The β^* values of the low beta insertions are adjusted by powering the low beta magnets with separate power circuits. The required power circuits per insertion are shown in Figure 6.3.1. The number of power circuits has been reduced from 18 to 11 by utilizing the magnetic symmetry of the 5 inner quadrupole pairs; because the Q2 and Q4 gradients are equal; and by adding shunt regulators to the T6 quadrupole circuit. The maximum current required by each circuit is shown in Table 6.3.1. The five inner circuits will utilize 7.5 kA, 50 V power supplies initially designed to power the older low beta insertion at B0. The outer circuits - T7,T8,T9 - will use new 1.5 kA, 15 V power supplies.

Table 6.3.1 Low Beta Magnet Lengths, Fields and Currents

Magnet Number	Magnetic Length (cm)	Maximum Gradient (T/cm)	Maximum Current (A)

Q1	137.34	.5858	2011
Q2	335.28	1.4013	4811
Q3	589.28	1.3824	4746
Q4	335.28	1.4013	4811
Q5	137.34	.8217	2821
Q6	60.64	1.4070	4832
T7	54.61	.6328	1086
T8	54.61	.1441	247
T9	54.61	.5634	967

The basic power circuit is shown in Figure 6.3.2. Quenches are detected with a microprocessor by comparing the measured voltages across the four equal inductive elements of the circuit. Depending on the specific power circuit, the inductive elements in Figure 6.3.2 are individual quadrupole magnets (Q2,Q4 circuit), half of a quadrupole magnet (Q1, Q3, Q5, and T6 circuits),or one fourth of a quadrupole magnet (T7, T8, and T9 circuits). When a quench is detected by the microprocessor, it reduces the power supply voltage to zero and fires the magnet quench heaters. Each magnet contains two quench heaters energized by separate heater power supplies for redundancy. The spontaneous and heater induced quench resistances and the other circuit resistances then cause the magnet current to decay through the bypass diodes of the power supply.

Refrigeration System

The new low beta magnets have been designed to operate at a peak temperature of 4.8 K. They will be cooled to a nominal temperature of 4.6 K by attaching them to the accelerator magnets on either side of the low beta straight section. The additional heat load and liquid helium load for the satellite refrigerators on either side of the low beta straight sections is shown in Table 6.3.2. The larger liquid helium load of the new low beta system will have to be supplied by the Central Liquefier. The satellite refrigerators should have no difficulty with the added heat load. The older low beta system presently in operation at B0 is also attached to the satellite refrigerators. Its additional heat load per satellite has been measured at approximately 100 W.

VI.4. Lattice Options

Fixed Target

The accelerator will alternate between colliding beam operation and fixed target operation during the foreseeable future. In order to extract beam

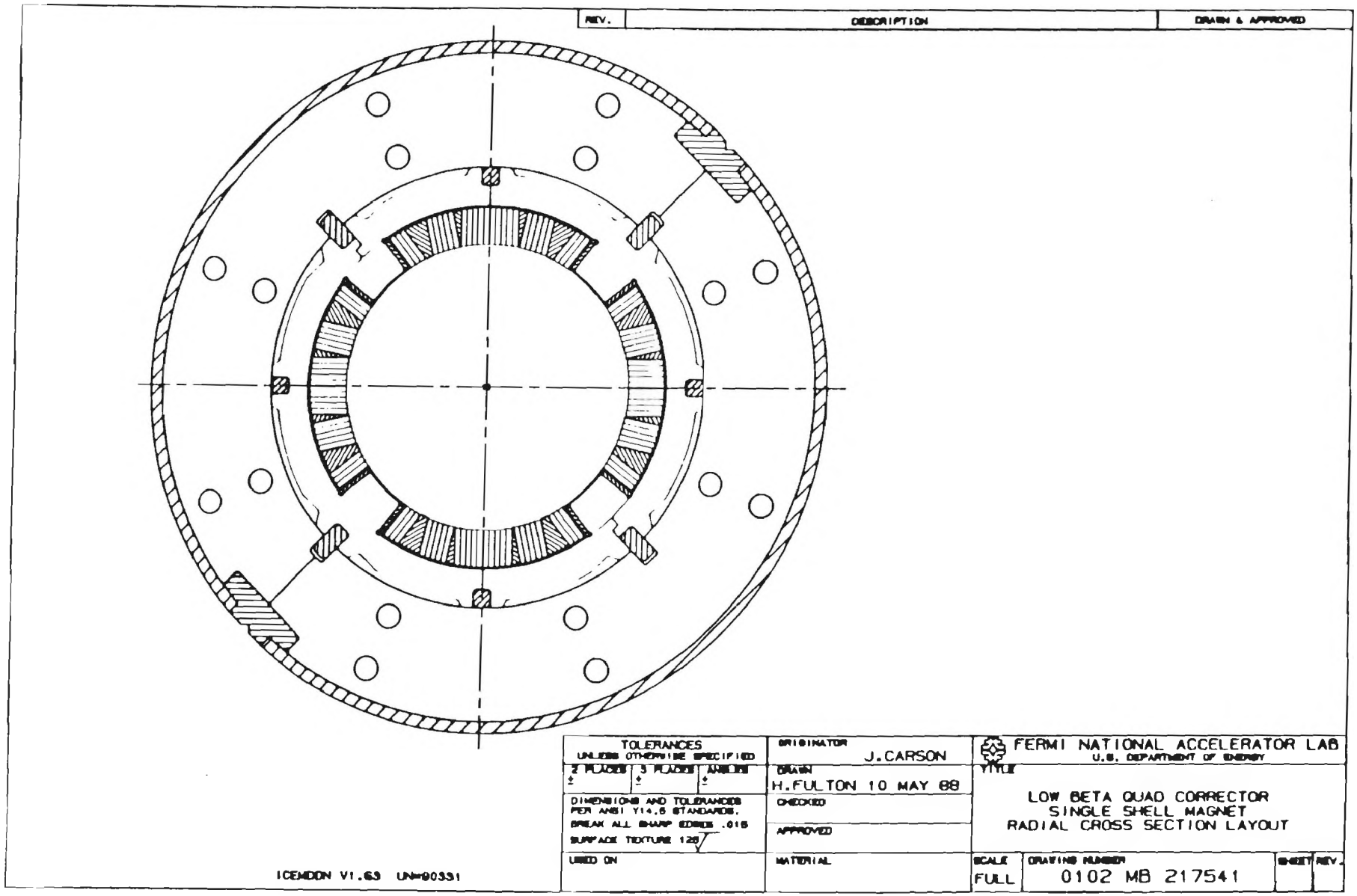
REV.
DESCRIPTION
DRAWN & APPROVED
TOLERANCES
UNLESS OTHERWISE SPECIFIED
2 PLACES ±
3 PLACES ±
ANGULAR ±
DIMENSIONS AND TOLERANCES PER ANSI Y14.5 STANDARDS.
BREAK ALL SHARP EDGES .015
SURFACE TEXTURE 125
USED ON
ORIGINATOR J.CARSON
DRAWN H.FULTON 10 MAY 88
CHECKED
APPROVED
MATERIAL
FERMI NATIONAL ACCELERATOR LAB
U.S. DEPARTMENT OF ENERGY
TITLE
LOW BETA QUAD CORRECTOR
SINGLE SHELL MAGNET
RADIAL CROSS SECTION LAYOUT
SCALE FULL
DRAWING NUMBER 0102 MB 217541
SHEET
REV.
ICEMDDN V1.63 UN=00331

Figure 6.2.3

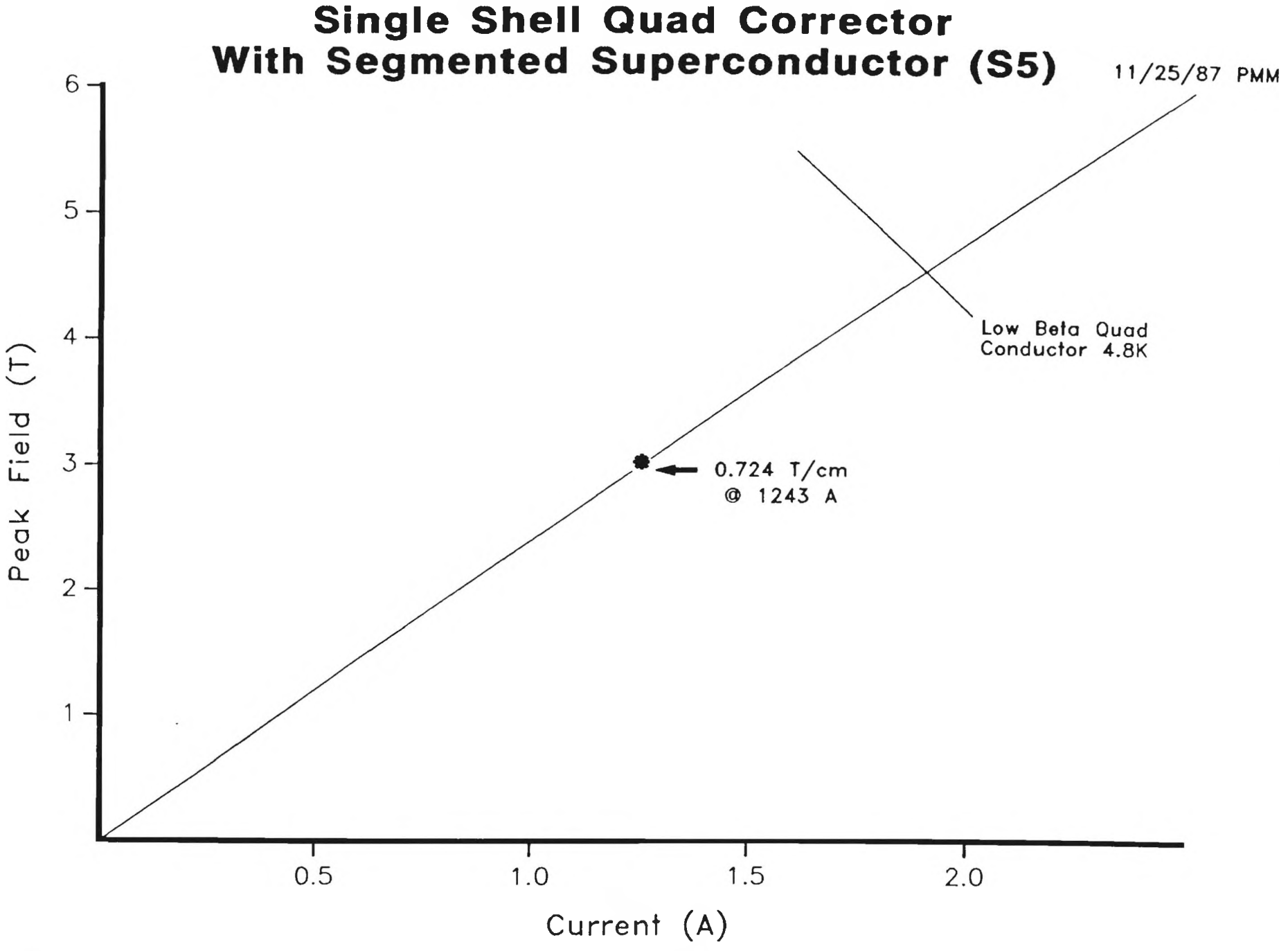
Single Shell Quad Corrector
With Segmented Superconductor (S5)
11/25/87 PMM
Low Beta Quad
Conductor 4.8K
0.724 T/cm
@ 1243 A
Peak Field (T)
Current (A)
1
2
3
4
5
6
0.5
1.0
1.5
2.0

Figure 6.2.4

Table 6.2.2. 1-shell Magnet Specifications

Superconductor

Alloy	NbTi
Copper to Superconductor ratio	1.5:1
Number of filaments	630
Twist pitch (twists/inch)	2
Filament diameter (μm)	20
J_c 4.2 K 5T (A/mm^2)	3000
Conductor dimensions (inches)	0.043 x 0.0694
Insulation (inches)	2/3 lap 0.001 Kapton

Cable

Number of strands	5 identical paralled strands separately insulated
Insulated cable dimensions (inches)	0.391 x 0.053
Keystone	none

Coil

Number of turns per pole	13
Number of wedges	2
Inner diameter w/o insulation (inch)	3.008
Outer diameter w/o insulation (inch)	3.778

Cold mass inductance (calculated)	19.9mh/m
Yoke inner diameter (inches)	4.638
Yoke outer diameter (inches)	7.00

Calculated harmonics
radius = 1.0 inch

	Body	Integrated
pole= 4	10^4	10^4
12	0.000	0.000
20	0.000	0.000
28	0.899	0.800
36	-0.156	-.142
44	0.119	0.108
52	-0.004	-0.004

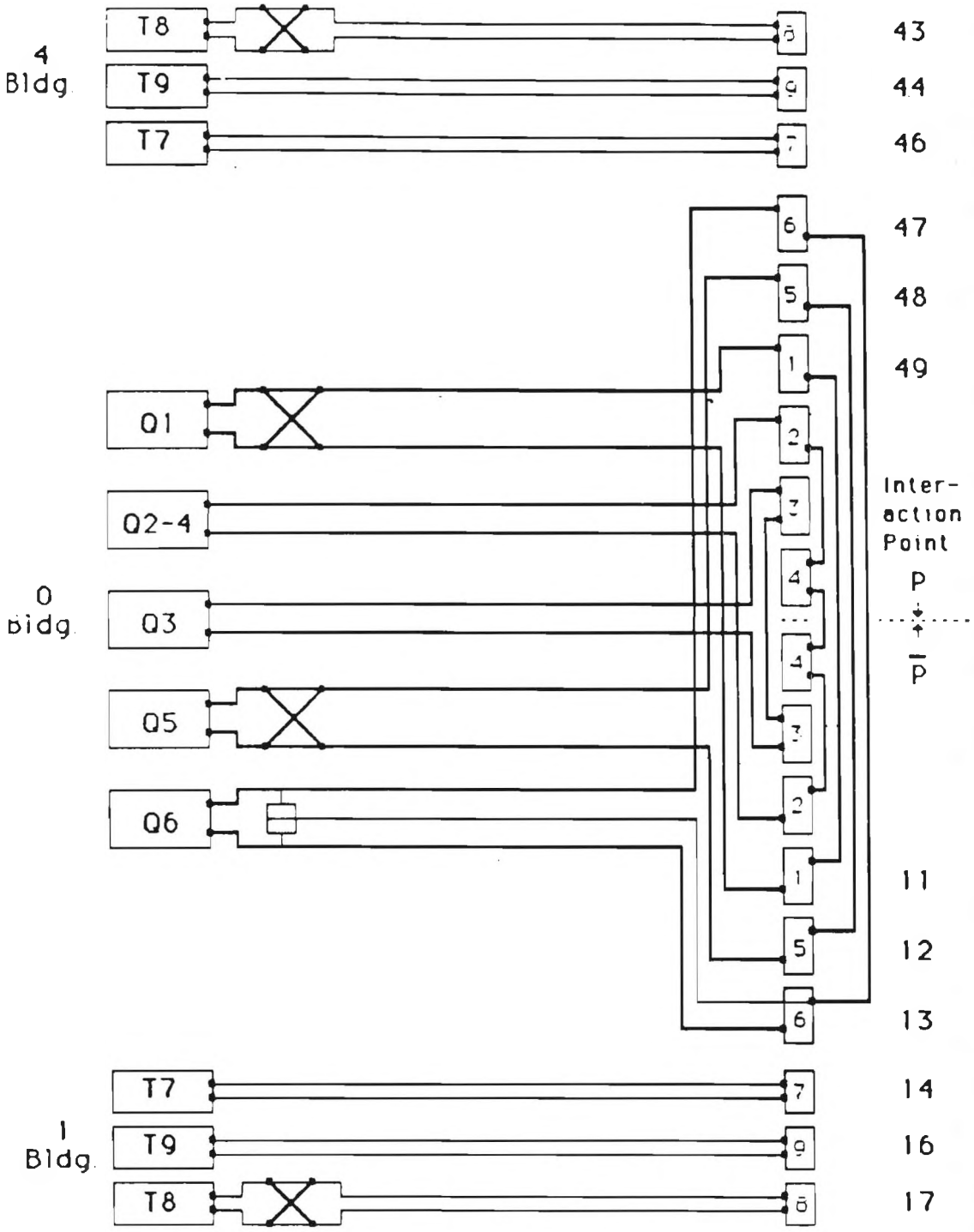
4
Bldg.
T8
T9
T7
43
44
46
47
48
49
Q1
Q2-4
0
Bldg.
Q3
Q5
Q6
Inter-
action
Point
P
P̄
11
12
13
1
Bldg.
T7
T9
T8
14
16
17

Figure 6.3.1

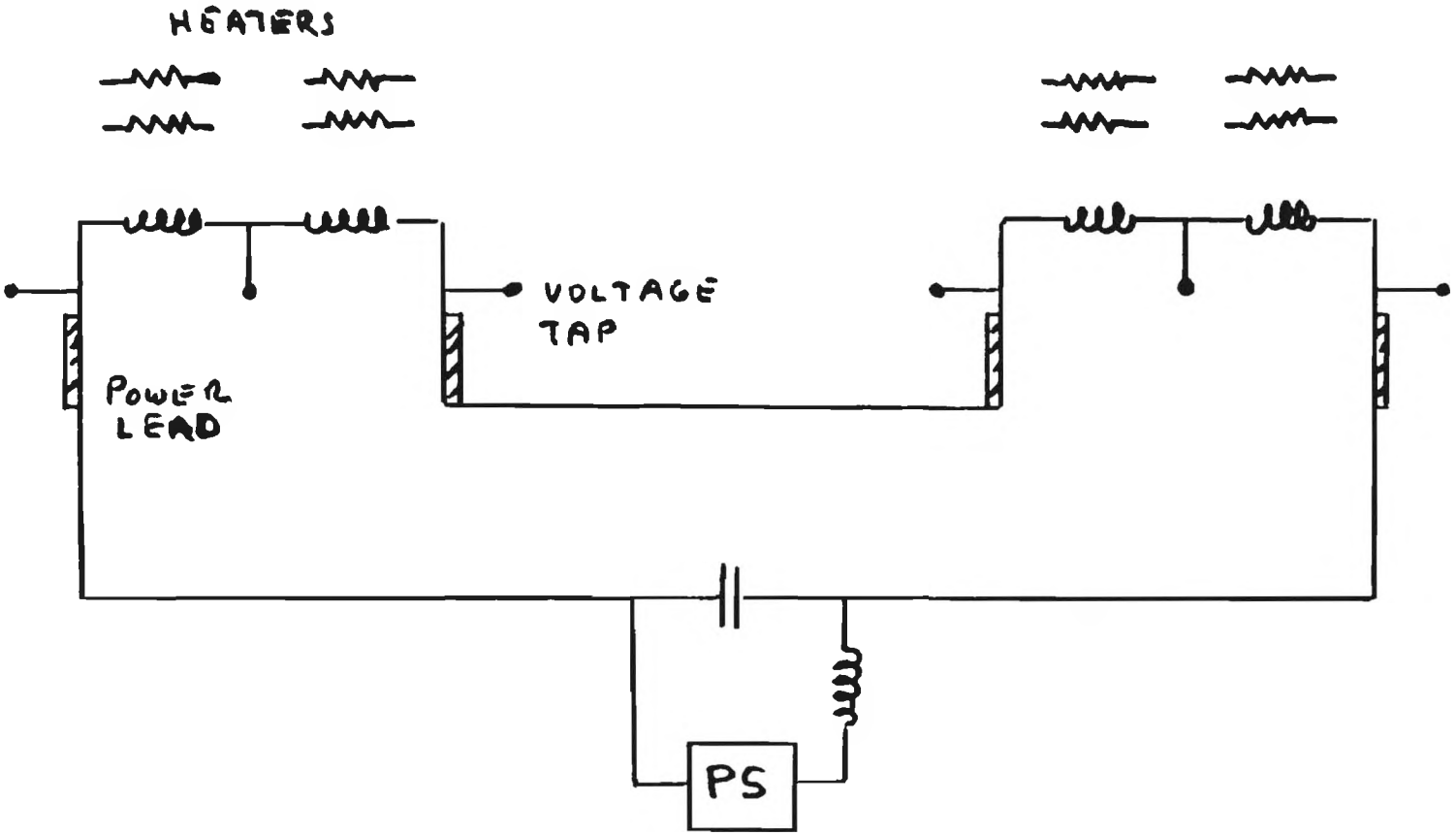

Figure 6.3.2

Table 6.3.2 D0 Low Beta Cryogenic Requirements

Component	# Leads	Lead Size amps	Existing Load watts	New Load watts	Lead Flow l/hr
Q4			0	12	
Q3			0	3	
Q2			0	3	
Six Power Lead Can	6	5000	0	15	82.5
Bypass			0	1	
New Spool	2	5000	10	15	27.5
Q1			5	3	
Barrier Box	2	5000	15	20	27.5
New Spool	2	5000	10	15	27.5
Q5			5	3	
T6 Spool	2	5000	10	15	27.5
T7 Spool	2	2000	10	13	11
T8 Spool	2	2000	10	13	11
T9 Spool	2	2000	10	13	11
Collins Quads			10	0	
Total Additional Heat Load				49	198
Increase per Refrigerator				6.4%	5.8%
Total Increase in CHL Consumption (B0 & D0)					14.7%

Notes:

1. Only loads for Q5 thru T9 were considered as additional loads for B0

2. Power lead flow requirements were based on 2.75 l/hr/kA/lead

3. The total CHL increase shown will require either the new higher capacity CHL or a considerable retuning of the satellite refrigerators

during fixed target operation, the D0 straight section lattice must be returned to the beam extraction geometry. The D0 detector, the D0 low beta components (Q1 through Q5), and the D0 fixed target extraction components are therefore designed to be readily moved in and out of the area.

The large filament diameter of the low beta quadrupoles (1-shell and 2-shell) degrades the ramp rate behavior of these magnets. The onset of reduced peak field in prototype 2-shell low beta magnets occurs at 100 A/sec. The Tevatron lattice magnets show little degradation until 300 A/sec. This is not a problem during colliding beam operation as the ramp rates of the infrequent acceleration cycle and β^* adjustment cycle can be lowered to the capabilities of the low beta magnets. During fixed target operation, the accelerator cycles as fast as possible to maximize the beam on target.

A modified fixed target lattice has been found that overcomes the low beta magnet ramp rate limitation. At the D0 straight section, Q1 through Q4 are physically removed,T6 through T9 are left unenergized, and the straight section matching quadrupoles (Collins quadrupoles) and extraction equipment are reinstalled. This leaves the D0 lattice configuration identical to the original fixed target lattice except for Q5 which now operates at reduced current and current rate. At the B0 straight section, none of the magnets need to be moved. During fixed target operation, magnets Q1, Q4, T6 through T9 are not energized and magnets Q2, Q3 and Q5 operate at reduced maximum current and current rate. The required gradients for the powered low beta magnets during fixed target operation and the lattice functions of the original fixed target lattice and the modified lattice at the A0, B0, D0 and E0 long straight sections are given in Table 6.4.1.

Interim Low Beta Lattices

In case B0 and D0 can not be modified simultaneously to the new low beta configuration, two interim low beta lattices have been developed which allow the low beta installation to occur in stages.

The first interim low beta lattice assumes that a complete "D0 insertion" is installed at the D0 straight section. At the B0 location, the old low beta insertion is retained, the straight section matching quadrupoles (Collins quadrupoles) are deenergized or removed to make room for electrostatic separators, and a set of trim quadrupoles (T6 through T9 as at D0) are added. These high field trim quadrupoles allow the old B0 insertion to be matched. The low beta gradients for this lattice are given in Table 6.4.2. The β^* value has been left constant at 1.8 m. The β^* value at B0 can be adjusted down to 44 cm.

Table 6.4.1 FIXED TARGET LOW BETA GRADIENTS AND LATTICE FUNCTIONS

FILE FT1 EXTRACTION LATTICE PRESENTLY IN USE

A48-1 GRADIENT Q1=368.89773 KG/M

POS	S(M)	NUX	NUY	BETAX(M)	BETAY(M)	XEQ(M)	YEQ(M)	ZEQ (M)	ALPHAX	ALPHAY	DXEQ	DYEQ
135 .A0	953.1750	2.89476	3.05461	105.21621	107.50143	2.41123	0.00000	2.8856	1.96228	-1.99286	-0.03084	0.00000
296 .B0	2000.2200	6.18013	6.23488	73.22077	72.46386	2.41789	0.00000	5.8672	-0.47395	0.47224	0.02061	0.00000
611 .D0	4094.7675	12.59581	12.75416	106.51418	105.61320	2.41703	0.00000	11.8256	1.97161	-1.95511	-0.03089	0.00000
766 .E0	5141.9650	15.88007	15.93568	72.14751	72.86369	2.42200	0.00000	14.8074	-0.46606	0.46240	0.02059	0.00000

MAXIMA --- BETX(609) = 244.81563 BETY(136) = 245.24295 XEQ(58) = 5.96543 YEQ(942) = 0.00000

File TCFT2B NEW LOW BETA LATTICE AT B0
EXTRACTION LATTICE AT D0 CONTAINS BO COLLINS' QUADS WITH REVERSED CURRENTS

B0 LOCAION		D0 LOCATION		GRADIENTS IN KG/M
Q4	= 0.	Q4	= REMOVED	
Q3	= -360.874	Q3	= REMOVED	
Q2	= 481.694	Q2	= REMOVED	
Q1	= 0.	Q1	= REMOVED	
Q5	= 423.028	Q5	= 217.93	
T6	= 0.	T6	= 0.	
T7	= 0.	T7	= 0.	
T8	= 0.	T8	= 0.	
T9	= 0.	T9	= 0.	

POS	S(M)	NUX	NUY	BETAX(M)	BETAY(M)	XEQ(M)	YEQ(M)	ZEQ (M)	ALPHAX	ALPHAY	DXEQ	DYEQ
135 .A0	953.1750	2.90083	3.06054	105.90026	106.53481	2.68612	0.00000	2.8689	1.96470	-1.97053	-0.03243	0.00000
301 .B0	2000.2200	6.15829	6.24404	115.43804	115.10410	3.31993	0.00000	5.8552	-1.43313	1.42712	0.04887	0.00000
628 .D0	4094.7676	12.57013	12.76593	127.86570	129.32129	2.72396	0.00000	11.8187	2.60346	-2.62127	-0.04307	0.00000
789 .E0	5141.9652	15.87462	15.93099	73.07905	72.28702	2.17870	0.00000	14.7799	-0.47234	0.46452	0.01885	0.00000

MAXIMA --- BETX(626) = 310.67276 BETY(629) = 310.52157 XEQ(867) = 6.10802 YEQ(965) = 0.00000

Table 6.4.2 SQUEEZE PARAMETERS FOR A MIXED MODE 1989 LOW BETA INSERT GRADIENTS IN KG/M
INPUT FILE [KOEPKE.TEVATRON]KK89.IN
T6 THROUGH T9 ARE HIGH FIELD TRIM MAGNETS IN SPOOLS - MAGNETIC LENGTH 30"

DØ GRADIENTS	Q4	Q3	Q2	Q1	Q5	T6	T7	T9	T8
1	1401.3	-1347.70	1401.3	-685.80	821.70	469.8	473.3	-267.5	-87.6
						-429.7	-413.7	391.5	95.0
2 THRU 17	1401.3	-1347.70	1401.3	-685.80	821.70	449.6	441.0	-294.0	-87.6
						-513.7	-463.5	354.7	95.0

BØ GRADIENTS

STEP	DJ1	DJ2	DJ3	DJ4	T6	T7	T9	T8	QFC	QDC
1	73.3	922.4	-678.3	141.9	349.4	292.6	-425.8	-329.2	7.89	-9.65
2	0.0	928.5	-682.1	152.5	362.0	269.0	-396.4	-296.8	9.72	-7.00
3	-50.0	932.5	-719.0	240.6	358.0	286.4	-345.2	-301.7	7.94	-4.82
4	-100.0	936.4	-758.0	328.6	354.3	303.7	-294.0	-306.5	5.16	-2.25
5	-200.0	943.0	-816.9	493.1	378.4	291.7	-333.4	-296.9	5.00	-3.00
6	-300.0	942.3	-885.3	682.9	328.7	267.3	-352.3	-301.7	5.00	-3.00
7	-400.0	944.4	-941.7	888.4	345.8	273.5	-340.2	-340.6	3.39	0.41
8	-500.0	952.0	-957.6	962.6	438.3	248.3	-393.5	-254.5	0.83	2.35
9	-600.0	950.9	-966.3	958.1	455.6	279.0	-363.3	-217.1	-3.10	6.18
10	-700.0	952.3	-971.5	958.5	458.7	278.0	-357.9	-214.5	-3.79	7.28
11	-800.0	952.1	-982.8	979.5	470.1	272.3	-368.2	-206.2	-5.03	8.54
12	-825.0	952.6	-986.8	979.0	488.0	294.0	-356.0	-203.0	-7.63	9.94
13	-850.0	953.3	-990.6	978.3	507.7	314.7	-344.5	-199.9	-10.27	11.62
14	-858.6	953.5	-992.5	984.9	518.3	321.2	-378.3	-147.0	-10.79	12.04
15	-867.1	953.8	-994.4	991.4	528.8	327.7	-412.0	-94.1	-11.28	12.44
16	-932.6	955.2	-995.8	997.9	478.2	344.1	-426.7	-44.1	-12.02	14.28
17	-932.6	955.2	-998.2	999.8	539.0	376.0	-508.8	44.5	-14.74	16.42
1					-286.9	-307.1	486.1	332.4		
2					-302.1	-254.4	335.6	273.2		
3					-382.3	-279.3	386.5	246.3		
4					-462.5	-304.2	397.3	219.4		
5					-399.3	-287.7	384.0	285.3		
6					-291.9	-257.5	391.0	274.9		
7					-456.0	-266.7	418.3	239.1		
8					-510.4	-238.0	429.9	214.5		
9					-560.1	-283.7	419.4	210.2		
10					-569.9	-286.6	420.6	199.0		
11					-570.8	-294.0	413.4	222.5		
12					-557.0	-312.0	465.0	225.6		
13					-544.6	-330.7	518.7	228.6		
14					-441.7	-308.7	447.3	124.5		
15					-338.8	-286.7	375.9	20.3		
16					-341.8	-307.5	359.9	-68.6		
17					-349.9	-329.7	330.9	-84.0		

STEP	BSTAR	BXMAX	BYMAX	ETAMAX
1	40.	278	307	6.3
2	45.	349	279	6.5
3	41.	343	342	6.5
4	34.	340	435	6.3
5	20.	401	405	6.2
6	7.5	442	404	6.2
7	4.3	452	518	6.3
8	5.1	504	489	6.6
9	2.6	689	651	6.4
10	2.3	790	741	6.4
11	1.2	855	788	6.4
12	.95	912	831	6.4
13	.86	942	872	6.3
14	.74	1024	1008	6.6
15	.65	1110	1136	7.3
16	.50	1473	1467	8.3
17	.44	1661	1615	9.7

The second interim low beta lattice does not utilize any high current trim magnets. At B0, the old low beta magnets are retained, the straight section matching quadrupoles are off or removed, and the 10 nearest tune quadrupoles - 5 per side - are removed from the tune buses and separately powered to approximately match the B0 insertion during injection. At D0, the dipoles are moved, the straight section matching quadrupoles are removed, the new 2-shell low beta quadrupoles (Q1 through Q5) are added, and as at B0, 10 tune quadrupoles are removed from the tune buses to match D0 to the arcs at injection. Because of the inadequate strength of the separately powered tune quadrupoles, the insertions are no longer matched. The beta peaks in the arcs of the accelerator have been kept below 150 m and the dispersion has been kept below 10 m. The gradients for this lattice are given in Table 6.4.3.

Table 6.4.3 SQUEEZE PARAMETERS FOR A MIXED MODE LOW BETA INSERT
INPUT FILE [KOEPKE.TEVATRON]CHEAP.IN
•• ONLY LOW GRADIENT TRIMS ARE USED •• GRADIENTS IN KG/M
T6 THROUGH T10 ARE TRIM MAGNETS IN SPOOLS - MAGNETIC LENGTH 30"

D0 GRADIENTS	Q4	Q3	Q2	Q1	Q5	T6	T7	T8	T9	T10
RAMP150	-1261.4	1442.0	-1436.6	-1.1	1314.20	77.7	37.1	29.0	-77.1	-120.0
						28.0	-72.6	-43.7	-187.2	-34.9
RAMP1000	SAME AS STEP 8									
STEP 1	SAME AS STEP 8									
STEP 2	SAME AS STEP 8									
STEP 3	SAME AS STEP 8									
STEP 4	SAME AS STEP 8									
STEP 5	SAME AS STEP 8									
STEP 6	SAME AS STEP 8									
STEP 7	SAME AS STEP 8									
STEP 8	-1237.7	1426.3	-1439.5	-2.6	1328.90	0.0	0.0	0.0	0.0	-26.0
						0.0	0.0	0.0	0.0	28.0

B0 GRADIENTS

STEP	DJ1	DJ2	DJ3	DJ4	T6	T7	T8	T9	T10	QFC	QDC
RAMP150	-53.5	924.7	-878.2	138.2	334.4	267.1	-50.0	-418.7	-360.8	-11.53	17.88
					-401.6	-231.8	-5.1	506.3	361.1		
RAMP1000	-100.0	877.4	-845.	26.1	59.4	83.6	89.4	-89.8	-37.2	-8.20	12.73
					-89.9	-83.6	-57.4	-90.0	25.4		
STEP 1	-112.7	910.5	-768.5	339.7	85.0	89.7	-7.2	-58.0	-84.4	-10.58	14.57
					-31.8	-89.9	89.0	-89.9	-83.1		
STEP 2	-200.6	926.1	-873.2	647.2	67.9	81.9	86.9	-89.4	-87.5	-13.80	15.27
					6.0	-89.8	82.1	42.0	-79.8		
STEP 3	-289.3	921.8	-912.0	737.4	82.7	80.7	-43.1	13.5	-90.0	-12.69	16.08
					24.8	-86.8	48.0	-89.7	-27.0		
STEP 4	-289.0	916.4	-958.8	904.8	88.9	90.0	88.0	-79.6	-89.4	-14.47	16.54
					4.2	-78.1	89.7	-89.4	-38.2		
STEP 5	-458.0	925.1	-983.5	939.7	90.0	89.0	89.9	-90.0	-26.5	-18.47	20.62
					-90.0	-90.0	-89.9	54.3	76.6		
STEP 6	-758.0	943.7	-993.4	930.0	88.3	89.9	-18.4	-88.9	-90.0	-21.99	24.03
					89.7	-87.9	-32.7	90.0	-4.8		
STEP 7	-875.0	949.4	-996.7	950.2	89.2	90.0	35.8	-89.5	-58.0	-25.30	27.54
					-0.2	-89.0	-61.4	90.0	11.2		
STEP 8	-1000.0	955.1	-1000.0	970.4	90.0	90.0	90.0	-90.0	-26.0	-29.42	31.71
					-90.0	-90.0	-90.0	90.0	28.0		

STEP	BSTAR	BXMAX	BYMAX	ETAMAX	NUX	NUY
RAMP150	39.	286	274	6.6	20.40	20.40
RAMP1000	25.	303	369	9.6	20.40	20.40
STEP 1	18.5	390	345	9.0	20.40	20.40
STEP 2	7.5	451	309	9.1	20.40	20.40
STEP 3	3.6	529	469	9.8	20.40	20.40
STEP 4	1.8	486	443	8.5	20.40	20.40
STEP 5	1.65	518	575	9.3	20.40	20.40
STEP 6	1.2	867	684	8.6	20.40	20.40
STEP 7	.87	988	934	8.5	20.40	20.40
STEP 8	.63	1253	1323	8.9	20.40	20.40

VII. ENERGY DEPOSITION IN THE TEVATRON MAGNETS FROM BEAM LOSSES IN THE INTERACTION REGIONS

1. INTRODUCTION

In addition to interacting in the detector, particles produced at an interaction region also deposit energy, with less desirable consequences, in magnets and other components of the accelerator. This section briefly assesses the damage potential of these (essentially unavoidable) beam losses from the viewpoint of quenching of superconducting magnets in an upgraded Tevatron with a luminosity of 10^{31} $cm^{-2}sec^{-1}$ though the results carry more generality. Related issues such as radiation damage to detector electronics or other components are not addressed here. These are thought to be less problematic at the Tevatron, as is thus far supported by operational experience. A similar (and actually more serious) situation is encountered in fixed target mode during resonant extraction where unavoidable losses occur when a small fraction of the beam strikes the wires of the electrostatic septum. A detailed analysis, based on reasonably realistic Monte Carlo simulations of these losses, exists[1] and this section relies heavily on that study.

Elastic or quasi-elastic scattered protons are characterized by small energy losses and small angles,[2] which permits them to travel with the beam for considerable distances, though a significant fraction is lost eventually at one or more aperture limiting locations. These losses therefore tend to be more concentrated than the inelastic kind.This is further enhanced because, even at the loss point, the elastics still very much resemble a 'beam' which intercepts the beampipe in the midplane with a relatively narrow vertical spread. Quenches in the Tevatron from beam loss due to elastics have been observed and compared with results of simulations. While agreement can only be claimed to be semi-quantitative, this is reasonable in view of a very strong sensitivity to geometric factors such as magnet alignment and position of the closed orbit.

The problem of losses from collisions in the interaction regions can likewise be split into elastic and inelastic parts with p-$\bar{p}$ collisions replacing the interactions of protons with tungsten nuclei (and electrons) in the septum. The elastics can be further divided into (a) multiple Coulomb scattering, summed over repeated beam crossings, and (b) particles having participated in (nuclear) elastic or single diffractive events. The multiple scattering part is treated as a contribution to (slow) transverse beam growth rather than as a beam loss. It is included in this discussion because of its close relationship to the other physical mechanisms. Interference between Coulomb and nuclear scattering is neglected.

2. INELASTICS

One potential hazard associated with inelastics is quenches in the string of high beta quadrupoles which is positioned close to the center of the interaction region, without the benefit of any shielding. Of lesser concern are neutral particles which travel unimpeded from the interaction region until intercepted by the out-side of the beampipe-wall ~7 m into the first dipole string. Both cases are Monte Carlo analyzed using an approximate geometry. The neutrals simulation also affords a look at the energy deposition by leading particles.

The inelastic collisions are assumed to take place head on and at the exact center since the x,y-extent of the interaction region is small compared to the beampipe radius and the z-extent is small compared to the distance to the magnets. This assumption also results in a more concentrated energy deposition in the magnets thereby providing useful uppper limits. Simulation of 1 TeV on 1 TeV collisions relies on a simple parametrization of Monte Carlo results of the program DTUJET specifically for this energy.[5] Particle interactions and transport in beampipe, iron ring, and magnets is simulated by CASIM.[4]

a. High Beta Quadrupoles

Simulation of the problem of the high beta quadrupoles incorporates the overall geometry shown in Fig. 7.2.1, with the quadrupoles as in Fig 7.2.2. A lot of detail is omitted: flanges, valves, detector components, etc. As a test of the sensitivity to the presence of such objects a 10 cm thick ring of iron is optionally added in the position indicated in Fig. 7.2.1. The **B** field is taken to be 1.4 Tesla/cm and, in order from center, the polarity of the quads is (horizontal) D-F-D for positive particles.

Energy deposition is recorded in the magnet coils ($3.81 \leq r \leq 5.874$ cm, see Fig. 7.2.2) in ring-shaped bins with Δr varying from 0.29 cm (small r) to 0.574 cm, and Δz from 2.7 cm (small z of first quad) to 175 cm. Azimuthal binning is rather course: the region $0 < \phi < \pi/4$, as measured in a positive or negative sense from either horizontal or vertical, is divided equally in three parts. This binning is based on the observation that an 8-fold symmetry applies if one assumes identical populations of positive and negative particles in phase space at production, which is not exact but reasonably close. The main exception is that, among energetic (including leading) particles, positives will be more prevalent on the p-side and negatives on the $\bar{p}$-side, but most of these will traverse the high beta quads within the aperture.

The calculated energy deposition, for a luminosity of 10^{31} cm^{-2} s^{-1},as a function of distance along the quad string in the sampling region of the coils located innermost radially and containing the midplane azimuthally, is shown in Fig. 7.2.3 for a bare beampipe. It appears that adding 10 cm of iron does make a difference at shallow depth in the first quad. This is illustrated in Fig. 7.2.4a where the radial distribution in the slice $0 < z < 2.7$ cm, averaged over azimuth, is compared for the two cases. However, the difference in energy deposition disappears quickly with depth into the quad, as shown in Fig. 7.2.4b for the $7.7 < z < 12.7$ cm region. This suggests that even a relatively thin (~10 cm) collimator, placed directly in front of the first quad, could absorb the excess. The magnitude of the energy densities, approaching 0.03 GeV/(cm^3•inelastic event) for the bare beampipe and 0.1 GeV/(cm^3•inelastic event) with the iron present, are not cause for alarm. To recast these numbers in terms of a quenching limit one can ask for the luminosity needed to attain the nominal 8 mW/g from the Tevatron Design Report.[5] For 0.1 GeV/(cm^3•inelastic event) and assuming $\sigma_{inel} = 80$ mb this corresponds to $5 \cdot 10^{34}$ $cm^{-2}sec^{-1}$. It should also be recalled that for fast extraction losses observed quench limits are somewhat higher than expected from the Design Report (by a factor of ~1.7, though with significant statistical error).

b. Neutrals

The geometry used for simulating energy deposition due to neutrals is shown in Fig. 7.2.5. For simplicity the high beta quads are omitted and the dipole string is represented as a continuous magnet with a 754 m bending radius and **B** field to accomodate 1 TeV protons. The assumed dipole cross section is as in Fig. 7.2.6. All material beyond the iron cylinders (representing the stainless steel collars) is neglected since particles observed at these large radii are unlikely to contribute to the energy deposition at small radii in the coils. Only particles which enter the dipole string within the vacuum chamber are included in the analysis. (For particles striking the front of the first dipole the geometry of Fig. 7.2.5 is quite unrealistic.) Energy deposition is recorded in the magnet coils ($3.81 < r < 5.458$ cm) divided radially into three tori, as well as in the vacuum chamber which is 0.154 cm thick and is in the shape of a 'rounded square'. It is easy to imagine this peculiar shape to affect the energy deposition and therefore it is faithfully represented in the simulation. The recording bins are azimuthally subdivided into seven unequal wedges with two small regions ($\Delta\phi = 0.2$) centered on the midplane: on the out-side of the vacuum chamber wall for the purpose of recording the neutrals and on the in-side for leading particles. The up-down symmetry of this problem is exploited in the ϕ-binning. Less variation is expected along the z-direction and the bins are sliced into large Δz (100 to 200 cm). To help determine the true maximum energy density in the coils,

rather than an average over some volume bin, the radial energy variation is fitted to an *a priori* selected function (see Ref. 1, further fitting to functions of ϕ and z is not attempted here).

Fig. 7.2.7 presents the variation of the maximum energy density in the regions $0 < |\phi| < 0.3$ and $(\pi - 0.3) < |\phi| < \pi$ as a function of z. These regions include the smaller $\Delta|\phi| = 0.1$ bins (about zero and π) which do not show significantly higher energy densities but are statistically noisy. The neutrals peak is indeed observed and is about $2.5 \cdot 10^{-3}$ GeV/cm^3•collision at the maximum. Also from Fig. 7.2.7 it can be seen that on the in-side of the dipole (which includes the leading particle contribution) the maximum energy density is about $4.0 \cdot 10^{-4}$ GeV/cm^3•collision. Both these numbers are well below the corresponding value for the high beta quads.

3. ELASTICS

Quenching appears even less probable due to energy deposition by elastics than by the inelastics from comparison with the fast extraction problem. Located much closer to the particle source, and without a protective dogleg, the high beta quads do not appear to be vulnerable at design luminosity. Under similar circumstances in the resonant extraction problem, inelastics would definitely be expected to produce the larger energy densities. The relative number of elastic and inelastic beam losses also favor this conclusion: of all protons intercepting the septum (for typical operation of the Tevatron during extraction) about equal numbers are lost elastically (18.7%) as inelastically (22.9%).[1] (The remainder, mostly particles which suffered only minimal energy loss and scattering in the septum, is extracted in less than three turns.) By comparison for colliding beams $\sigma_{inel} = 80$ mb, $\sigma_{el} = 18$ mb and, for single diffraction, $\sigma_{sd} = 8.5$ mb (per beam, as per usual definition) are working numbers based on extrapolation. Also the collisions take place essentially in the center of mass so that, at least for the pure elastic part, the particles change direction but change their energy very little. In contrast, even purely elastic interactions in the septum are always accompanied by some energy losses of which ionization losses in the tungsten wires is the most significant. There are nevertheless noticeable dissimilarities with the extraction problem. For example, the high beta quads themselves pose severe aperture limitations raising the possibility that the elastics deposit their energy on top of the inelastic component, estimated above. Moreover, one set of high beta quads could collect elastics from more than one interaction region and from both p and $\bar{p}$ elastics. Since the quads are situated essentially within the detector, such a scenario is likely to be intolerable for many experiments even well below quench threshold and to necessitate, e.g., collimators to be installed. This facet of the problem depends strongly on the experiment being performed and is not further addressed here.

Below it is attempted to delimit the maximum energy deposition by the elastics from inspection of the phase space immediately after scattering. Tracking particles through the lattice and simulating their interactions at a loss point, as in Ref. 1, is not attempted. The three largest contributions to the elastic part are Coulomb scattering, nuclear (hadronic) elastic scattering, and single diffractive particle production wherein one particle becomes a state of low invariant mass while its collision partner (recoil) continues with only small changes in energy and direction.

For the initial phase space of the 900 GeV/c colliding beams it is assumed that $\sigma_y = \sigma_T = 0.032$ mm, $\sigma_x = [\sigma_T^2+\eta^2(\Delta p/p)^2]^{1/2}$ with $\eta = 150$ mm and $\Delta p/p = 1.5 \cdot 10^{-4}$. Distributions of x' and y' are derived using the lattice parameters at the interaction region $\alpha_x = 0.0007$, $\alpha_y = 0.016$, and $\beta_x = \beta_y = 0.5$ m. The x and y coordinates of the collision (x_c, y_c) are normally distributed. Since for the beams, $\sigma_{y,p} = \sigma_{y,\bar{p}}$ (independent of momentum) it follows that $\sigma_{y,c} = \sigma_{y,p}/\sqrt{2}$. For the x coordinate this must be modified since the momentum will differ for p and pbar, and $\sigma^2_{x,c} = \sigma^2_{x,p}\sigma^2_{x,\bar{p}} /(\sigma^2_{x,p} + \sigma^2_{x,\bar{p}})$. Given x_c, the combination $\alpha_x x + \beta_x x'$ is chosen from a Gaussian with $\sigma = \sigma_T$ from which x' follows (ditto for y'). Somewhat arbitrarily (see below) all the Gaussians of the incident distributions are truncated at 3.5σ.

a. Nuclear Elastic

To simulate the phase space population of the final states of nuclear elastic scattering, the dependence of the cross section on t, the square of the four-momentum transfer, is assumed to follow:

$$\begin{aligned} d\sigma/dt &= A \cdot \exp(16.8t) && 0 \le |t| < 0.63 \\ &= B && 0.63 \le |t| < 0.86 \\ &= C \cdot \exp(3.1t) && 0.86 \le |t| \end{aligned}$$

where A, B, and C are constants fixed by continuity and normalization and t is expressed in $(GeV/c)^2$. This is a parametrization of a theoretical prediction of Gauron et al[6] whose results at lower energy agree quite well with the data. Since selection from the above distribution is very fast no biasing has been applied. Momenta and directions of the final state particles are determined using full kinematics.

As an indication of beam losses, particles scattered into the 'wings' of the phase space are considered lost (after some distance, possibly multiple turns) if $(\alpha_x x+\beta_x x')$ or $(\alpha_y y+\beta_y y')$ falls outside of 5σ. This condition prompted the aforementioned 3.5σ cut on the incident phase space since otherwise even some unscattered incident particles would already qualify as being lost. Fortunately, the scattered phase space is not very sensitive to the precise value

of the cut on the incident phase space. Because of the proximity of lab and center-of-mass system, no events with $\Delta p/p$ large enough to be 'lost' are encountered. Obviously, there are no cuts to apply on x and y since these are unchanged in the scattering process. Fig. 7.3.1 shows the fraction of particles outside a given limit in $(\alpha_x x+\beta_x x')$ and $(\alpha_y y+\beta_y y')$ as a function of that limit, expressed in units of the corresponding σ of the beam. It is separately indicated whether $(\alpha_x x+\beta_x x')$ or $(\alpha_y y+\beta_y y')$ exceeds the limit (where both qualify the event is sorted with the larger of the two). The fraction of particles outside the 5σ limit is found to be 0.18.

From Ref. 1, a fast loss of $\sim 7 \cdot 10^8$ (elastically scattered) protons striking the last quadrupole at the F49 location suffices to cause it to quench. Scaling this to a corresponding number for continuous operation by the ratio of the nominal design limits[5] for fast and slow losses ($8\ mW \cdot g^{-1}/1\ mJ \cdot g^{-1}$) means that $\sim 6 \cdot 10^9$ p/sec will induce a quench. However, for a luminosity of $L = 10^{31}\ cm^{-2}sec^{-1}$, $\sigma_{el} = 18$ mb, and for 0.18 of the elastics outside of the emittance, only $3.2 \cdot 10^4$ protons per second (and per beam) will be lost ring-wide. For a worst case scenario it should be assumed that all these particles are lost at one location and this could further be multiplied by a factor of four given two interaction regions and since p as well as $\bar{p}$ elastics can, in principle, contribute. Even this scenario leaves an ample margin of safety and the conclusion that, from the viewpoint of magnet quenching, elastics are unlikely to cause any problems. The dependence on the 'loss-limit' of the outgoing phase space, shown in Fig. 7.3.1 and somewhat arbitrarily set at 5σ, is not so strong that lowering this limit to 4σ, or even 3.5σ, would alter the conclusion. The scaling procedure above ignores differences in the phase space at production between elastics from p-$\bar{p}$ versus those from the septum as well as possible geometric factors arising at the loss point from striking different magnets in different locations. However, these differences are very unlikely to overcome the large difference in the numbers of elastics generated in each mode of operation.

b. Diffractive

The phase space produced by single diffractive recoils is obtained using a parametrization of the cross section, $d\sigma/dtdM^2$, taken from the review of Goulianos.[7] The more detailed algorithm may be found in Ref. 2. Again the full kinematics is applied to derive the parameters of the final state particle. Fig. 7.3.2 presents contours of equal particle density in Δp,y'-space, illustrating the importance of momentum losses in this case. Fig. 7.3.3 shows the fraction of particles outside each and any of the $(\alpha_x x+\beta_x x')$, $(\alpha_y y+\beta_y y')$ and Δp limits as a function of the limits expressed in units of the corresponding σ of the incident beam. About 0.66 of the total are outside the 5σ limit, mostly due to momentum losses. From the large Δp encountered here it appears that many of these particles will be lost relatively quickly from the aperture thereby diminishing the likelihood that all are lost at the same location.

The argument, made above for the elastics, can be repeated here to demonstrate that single diffractive losses are also expected to be entirely tolerable. For $L = 10^{31}$ cm^{-2}sec^{-1}, $\sigma_{sd} = 8.5$ mb, and for 0.66 of the elastics outside the emittance $5.6 \cdot 10^4$ protons per second (and per beam) will be lost. Hence no quenching problems are expected even if the combined inelastic, scattering, and diffractive losses from two interaction regions all were to accumulate in one particlular loss location.

c. Multiple Scattering

Multiple Coulomb scattering incurred during multiple encounters of a particle with members of the opposite beam and summed over multiple turns contributes to a slow growth in beam emittance. While this will also lead to slow losses these are presumably small and not assessed here. The growth in beam emittance, from this and other mechanisms, will shorten the useful beam lifetime. Below a brief derivation of the emittance growth is presented and numerically evaluated for beam parameters as listed above for the other elastic mechanisms.

The cross section for Coulomb scattering, $d\sigma/d\Omega \simeq (2\alpha/p\theta^2)^2$, evaluated at 900 GeV and integrated over angle becomes $\sigma_C \simeq 3.1 \cdot 10^{-10}\theta_{min}^{-2}$ mb, while the mean square angle per scattering is $\langle\theta^2\rangle \simeq 2\theta_{min}^2 \ln(\theta_{max}/\theta_{min})$, with θ_{min}, θ_{max} to be determined below. For two Gaussian beams colliding head on the average number of such collisions per crossing, experienced by each particle, is $N_b\sigma_C/4\pi\sigma_x\sigma_y$, where N_b is the number of particles per bunch, and the mean square angle per crossing (at 900 GeV) is $5.0 \cdot 10^{-36} N_b \ln(\theta_{max}/\theta_{min})/\sigma_x\sigma_y$, with σ_x, σ_y in mm. In view of the log dependence, the derivation of θ_{min}, θ_{max} can be quite sketchy. θ_{min} is obtained by equating $\sigma_C \simeq \pi b^2$ where b is the maximum impact parameter. To estimate b it is assumed the N_b particles are uniformly distributed in a $(2\sigma_x)\times(2\sigma_y)\times(2\sigma_z)$ box, which results in a distance between neighbors of $(8\sigma_x\sigma_y\sigma_z/N_b)^{1/3}$. The half-distance, projected onto the (x, y) plane is a reasonable estimate of b. For σ_x, σ_y as above and for $\sigma_z \simeq 350$ mm this yields $\theta_{min} \simeq 2.1 \cdot 10^{-14}$. The angle θ_{max} can be chosen as the angle where nuclear and Coulomb scattering are equal which, at 900 GeV, means $\theta_{max} \simeq 3 \cdot 10^{-5}$. This is still below rms beam angles and, while Coulomb scattering with $\theta \simeq \theta_{max}$ is expected to be relatively rare, the condition $\theta < \langle\theta^2\rangle^{1/2}$ allows for treating such angles as contributing to beam spreading. With $N_b = 7.4 \cdot 10^{10}$ these numbers combine to yield $\langle\theta^2\rangle \simeq 6.0 \cdot 10^{-21}$ per crossing. If one assumes only two interaction regions contribute, i.e., that the beams are separated elsewhere, then this translates directly into an (instantaneous) rms growth in projected angle of 5 μr per day for each θ_x and θ_y. For $\beta_x = \beta_y = 500$ mm, σ_x and σ_y are expected to grow 2.5 μm per day, which is not negligible but well below the growth rate, e.g., from intrabeam scattering.

d. Intermediate Angles

To complete the discussion one should mention beam growth from individual scattering events which fail to expel the particle from the beam ($\theta < \sim 5\sigma$, in the simplistic model used here). For nuclear scattering the fraction remaining within 5σ is estimated at 0.82 for a cross section of 14.8 mb and with an rms angle of $2.1 \cdot 10^{-4}$. For the diffractive component the corresponding cross section is about 2.9 mb and the rms angle is $1.8 \cdot 10^{-4}$. For the Coulomb part the multiple scattering regime ($\theta < \theta_{max}$) must be excluded. The total cross section for the remainder is about 0.35 mb with an rms angle of $5.4 \cdot 10^{-5}$. For all combined, events at these intermediate angles accumulate at a rate of ~3% of the beam per day.

4. CONCLUSIONS

In summary, it has been shown that energy deposition in the Tevatron superconducting magnets due to particle production and elastic processes in the interaction regions is unlikely to cause any quenching even at luminosities much higher than the design value of 10^{31} $cm^{-2}sec^{-1}$. The products of inelastic interactions which strike the nearby high beta quads provide the worst scenario in this respect but are not expected to induce a quench unless the luminosity were higher by a factor of ~5000. The peak energy density for the neutral 'beam' striking the dipoles is down further by a factor of 40 to that observed in the high beta quads. For the leading particle contribution the corresponding factor is 250.

Elastically scattered particles are analyzed both in terms of losses and of a slow beam growth (2.5 μm/day at the interaction region). While detailed calculations of the energy deposition are not performed here, a comparison with earlier such calculations, performed in connection with fast extraction losses, plus the 'worst case' assumption that all elastic losses occur on the same magnet, lead again to a margin of safety of ~5000. However, aside from quenching considerations, a significant loss of the elastics on the high beta quads could be unacceptable to nearby experiments at much lower luminosties. The separation of the elastically scattered particles into beam growth, and beam loss, while not entirely realistic, has the virtue of convenience and avoids double counting.

REFERENCES

[1] A. Van Ginneken, D. Edwards, and M. Harrison, Quenching Induced by Beam Loss at the Tevatron, in High Energy Hadron Colliders, A. Chao, H. Edwards, and M. Month, Eds., American Institute of Physics, New York (1987).

[2] A. Van Ginneken, Phys. Rev. D **37**, 3292 (1988).

[3] J. Ranft et al, SSC-Report SSC-149 (1987).

[4] A. Van Ginneken, Fermilab Report FN-272 (1975).

[5] Report on the Design of the FNAL Superconducting Accelerator, F. T. Cole et al, Eds., Fermilab (1979).

[6] P. Gauron, B. Nicolescu and E. Leader, Phys. Rev. Lett. **54**, 2656 (1985).

[7] K. Goulianos, Phys. Rep. **101**, 169 (1983).

FIGURE CAPTIONS

Fig. 7.2.1. Overall geometry of interaction region, with high betas quads, as represented in simulation of inelastic interactions.

Fig. 7.2.2. Cross section of quadrupole magnet as represented in simulation. All dimensions are in cm.

Fig. 7.2.3. Energy density in innermost radial region of coils ($3.81 < r < 4.1$ cm) and in azimuthal regions ($0 < |\phi| < \pi/12$) and ($11\pi/12 < |\phi| < \pi$) as a function of distance along the quadrupole string.

Fig. 7.2.4 Energy density as a function of radius at shallow depth in superconducting coils of first quad for a bare beampipe between interaction region and first quad (solid) and with 10 cm extra iron present (dashed) (a) at the beginning of the quad $0 < z < 2.7$ cm, and (b) some 10 cm into the quad ($7.7 < z < 12.7$ cm). The energy density is averaged over ϕ.

Fig. 7.2.5 Schematic geometry (not to scale) to study effects of neutrals and leading particles in dipoles.

Fig. 7.2.6 Cross section of dipole magnet as represented in simulation. All dimensions are in cm.

Fig. 7.2.7 Estimated maximum energy density in superconducting coil of dipole magnet as a function of z (a) for $0 < |\phi| < 0.3$, or in-side of ring, where leading particles are expected to strike (dashed) and (b) for $\pi - 0.3 < |\phi| < \pi$, or out-side, where neutrals are intercepted (solid).

Fig. 7.3.1 Fraction of elastically scattered particles outside each of the $(\alpha_x x+\beta_x x')$, $(\alpha_y y+\beta_y y')$ limits and fraction outside either limit (labeled TOTAL) as a function of the limits expressed in units of the corresponding σ of the incident beam.

Fig. 7.3.2 Iso-density contours in y',Δp-space of single diffractive recoils.

Fig. 7.3.3 Fraction of diffractive recoils outside each of the $(\alpha_x x+\beta_x x')$, $(\alpha_y y+\beta_y y')$ and Δp limits, and fraction outside any limit (labeled TOTAL) as a function of the limits expressed in units of the corresponding σ of the incident beam.

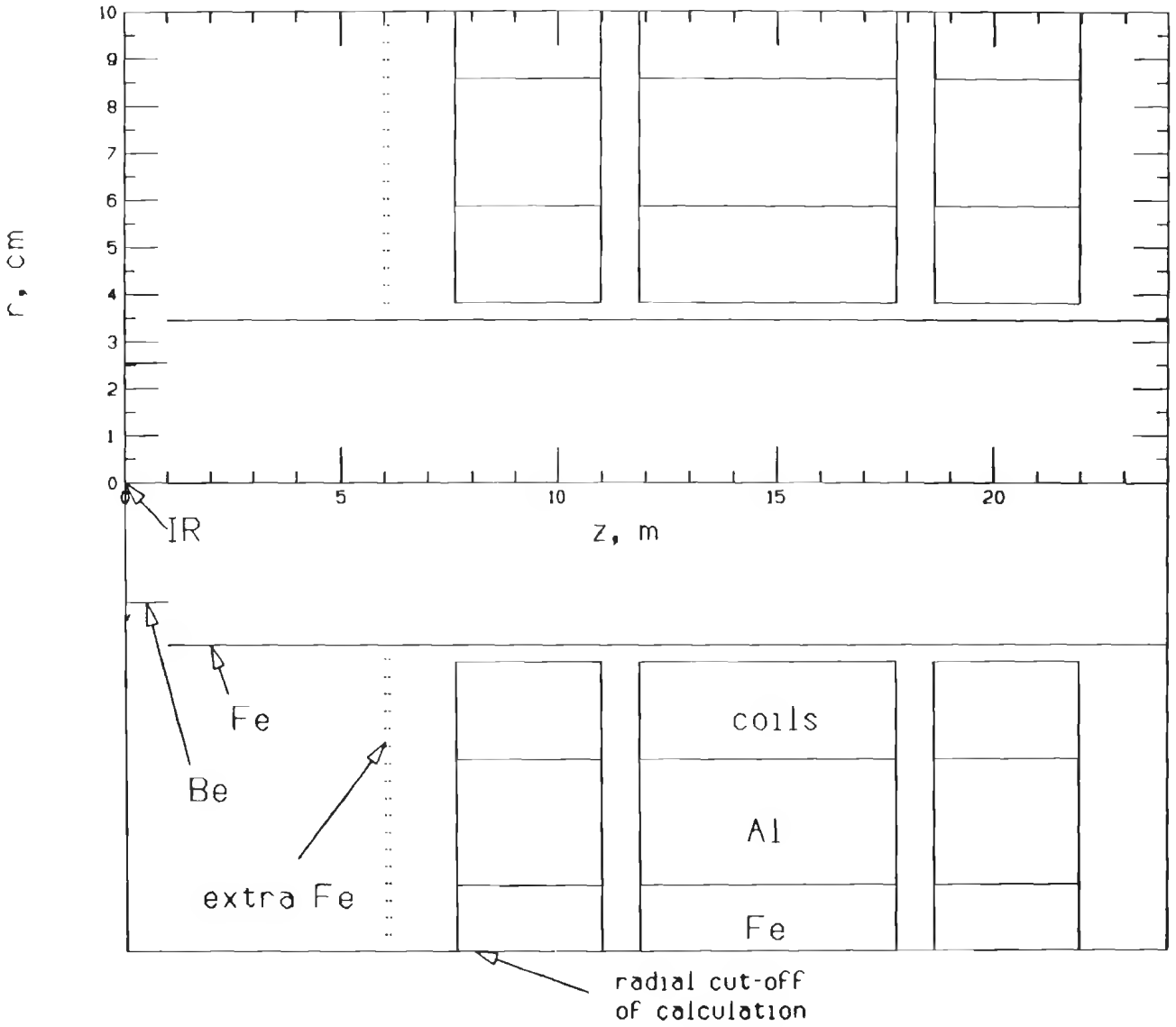
r, cm
z, m
IR
Fe
Be
extra Fe
coils
Al
Fe
radial cut-off
of calculation

Figure 7.2.1

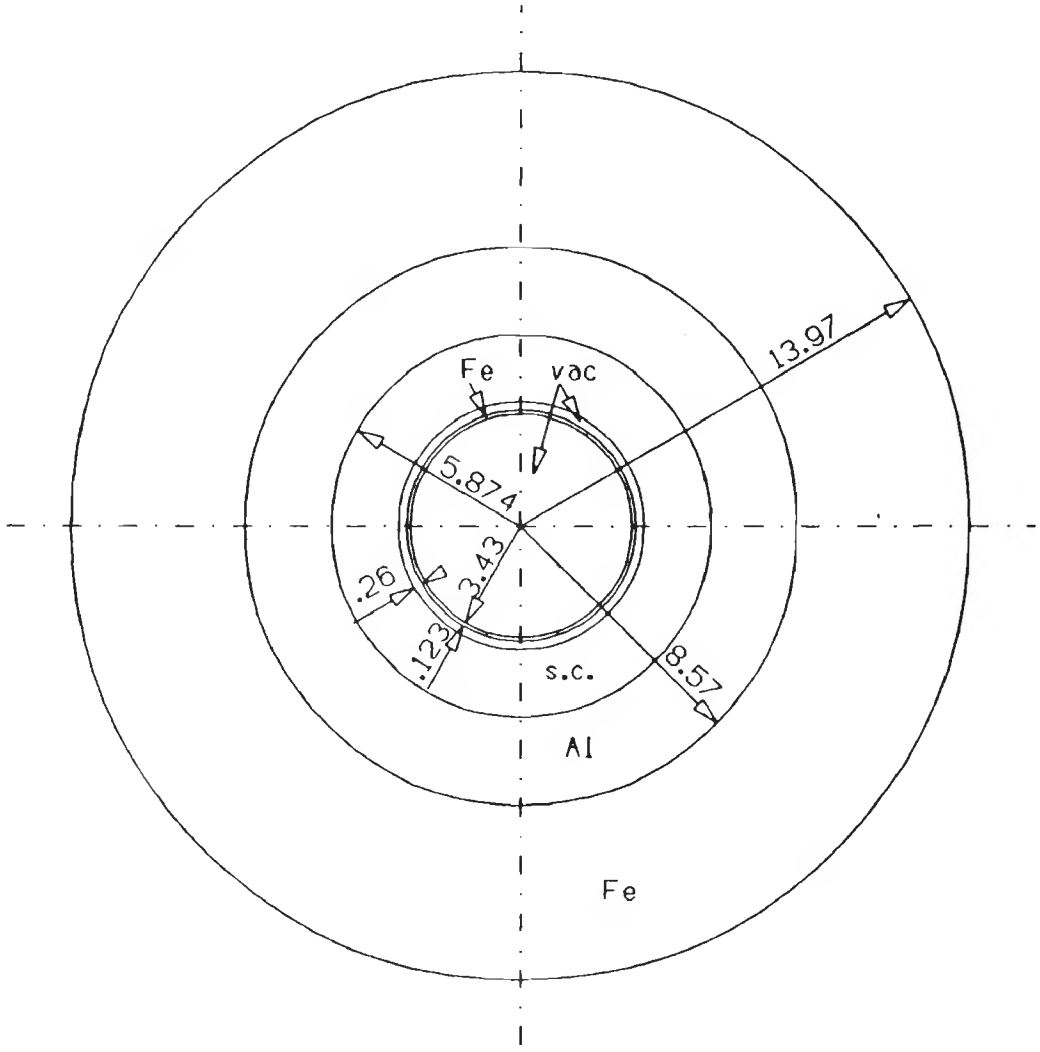

Figure 7.2.2

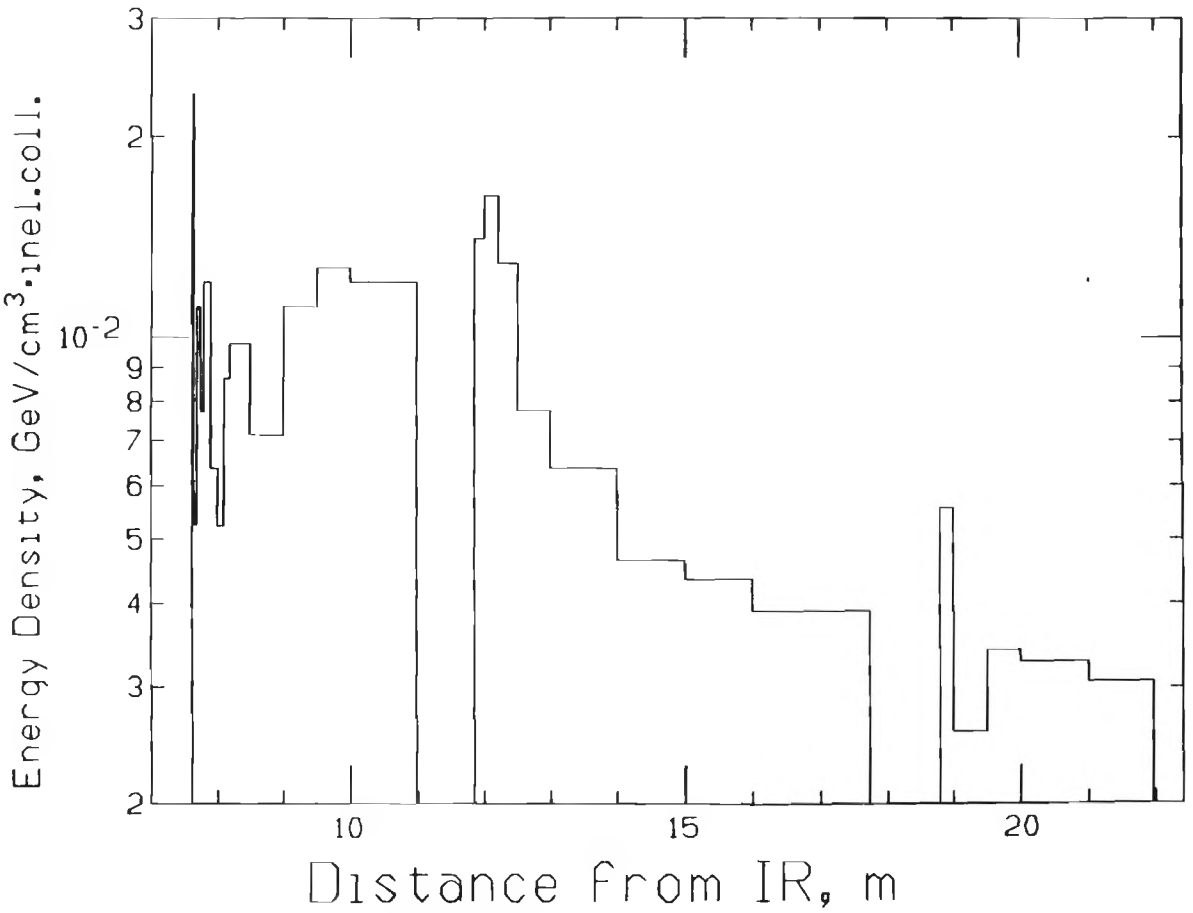
Energy Density, GeV/cm^3·inel.coll.
10^{-2}
3
2
9
8
7
6
5
4
3
2
10
15
20
Distance from IR, m

Figure 7.2.3

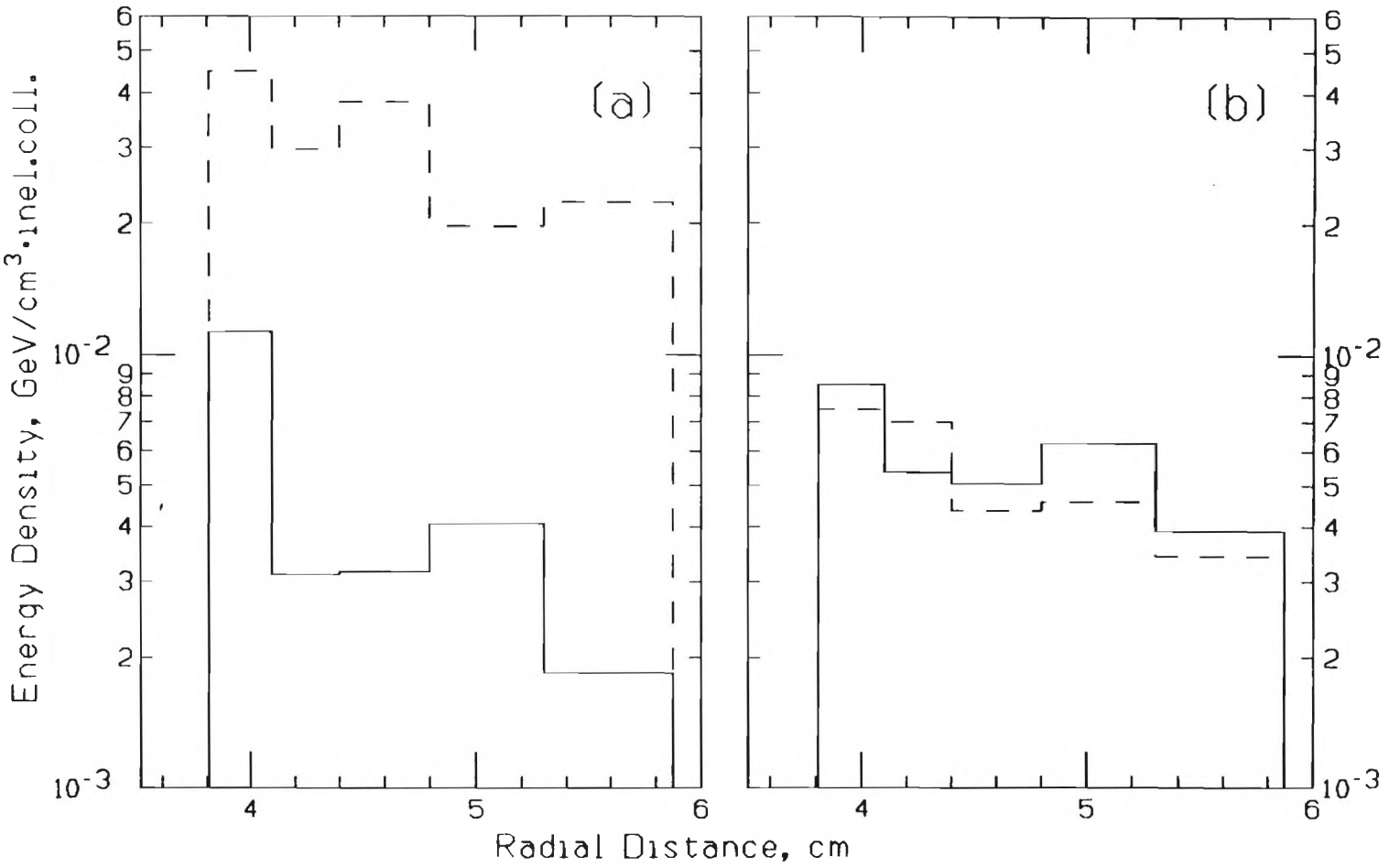
(a)
(b)
Energy Density, GeV/cm^3.inel.coll.
Radial Distance, cm
10^{-2}
10^{-3}
4
5
6

Figure 7.2.4

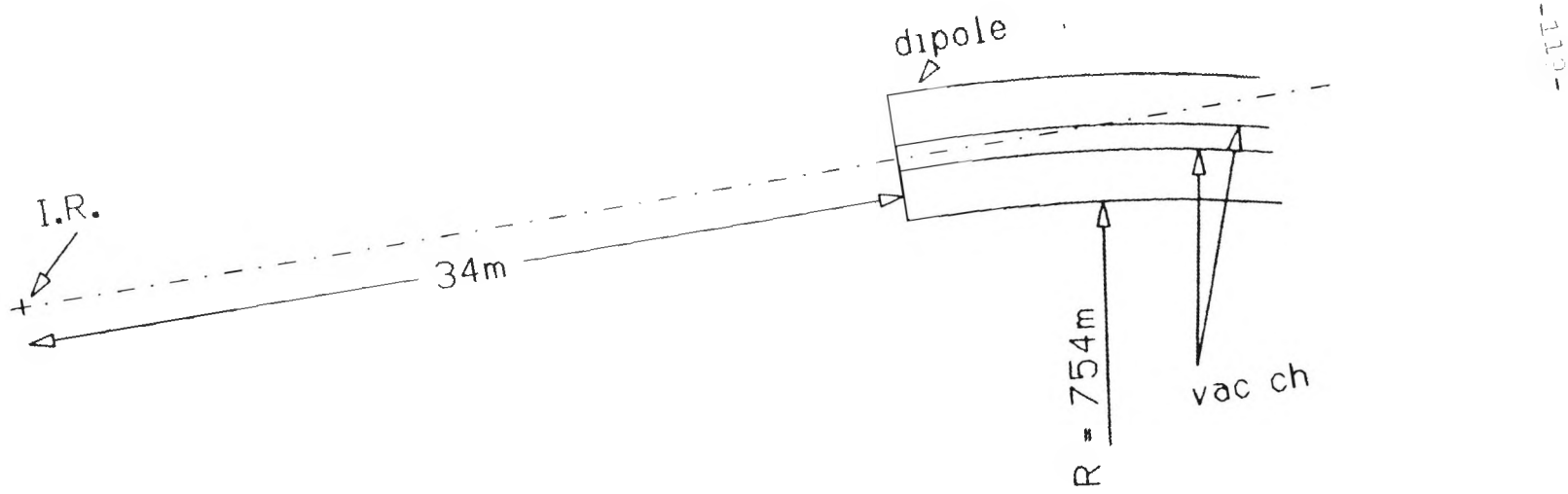

Figure 7.2.5

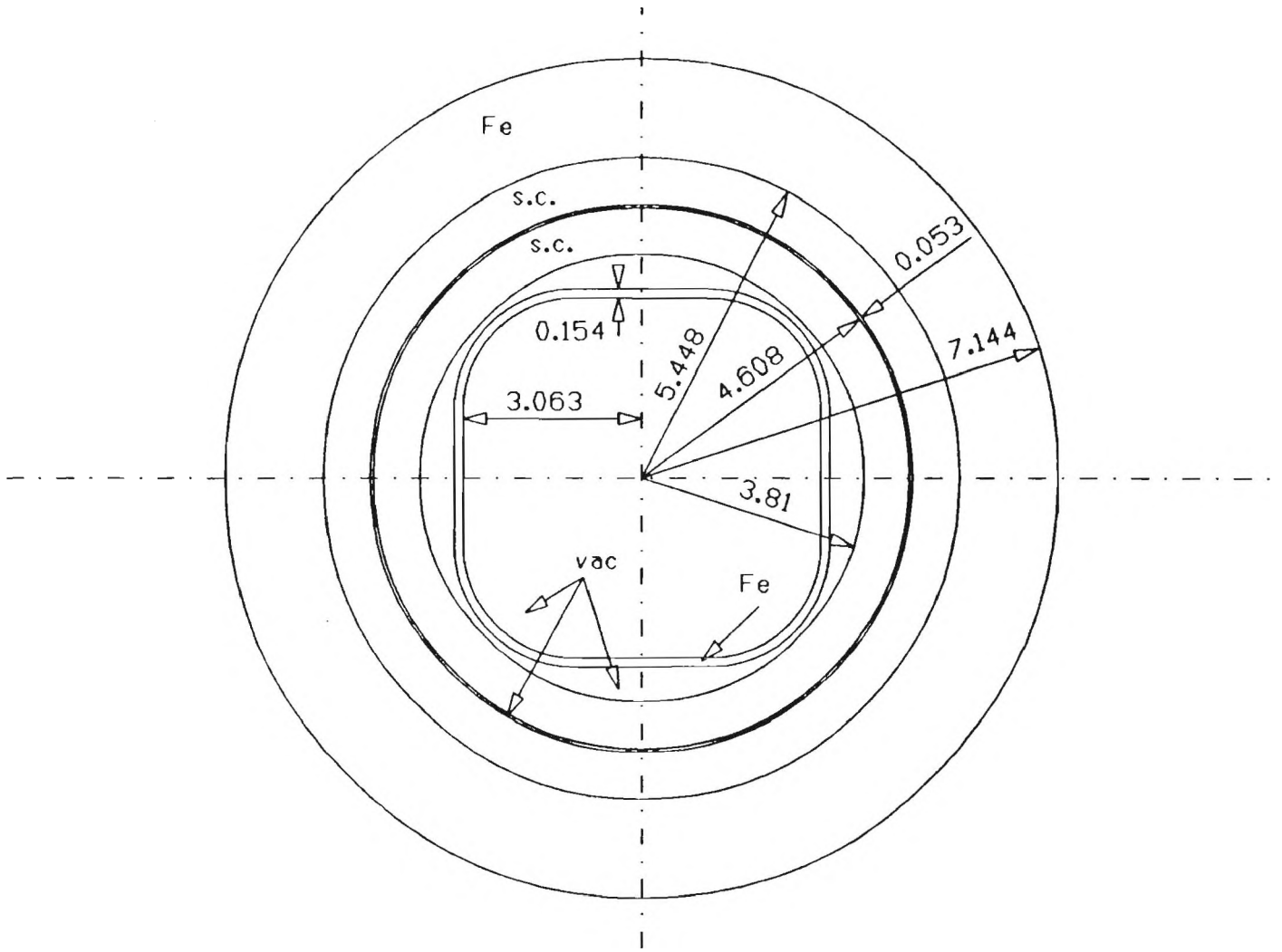

Figure 7.2.6

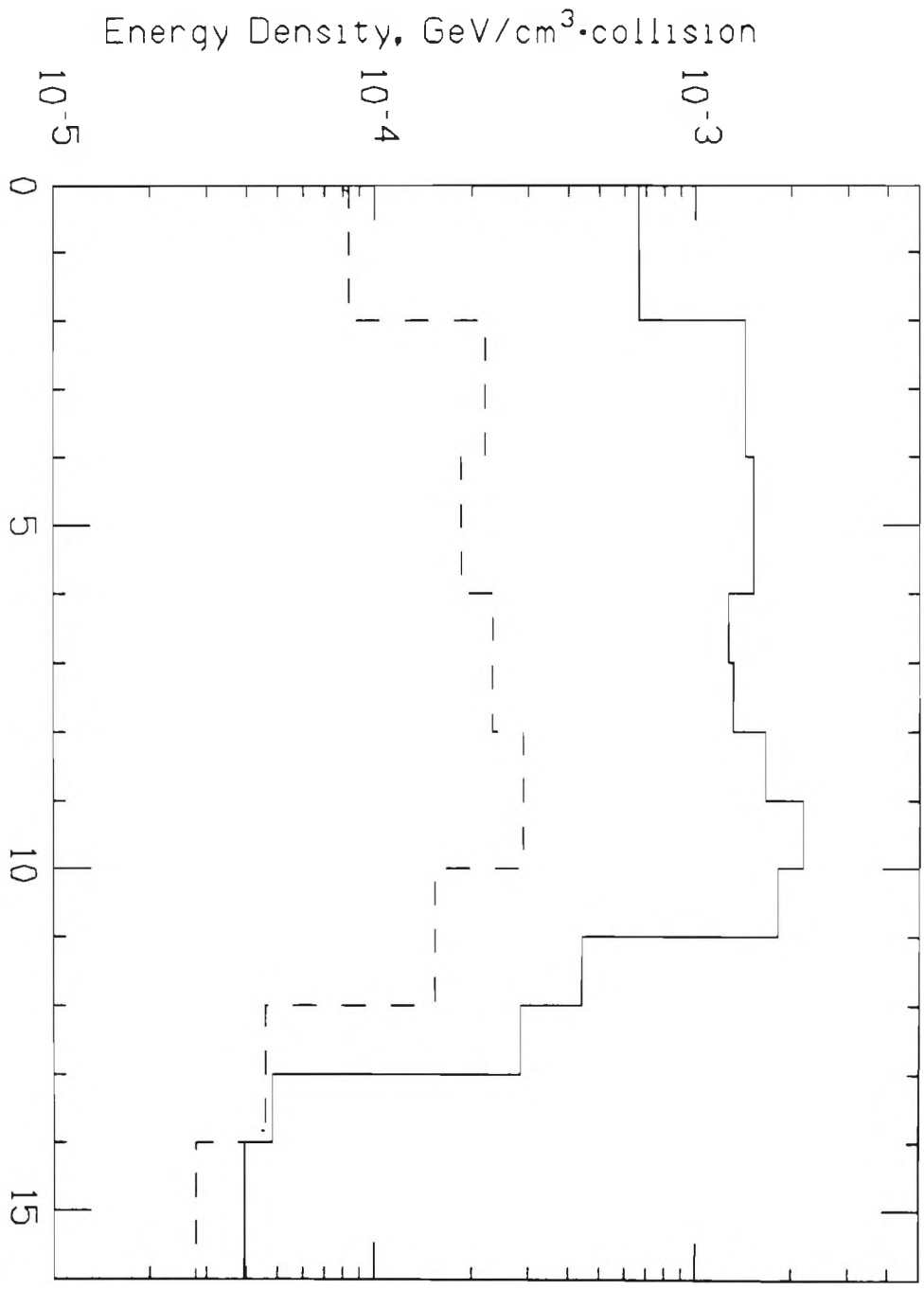
Energy Density, GeV/cm^3·collision
10^{-5}
10^{-4}
10^{-3}
0
5
10
15
Distance, m

Figure 7.2.7

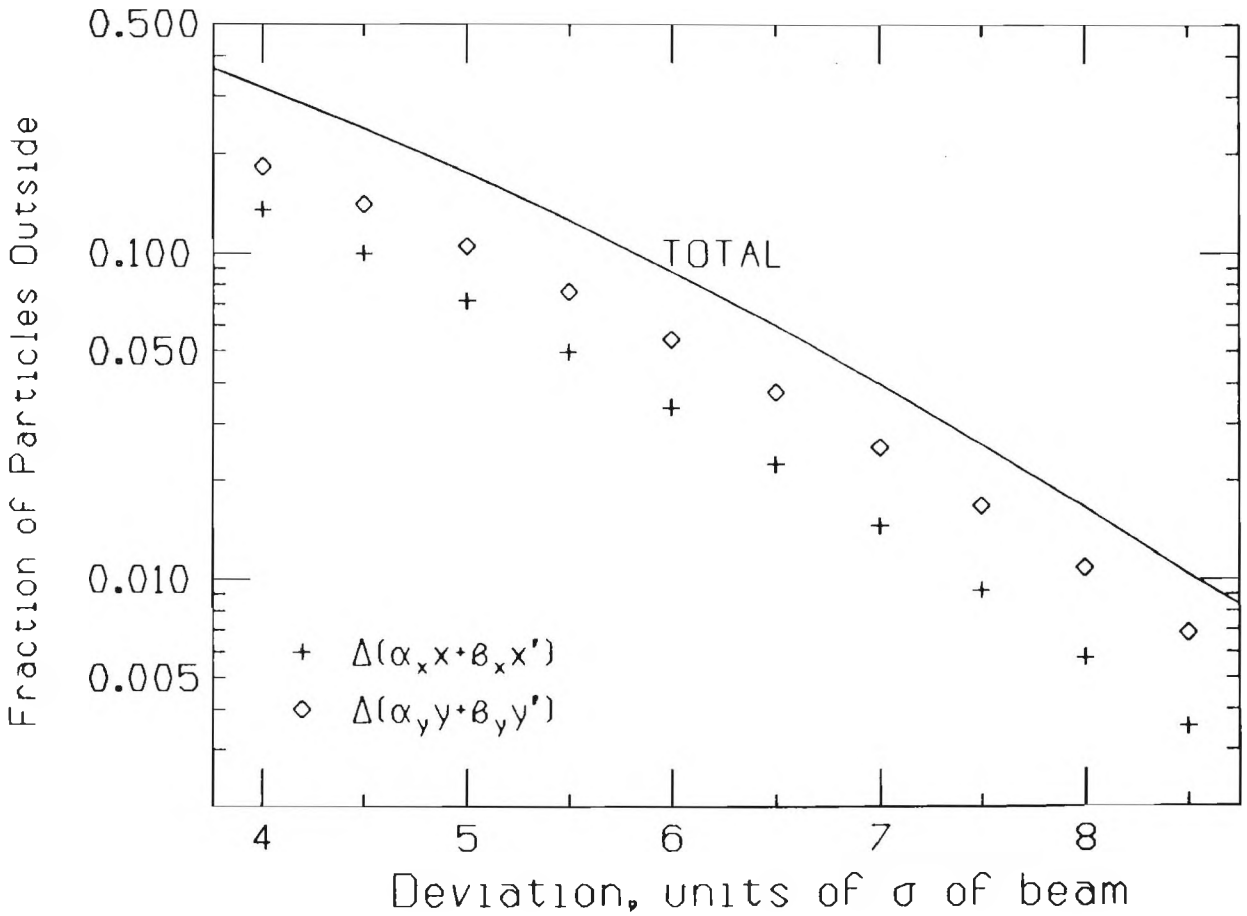
0.500
0.100
0.050
0.010
0.005
Fraction of Particles Outside
TOTAL
+ Δ(αxx+βxx')
◇ Δ(αyy+βyy')
4
5
6
7
8
Deviation, units of σ of beam

Figure 7.3.1

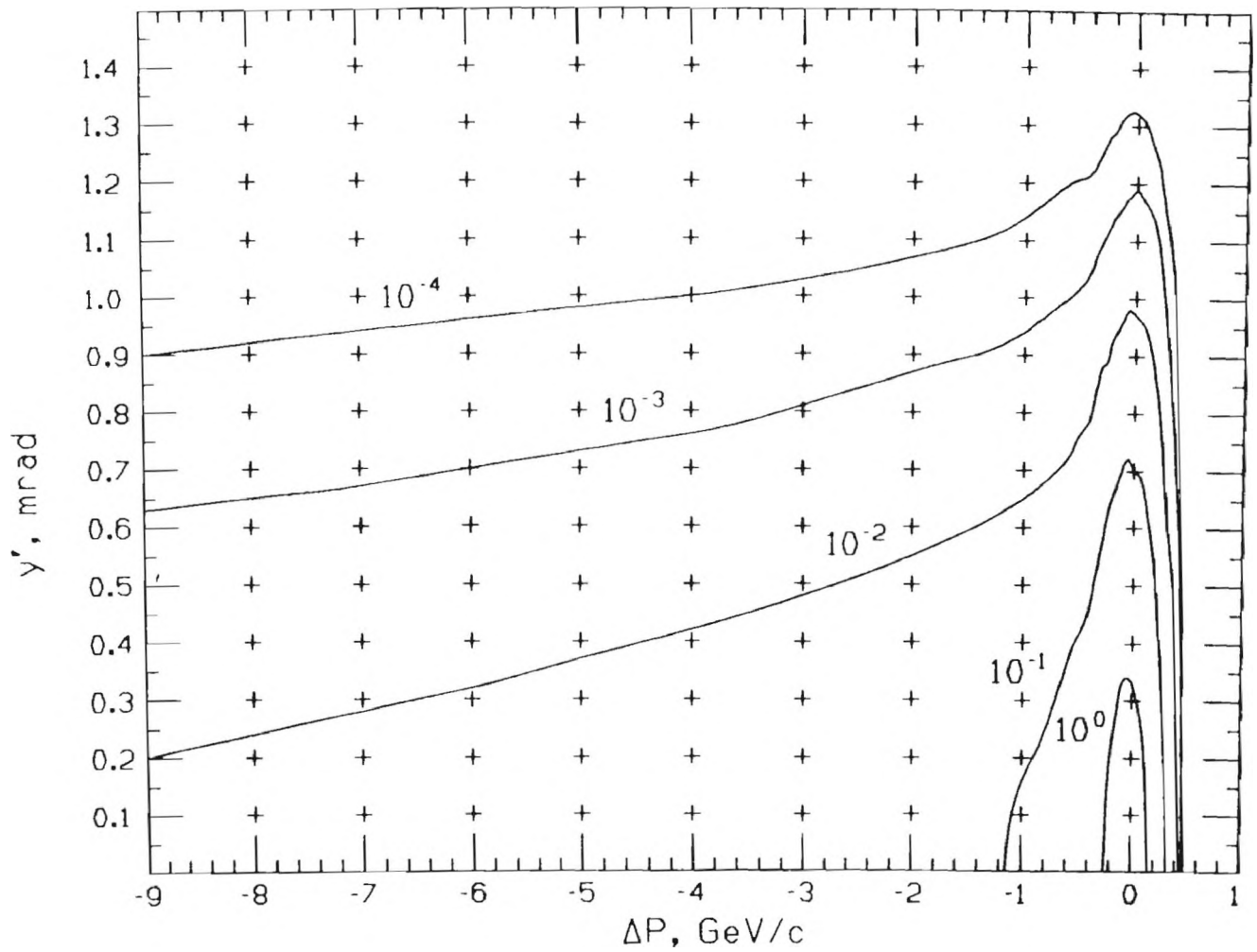
y', mrad
ΔP, GeV/c
1.4
1.3
1.2
1.1
1.0
0.9
0.8
0.7
0.6
0.5
0.4
0.3
0.2
0.1
-9
-8
-7
-6
-5
-4
-3
-2
-1
0
1
10^{-4}
10^{-3}
10^{-2}
10^{-1}
10^{0}

Figure 7.3.2

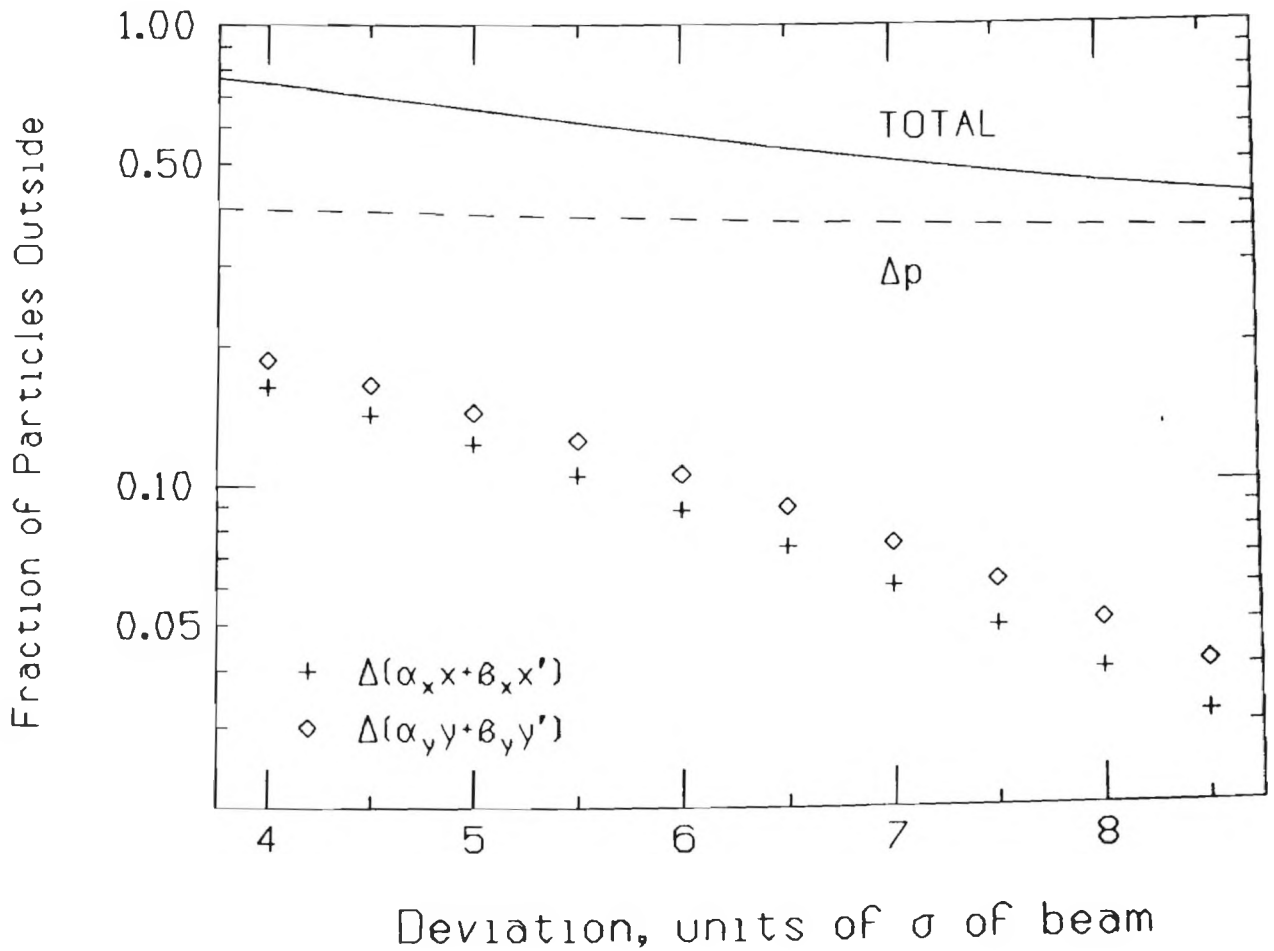
1.00
0.50
0.10
0.05
Fraction of Particles Outside
TOTAL
Δp
+ Δ(αxx+βxx')
◇ Δ(αyy+βyy')
4
5
6
7
8
Deviation, units of σ of beam

Figure 7.3.3